THE UNIVERSITY OF CHICAGO

SYNTHETIC CONTROL OF MERCURY TELLURIDE QUANTUM DOTS AND ITS IMPROVEMENT IN ELECTRICAL AND OPTICAL PROPERTIES

A DISSERTATION SUBMITTED TO

THE FACULTY OF THE PRITZKER SCHOOL OF MOLECULAR ENGINEERING

IN CANDIDACY FOR THE DEGREE OF

DOCTOR OF PHILOSOPHY

BY

HAOZHI ZHANG

CHICAGO, ILLINOIS

JUNE 2023

Table of Content

List of Tables

List of Figures

Acknowledgments

It has been around 5 years since I started working in the PGS lab, and it seems like a short time as I am writing this thesis. I would first like to express my gratitude to my advisor, Prof. Philippe Guyot-Sionnest for all his guidance and support during my Ph.D. years at the University of Chicago. I am truly grateful for the opportunity to work in the PGS lab, which gave me some of the best times I have ever had. Philippe is truly a great researcher, who often helps me with discussions on issues related to my experiments and changed the way I think about these problems during my time working with him. I often get many great ideas by talking to him, which is an enlightening experience.

I would also like to thank all my committee members, Prof. Alexander High and Prof. Dmitri Talapin, who took to the time attend my dissertation defense and help me with many difficulties during my Ph.D.

I am very thankful to all former and current group members in the PGS lab, Dr. Xin Tang, Dr. Matt Ackerman, Dr. Christopher Melnychuk, Dr. Guohua Shen, Ananth Kamath, John Peterson, Dr. Augustin Caillas, and Xingyu Shen. It was a great time working in the lab with them, and often a discussion with them helps me to understand many physics problems a lot more. They are the first people I look for help when I encounter some trouble, but related or unrelated to my research.

Finally, I want to thank my family. Though I am not able to see them for three years because of the pandemic, their support is my best comfort during those difficult times. I would especially like to thank my girlfriend, who I met during the first year of my Ph.D. Time spent with her is the best moment I have ever had, and I am grateful to have her by my side as I am writing this thesis.

Chapter 1: Background and Motivation

1.1 Introduction

Colloidal Quantum Dots (CQDs) are a type of disordered semiconductor nanomaterial with properties that is unique to their kind.[1,2] Their optoelectronic properties can be tuned in many ways, from the semiconductor properties, such as the bulk band gap and doping, to nanoparticle properties, like size, shape, and surface chemistry. This tunability of CQDs makes them desirable when compared to conventional bulk semiconductors. Moreover, improvement in solution synthesis allows us to make ink-like colloidal suspensions, and optoelectronic devices can therefore be fabricated using ink-coating methods. This also makes CQDs similar to a polymer, not just to be more cost-effective, but also enables the creation of devices on soft surfaces that is impossible for conventional materials.[3] In summary, these unique properties make colloidal quantum dots an exciting field to explore and have great potential to advance many technologies in the real world.

My work in the field of colloidal quantum dots focuses on one kind of material only, HgTe. HgTe is described as having a negative band gap, which makes it a semimetal in the bulk form.[4,5] HgTe CQDs can tune their band gap through quantum confinement across the entire infrared spectrum using size control, making them advantageous for infrared imaging. This is particularly important as, traditionally, infrared technology has been expensive despite numerous improvement efforts. This is because commercial infrared photodetectors are based on single crystals of InGaAs, InAsSb, and HgCdTe, which need molecular beam epitaxy (MBE) to grow.[6,7] Also, as they are not compatible with traditional silicon technologies, they need a delicate flip-bonding process to bind them to the silicon readout circuit making this process expensive to be widely adopted.

Mercury chalcogenide quantum dots have been widely considered a potential material for making

next-generation infrared detectors. The PGS lab is a pioneer in researching mercury chalcogenide CQDs and has demonstrated the performance of short-wave infrared (1-2 μm) and mid-wave infrared (3-5 μm) photovoltaic devices approaching commercial devices.[8,9] By manipulating the surface chemistry, such as ligand exchange and core-shell growth, one could expect these devices to outperform their semiconductor counterparts. Together with the ease of synthesis and solution processing, we could make superior infrared devices at less than 1% of the cost.

Making these claims above, it is necessary for these HgTe CQDs to have good optical and electronic properties. Still, before that, the synthesis must be well-controlled, enabling uniform size-controlled quantum dots. This thesis is built on the previous research on both synthesis, optical and electrical properties of HgTe CQDs. I hope that my contribution will enable future researchers in this field to make better dots and devices.

In **Chapter 2**, I will discuss the improvement in the synthesis by controlling the reactivity of the precursors, thus enabling a better shape and size control of quantum dots. I will also discuss the implications of the shape of quantum dots on the intraband spin-orbit splitting though spectroelectrochemistry measurements of these shape-controlled HgTe CQD films.

In **Chapter 3**, I will discuss the improvement of the size control that enables a CQD film to be made with the highest mobility to date. One exciting aspect of this is how it affects the transport of carriers inside this CQD film and gives a more detailed description of a different transport model for these uniform films of quantum dots. Later in this chapter, I will also discuss another limiting factor of device performance, the 1/f noise, and shows how mobility improvement could also facilitate a reduction of 1/f noise.

In **Chapter 4**, I will discuss intraband transition and report on its optical properties. The temperature dependence of this intraband transition is attributed to the presence of a second

conduction band in the 14 band $k \cdot p$ model. Lastly, this intraband transition can be used for infrared light detection of up to 14 μm in the longwave infrared.

In **Chapter 5**, I will discuss some of my thought on some motivating field of research and potential future directions, with comments on their practicality.

1.2 Theory of CQD systems

Quantum dots are semiconductors in which the electrons and holes are confined to length scales on the nanometer range, which leads to the bands splitting into discrete energy levels, with defined angular momentum for spherical boundaries This gives two unique properties which do not exist in the bulk. First, the band gap of CQDs does not just depends on the bulk band gap of the material, but on the length of the confinement, such that they can be tuned by the size of the nanoparticle. Second, instead of a continuous band, the energy levels of the CQDs are discrete, which makes intraband transitions within each band available. This intraband property is discussed as part of my thesis.

The physics of quantum dots are simple, particle in a box system. i.e., when an infinite potential well of length gap L confines the electrons and holes in 1 dimension, the energy levels of the confinement take on discrete values given as $E_n = \frac{n^2h^2}{8m^*L^2}$. In reality, with dots close to spherical, the quantization is described by particle in a sphere model with the principal n and orbital quantum number l, and the solutions being the spherical Bessel functions. Thus, the states are described as nl, similar to atomic orbitals.

Another approach to thinking about colloidal quantum dots starts with the bulk material. For a bulk semiconductor with band structure shown in Fig. 1-1, the energy of the carriers can be described by their wavevector, k.[10] In parabolic approximation, $E = \frac{\hbar^2k^2}{2m^*}$, where m^* being the

effective mass of the carriers in this band. By reducing the dimension of the bulk semiconductor to a sphere, k will take discrete values depending on the radius r. The quantum number nl defines the energy levels of k, which is shown in Fig. 1-1.

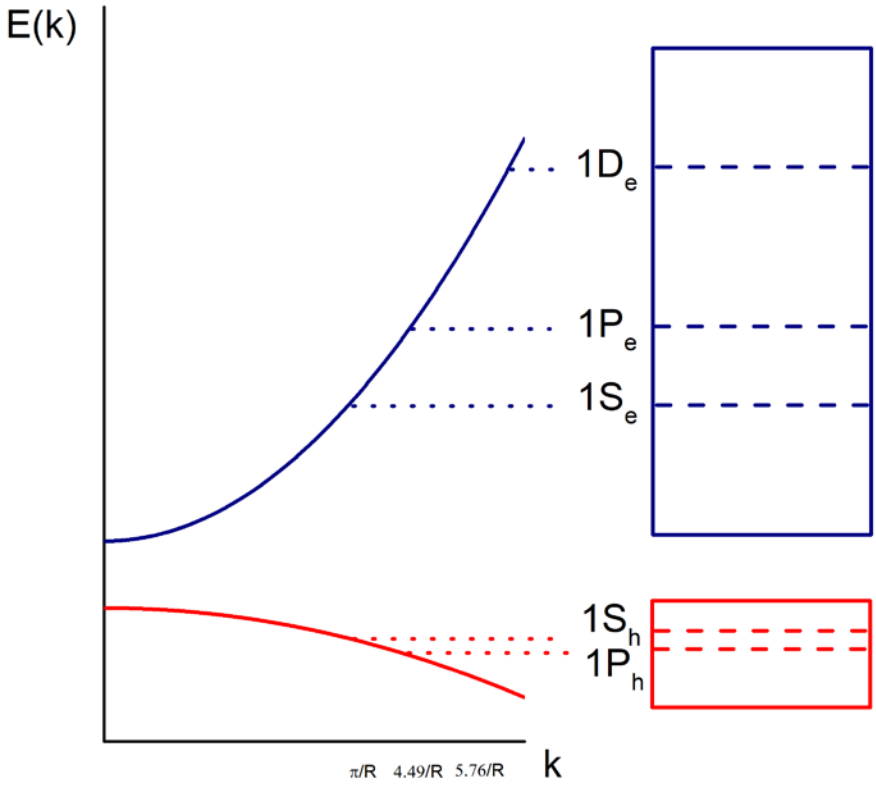

Fig. 1-1. Correspondence of the bulk semiconductor bands and the quantized quantum dot energy levels. The quantum dot states are labeled by the quantum number nl which also defines the wavevector k.

Free carriers in quantum dots are created by changing the Fermi level through chemical or electrical controls called doping, or by creating an exciton through thermal activation or optical absorption. For the CQDs to form an electrical device, the carriers in one dot need to move to other dots to be eventually measured as a current. Since the potential energy confines the dots at the surface, this is possible only by carrier tunneling through the barrier into neighboring dots.[11] One

important study of the CQDs in this thesis is the carrier transport through the film. Carrier transport not only reveals the fundamental physics of how electrons move in disordered systems like a film of quantum dots. It is also important for device applications as the time of carrier extraction need to be faster than the excitation lifetime for optimal device performances.

1.3 The metal-insulator transition

The question of whether a material is metallic or insulating at absolute zero temperature has been studied for decades.[12] To understand this, a simple model for the metallic insulator transition was first described by Mott for a crystalline array of hydrogen-like atoms with one electron per site.[13,14] Mott predicted that a critical density of free electrons and holes is necessary for the system to be metallic, and a continuous increase in the number of free carriers from zero is not possible before this critical concentration. If the electron density in the system is below this critical density, the material is an insulator. In that case, its transport will be described as 'hopping', where the electrons are in localized states bound to each atomic site except for a limited probability of tunneling to nearby sites. If the temperature is lowered further, the hopping is favored to more distant sites and follows a variable range hopping model.

For metallic electrical transport to happen, once an electron leaves its atom and becomes free, it leaves a positive hole which attracts the departing electron with a force of $e^2/\varepsilon r^2$, where ε is the dielectric constant. Therefore, at absolute zero, metallic conductivity is impossible unless there is sufficient screening of this force for the electrons to be free. With screening into consideration, we can derive the Coulomb potential energy of an electron,

$$-\frac{e^2}{4\pi\varepsilon\varepsilon_0 r}\exp(-qr)$$

q is the screening constant of the electron, given by the Thomas-Fermi approximation.

$$q = \sqrt{4m^* e^2 n^{1/3}/4\pi\varepsilon\varepsilon_0 \hbar^2} = \sqrt{4n^{1/3}/\alpha_H}\ .$$

$\alpha_H = \hbar^2 4\pi\varepsilon\varepsilon_0/m^* e^2$ is the effective Bohr radius of the electron, and m^* the reduced mass. Thus, q is related to the electron density, where a high number of electrons provides the screening needed for an electron to be free. The Metal-Insulator Transition (MIT) is proposed to occur when the screening takes place when $q = \frac{1}{\alpha_H}$, giving the Mott critical concentration n as $n^{1/3}\alpha_H = 1/4$. On a log scale, this criterion has been verified for a wide range of disordered materials, where the doped semiconductor reaches metallicity at the critical carrier density, as shown in Fig. 1-2.

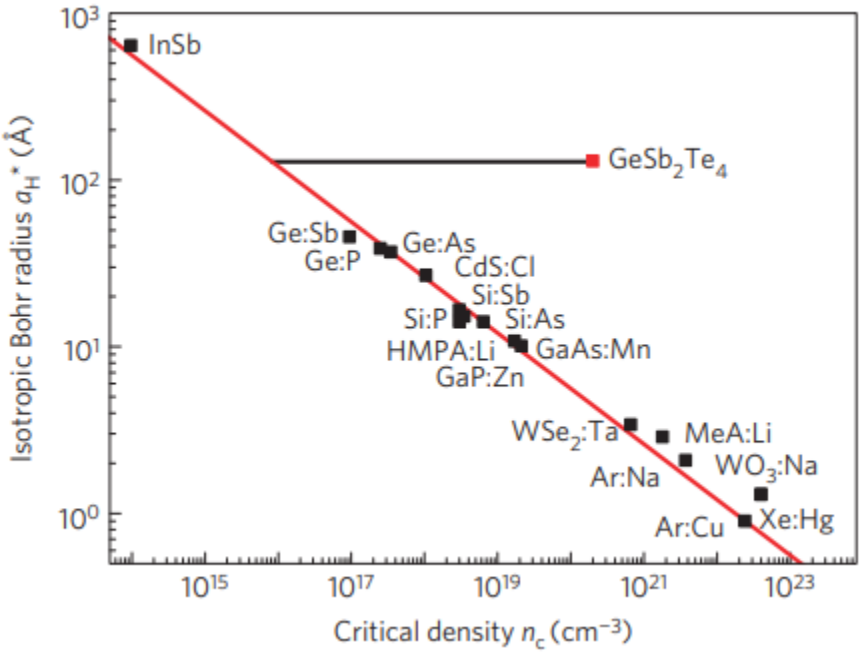

Fig. 1-2. The Mott criterion ($n_c^{1/3}\alpha_H = 0.26$) is shown as the red line, where the critical density of individual material is shown as black dots. The metallic regime is shown as the right of the line. Not all materials follow the Mott criterion, as the Mott criterion cannot predict the MIT of GeSb2Te4. The figure is adapted from Ref. 12

Although the Mott criterion is valid for a range of materials, a more comprehensive model that predicts the MIT needs to consider the correlation effects and disorder. Three energies are required to take into consideration for the electrons in the system, the Fermi Energy, the Coulomb Energy, and the Energy of Mobility Edge for the Anderson transition.[12,15]

The first criterion (Mott) requires the energy at the Fermi level to overcome the Coulomb Energy due to electron-electron repulsion at zero Kelvin.[13]

$$E_F = \frac{\hbar^2(3\pi^2 n)^{2/3}}{2m^*} > E_C = \frac{e^2}{4\pi\varepsilon_0\varepsilon} n^{1/3}$$

Not surprisingly, since it is still a balance between the delocalizing quantum kinetic energy and the localizing Coulomb interaction, this gives a result very similar to the previous discussion. Rearranging the formula gives a similar prediction to the Mott's critical concentration as $n^{1/3}\alpha_H > \frac{2}{(3\pi^2)^{2/3}} \sim 0.2$.

When introducing correlation, there is a distinct possibility of having an insulator at integer filling of the states of each site even for a perfectly ordered system. This happens when the on-site repulsive interaction, due to two electrons occupying a single site, is larger than the coupling energy which projects the electron over its neighbors. This is called the Mott insulator. A minimal model of the Mott insulator is the Hubbard model with only two ingredients, a kinetic energy term, *t,* allowing for tunneling of electrons between lattice sites and a potential term, *U*, reflecting on-site interaction. For a low enough value of t/*U*, this model predicts the Mott insulator at n=1 when every site is occupied by one electron, and it predicts metallic behavior for other fillings, and for sufficient ratios of t/U. The system can be metallic when it is close to n=0 or n=2 with small values of t/U.

However, if there is disorder, the system will always be an insulator for low state-filling and close

to complete state-filling. This is due to disorder-induced localization (Anderson). Anderson localization exists if the randomness of the energy levels is large enough to separate delocalized states and localized states.[15] The boundary is called the mobility edge. If the Fermi energy is lower than the boundary, all the states are localized and the system is an insulator, while if the Fermi energy is higher than the boundary, some states are delocalized, and the system is metallic. Therefore, the metal-to-insulator transition occurs when the energy that separates the localized states from the delocalized states is larger than the Fermi Energy of the electrons. This is best visualized in Fig. 1-3.

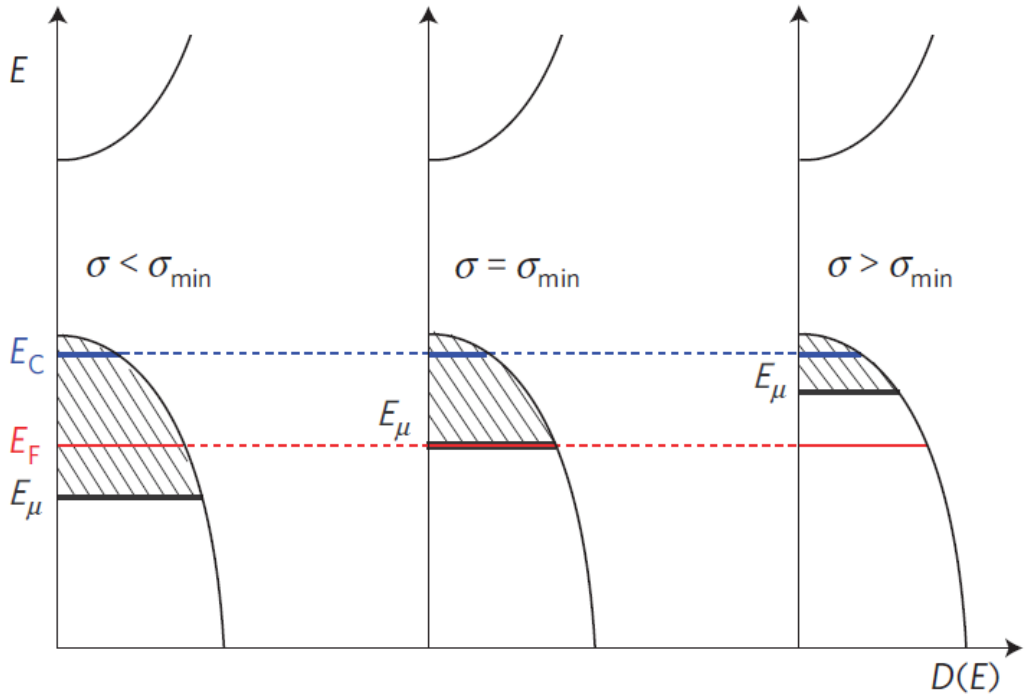

Fig. 1-3. The shaded region denotes the localized states due to disorder in the system.

As long as the Fermi energy E_F lies within the localized states (shaded regions) the system is insulating (left). When the mobility edge passes the Fermi energy (center) the 'Anderson-like' transition to metallic behavior (right) occurs. Note that Coulomb energy is always less than the Fermi energy, however the material can still be insulating due to disorder. The figure is adapted from Ref. 12.

While the discussion above provides a qualitative, or semi-quantitative, description of the metal-insulator transition in disordered semiconductors, taking into account colloidal nanoparticles adds a layer of complexity since colloidal quantum dots are different from bulk-disordered materials in at least three aspects.[16]

1. CQD solids often do not form good lattices and have no symmetry, such that a wavevector cannot be well defined over a wide range of dots.

2. The disorder comes from the distribution of sizes of the CQDs, which is different from impurities as they also affect the spatial overlap of wavefunctions.
3. The size and shape of the CQDs also affect the coupling between quantum dots, i.e., the conductance channel is restricted to pass through the surface of the dots instead of a bulk matrix.

A model discussing transport in quantum dots can start from two nanoparticle spheres, as shown in Fig. 1-4. This is in the same spirit as the above discussion of nearest neighbor Mott criterium, and the Mott-Ioffe-Regel limit which considers that the mean free path equal to the interparticle distance is the limiting case of a metallic conductor.

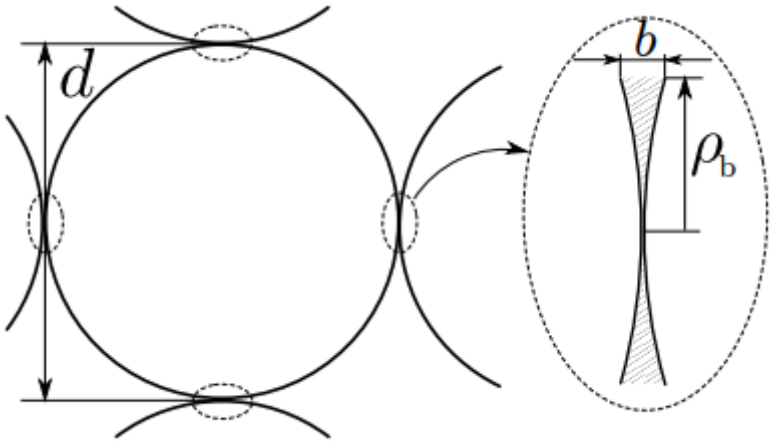

Fig. 1-4: Two NCs touching away from prominent facets are shown. In this case, electrons tunnel through the contact which is depicted in the inset. The radius of the contact is ρ_b, where b is the decay length of an electron in the medium surrounding NCs. Figure adapted from Ref. 16.

For a dot with a barrier height W at the surface, the tunneling distance is defined as $b = \hbar/\sqrt{2m^*W}$. For most CQDs, b will be of the order of a few angstroms. The effective area of the conductance channel between two dots is given by $\pi\rho^2$, where ρ is taken to be such that the gap between the dot surfaces is below the tunneling distance b. ρ is estimated by $\rho = \sqrt{db/2}$, where d is the diameter of the dot. (Fig. 1-4)

The conductance of two metallic spheres with electrons of momentum $\hbar k_F$ in the ballistic regime is then taken as[17]

$$G = \frac{e^2}{\pi\hbar}\frac{k_F^2}{4\pi}\pi\rho^2 e^{-l/b}$$

where l is the distance separating the dots. This can be understood by the number of channels being the product of the Fermi surface and the effective area, and with each channel contributing a unit of quantum conductance, $e^2/\pi\hbar$, reduced by the tunneling probability $e^{-l/b}$.

The proposed metal-insulator transition occurs when the average conductance G between two dots is equal to the quantum conductance.[11,18,19] The energy barrier for transport is $E = e^2/C$, where C is the capacitance of the two dots. The RC constant of the dots needs to be smaller than the coherence time τ of the electron for nearest neighbor coherence to be established. Thus, as $E = e^2/C = h/\tau \sim h/RC$. This implies that conductance $G = \frac{1}{R} \sim e^2/h$ is required for electron to maintain its coherence during the time of transport. Thus, the metal insulator transition is assigned to arise when the nearest neighbor conductance exceeds the quantum conductance. By substituting $G = e^2/\pi\hbar$, we can solve the equation for k_F which gives.

$$k_F\rho e^{-l/2b} = 2$$

Using the k_F from the electron gas model $k_F = (3\pi^2 n)^{1/3}$, we get the following,

$$n_c = \frac{8}{3\pi^2\rho^3}e^{3l/2b}$$

Typically, $\rho = 0.25\ d$ where d is the diameter of a dot.[20]

Taking $l \sim 5b = 0.5$ nm and a dot with diameter of 15 nm, we get the critical carrier density $n_c \sim 10^4\ e^-$/dot, which can lead to arguments that MIT will only be possible for metallic nanoparticles. Yet, the previous discussion of Mott and Anderson localization does not a priori justify this restriction. The difference is that, in contrast to the prior discussion of the Mott model, the Fermi wavevector defined here is *within* the metallic particle and does not arise from the coupling between the particles. This model is therefore applicable to very highly doped semiconductor quantum dots, but it does not clearly relevant for the quantum dots with low carrier number.

Interestingly, some of the best quantum dots right now reach mobility of up to 10 cm^2/Vs.[21–23] G is related to the mobility by $\mu = G/end$, so that $\frac{G}{(e^2/\pi\hbar)} = \frac{\mu n d}{e}\pi\hbar$. With one electron per dot, n~ $1/d^3$, $\frac{G}{(e^2/\pi\hbar)} \sim \frac{\mu}{\mu_q}$ where $\mu_q = \frac{h}{2ed^2}$ and therefore μ_q is a "quantum" mobility which is the minimum value needed to achieve metallic behavior. This value is 1100 cm^2/Vs for 15 nm particles, which is much higher than 10cm^2/Vs, but also much smaller than the mobilities reported for crystalline HgCdTe.

Due to variation in quantum dots, we also need to consider the energy variation of the states ΔE and the reorganization energy of the dot matrix λ. This is a second criterion for quantum dot conductance, with the Fermi energy of the electrons needing to be larger than both ΔE and λ. ΔE can be improved through better synthetic control and size selective precipitation, and λ may become the more limiting factor. [24]

With HgTe dots of 15 nm diameter, a previous experiment indicated a nearest neighbor coupling energy of 1.6 meV with one electron filling in the $1S_e$ state. This implies a full band width of 12 × 1.6 meV = 19.3meV. The reorganization energy λ is estimated to be 4.2 meV. There is therefore

a range of filling that is possible for $E_F > \lambda$. Furthermore, the Fermi energy scales in proportion to the coupling, which was observed to be rather independent of size, while the reorganization energy λ scales as $1/r^2$. Thus, much that can be gained by making larger dots. In addition, λ can be improved by better packing which reduces the dielectric constant.

In summary, a perfect lattice, with partial electron filling and only electron-electron repulsion, can exhibit metallic behavior (Mott metal-insulator model). A perfect lattice with polaronic interactions, such as the reorganization energy, needs inter-site tunneling larger than the polaronic well energy to present metallic behavior. A disordered lattice always has localized states, but it may also have delocalized states if the Fermi energy is raised above the mobility edge, and this requires a coupling stronger than the disorder. With the coupling energy previously achieved with HgTe quantum dots, the measured mobility was still ~100 times below the minimum needed for delocalization across neighboring dots. It may then be plausible that reduction of the static and dynamic disorder, and the localization energy, will significantly increase the mobility and possibly lead to delocalization and metallic transport at zero kelvin.

REFERENCES:

(1) Efros, A. L.; Brus, L. E. Nanocrystal Quantum Dots: From Discovery to Modern (1) Efros, A. L.; Brus, L. E. Nanocrystal Quantum Dots: From Discovery to Modern Development. *ACS Nano* **2021**, *15* (4), 6192–6210. https://doi.org/10.1021/acsnano.1c01399.

(2) García de Arquer, F. P.; Talapin, D. V.; Klimov, V. I.; Arakawa, Y.; Bayer, M.; Sargent, E. H. Semiconductor Quantum Dots: Technological Progress and Future Challenges. *Science* **2021**, *373* (6555), eaaz8541. https://doi.org/10.1126/science.aaz8541.

(3) Kagan, C. R.; Lifshitz, E.; Sargent, E. H.; Talapin, D. V. Building Devices from Colloidal Quantum Dots. *Science* **2016**, *353* (6302), aac5523. https://doi.org/10.1126/science.aac5523.

(4) Svane, A.; Christensen, N. E.; Cardona, M.; Chantis, A. N.; van Schilfgaarde, M.; Kotani, T. Quasiparticle Band Structures of $\ensuremath{\beta}$-HgS, HgSe, and HgTe. *Phys. Rev. B* **2011**, *84* (20), 205205. https://doi.org/10.1103/PhysRevB.84.205205.

(5) Allan, G.; Delerue, C. Tight-Binding Calculations of the Optical Properties of HgTe Nanocrystals. *Phys. Rev. B* **2012**, *86* (16), 165437. https://doi.org/10.1103/PhysRevB.86.165437.

(6) Rogalski, A. HgCdTe Infrared Detector Material: History, Status and Outlook. *Rep. Prog. Phys.* **2005**, *68* (10), 2267. https://doi.org/10.1088/0034-4885/68/10/R01.

(7) Rogalski, A. *Infrared and Terahertz Detectors, Third Edition*; CRC Press, 2019.

(8) Ackerman, M. M.; Tang, X.; Guyot-Sionnest, P. Fast and Sensitive Colloidal Quantum Dot Mid-Wave Infrared Photodetectors. *ACS Nano* **2018**, *12* (7), 7264–7271. https://doi.org/10.1021/acsnano.8b03425.

(9) Tang, X.; Chen, M.; Kamath, A.; Ackerman, M. M.; Guyot-Sionnest, P. Colloidal Quantum-Dots/Graphene/Silicon Dual-Channel Detection of Visible Light and Short-Wave Infrared. *ACS Photonics* **2020**, *7* (5), 1117–1121. https://doi.org/10.1021/acsphotonics.0c00247.

(10) Kittel, C.; McEuen, P. *Introduction to Solid State Physics*; John Wiley & Sons, 2018.

(11) Guyot-Sionnest, P. Electrical Transport in Colloidal Quantum Dot Films. *J. Phys. Chem. Lett.* **2012**, *3* (9), 1169–1175. https://doi.org/10.1021/jz300048y.

(12) Siegrist, T.; Jost, P.; Volker, H.; Woda, M.; Merkelbach, P.; Schlockermann, C.; Wuttig, M. Disorder-Induced Localization in Crystalline Phase-Change Materials. *Nat. Mater.* **2011**, *10* (3), 202–208. https://doi.org/10.1038/nmat2934.

(13) Mott, N. F. The Transition to the Metallic State. *Philos. Mag. J. Theor. Exp. Appl. Phys.* **1961**, *6* (62), 287–309. https://doi.org/10.1080/14786436108243318.

(14) Hussey ǁ, N. E.; Takenaka, K.; Takagi, H. Universality of the Mott–Ioffe–Regel Limit in Metals. *Philos. Mag.* **2004**, *84* (27), 2847–2864. https://doi.org/10.1080/14786430410001716944.

(15) Anderson, P. W. Absence of Diffusion in Certain Random Lattices. *Phys. Rev.* **1958**, *109* (5), 1492–1505. https://doi.org/10.1103/PhysRev.109.1492.

(16) Chen, T.; Reich, K. V.; Kramer, N. J.; Fu, H.; Kortshagen, U. R.; Shklovskii, B. I. Metal–Insulator Transition in Films of Doped Semiconductor Nanocrystals. *Nat. Mater.* **2016**, *15* (3), 299–303. https://doi.org/10.1038/nmat4486.

(17) Nikolić, B.; Allen, P. B. Electron Transport through a Circular Constriction. *Phys. Rev. B* **1999**, *60* (6), 3963–3969. https://doi.org/10.1103/PhysRevB.60.3963.

(18) Matveev, K. A. Coulomb Blockade at Almost Perfect Transmission. *Phys. Rev. B* **1995**, *51* (3), 1743–1751. https://doi.org/10.1103/PhysRevB.51.1743.

(19) Beloborodov, I. S.; Lopatin, A. V.; Vinokur, V. M.; Efetov, K. B. Granular Electronic Systems. *Rev. Mod. Phys.* **2007**, *79* (2), 469–518. https://doi.org/10.1103/RevModPhys.79.469.

(20) Liljeroth, P.; Overgaag, K.; Urbieta, A.; Grandidier, B.; Hickey, S. G.; Vanmaekelbergh, D. Variable Orbital Coupling in a Two-Dimensional Quantum-Dot Solid Probed on a Local Scale. *Phys. Rev. Lett.* **2006**, *97* (9), 096803. https://doi.org/10.1103/PhysRevLett.97.096803.

(21) Lee, J.-S.; Kovalenko, M. V.; Huang, J.; Chung, D. S.; Talapin, D. V. Band-like Transport, High Electron Mobility and High Photoconductivity in All-Inorganic Nanocrystal Arrays. *Nat. Nanotechnol.* **2011**, *6* (6), 348–352. https://doi.org/10.1038/nnano.2011.46.

(22) Balazs, D. M.; Matysiak, B. M.; Momand, J.; Shulga, A. G.; Ibáñez, M.; Kovalenko, M. V.; Kooi, B. J.; Loi, M. A. Electron Mobility of 24 Cm2 V−1 S−1 in PbSe Colloidal-Quantum-Dot Superlattices. *Adv. Mater.* **2018**, *30* (38), 1802265. https://doi.org/10.1002/adma.201802265.

(23) Chen, M.; Lan, X.; Tang, X.; Wang, Y.; Hudson, M. H.; Talapin, D. V.; Guyot-Sionnest, P. High Carrier Mobility in HgTe Quantum Dot Solids Improves Mid-IR Photodetectors. *ACS Photonics* **2019**, *6* (9), 2358–2365. https://doi.org/10.1021/acsphotonics.9b01050.

(24) Lan, X.; Chen, M.; Hudson, M. H.; Kamysbayev, V.; Wang, Y.; Guyot-Sionnest, P.; Talapin, D. V. Quantum Dot Solids Showing State-Resolved Band-like Transport. *Nat. Mater.* **2020**, *19* (3), 323–329. https://doi.org/10.1038/s41563-019-0582-2.

Chapter 2: Shape Controlled HgTe Colloidal Quantum Dots and Reduced Spin-Orbit Splitting in the Tetrahedral Shape

In this chapter, I will explain the improvement in synthetic control than enables a lot of the studies in this thesis. Following on the non-aggregated synthesis developed by Shen et al. in 2017, I have demonstrated that shape and size distribution of HgTe CQDs can be controlled using the reactivity of the precursors, where using highly reactive species such as TMSTe and a higher temperature preferably forms dots that are spherical in shape, whereas less reactive species and lower temperatures forms more faceted CQDs.

The rest of this chapter will discuss the implication of the shape and sizes through spectro-electrochemistry studies, whereby gating the film using an electrolyte enables one to measure the spectrum at different doping levels. This study shows that the tetrahedral-shaped CQDs have a reduced spin-orbit splitting when compared to more spherical dots, thus causing a narrowing in the intraband transition. Such narrowing in transition could be beneficial in both intraband photodetection and LEDs, as it leads to a narrower spectrum and potentially higher mobility.

Most of this chapter is adapted from ref. 29, with some unpublished data.

2.1 Introduction

Colloidal quantum dots (CQDs) have been an active field of research as they afford tunable optoelectronic properties[1,2], by changing size[3], shape[4–6] and surface ligands[7]. Many investigations have focused on CQDs with visible and near-infrared energy gap, motivated by visible fluorescence, photodetection and solar cell applications.[1,2] The development of the CQD synthesis of smaller gap materials, such as the HgTe CQDs[8,9] , has enabled devices extending to mid-IR with promising performance, including reaching background limited noise for photovoltaic detectors.[10] HgTe CQDs were initially synthesized in polar solvent[11,12], but the synthesis in organic solvent, as developed by Keuleyan et. al.,[8] has been the most extensively used in device developments. In this synthesis, $HgCl_2$ in oleylamine is reacted with trioctylphosphine telluride (TOPTe). Typically, the TEM spectroscopy shows that CQDs are strongly faceted or tetrahedral but significantly aggregated. The absorption spectra nevertheless show a strong first absorption peak than can still be observed for mid-infrared CQDs. Although devices made with such aggregated dots have good performances, further improving device performance requires methods such as ligand exchange to increase mobility, surface modifications to control doping, and shell growth to reduce nonradiative losses. However, such surface manipulations are hindered with aggregated dots because the CQD surfaces are in large part not accessible. In order to address this problem, Shen et al. [9] developed an alternative synthesis that yields non-aggregated HgTe. This modified method starts with a more than 2-fold excess of $HgCl_2$ in oleylamine, uses the more reactive bis(trimethylsilyl)telluride (TMSTe), and is done in the absence of TOP. The reaction results in dispersed HgTe CQDs with rather spherical, or cubooctahedral shapes, that enabled studies of surface modification for increasing the electrical mobility in thin films.[13] These CQDs are rather well monodispersed, with ~10% size distribution, but show a broad yet strongly

structured intraband absorption. The study of these spectra highlighted a very significant spin-orbit splitting of the second electronic state of P symmetry.[14] The interband spectra also show that the absorption edge is much softer than for the aggregated faceted HgTe CQDs. Although this broadening was not understood, it directly affects the photodetection spectra and it is bound to increase noise for a given cut-off wavelength detector.

In this work, we improved the size control of the spherical CQDs and we explored shape control to attempt to sharpen the absorption edge. Since the dispersed spherical CQDs are synthesized with excess mercury and a reactive tellurium source, we started with the synthesis of such spherical small and dispersed HgTe CQDs and then investigated the effect of additional growth steps. Reasoning empirically that the strong faceting seen with the aggregated CQDs takes place when using TOPTe as a reagent, we studied the subsequent additions of either TMSTe or TOPTe. Spectroelectrochemistry and Transmission electron microscopy (TEM) are used to assess size, shape and interband and intraband spectra.

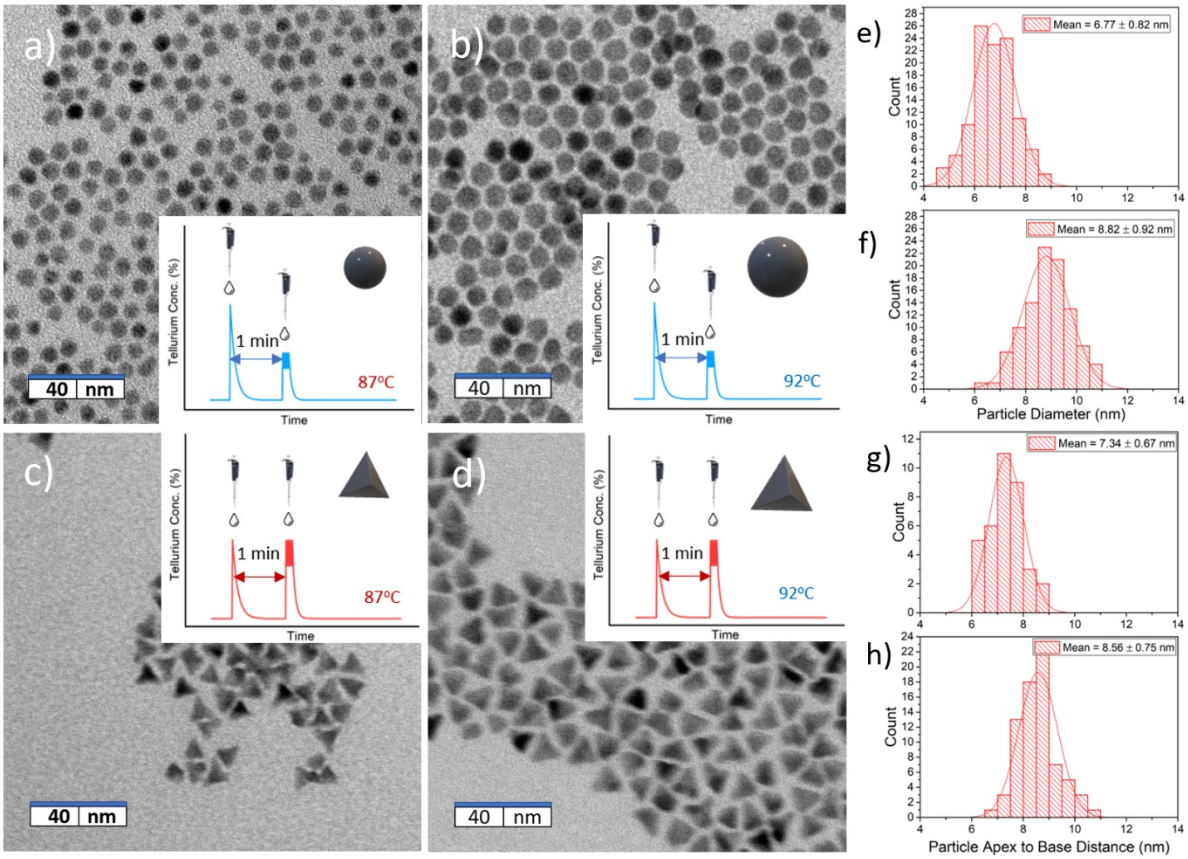

Fig. 2-1. a). Spherical Dots synthesized using the 0.05 mmol: 0.05 mmol TMSTe:TMSTe protocol at 86°C. b.) Same as a) but the reaction temperature is 92°C. c). Tetrahedral Dots synthesized using the 0.025 mmol: 0.075 mmol TMSTe:TOPTe protocol at 86°C. d.) Same as c) but the reaction temperature is 92°C. Inset: synthetic protocol for both tetrahedron and spherical dots at the two sizes respectively. e-h). The size distribution histogram for the particles shown in a-d). respectively.

2.2 Narrower size distribution of HgTe spherical CQDs.

In this work we describe HgTe CQDs such as those shown in (Fig. 2-1.a, b.) as "spherical", even though it is noted that the shape deviates from a sphere due to crystal truncation. Such spherical HgTe CQDs are obtained with a minor modification of the Shen synthesis.[9] A typical single step synthetic procedure involves dissolving $HgCl_2$ (0.2 mmol) in purified oleylamine (OAm) at 100^{o}C while stirring on a hotplate under inert atmosphere, then, TMSTe (0.1 mmol), first diluted in oleylamine, is quickly injected into the Hg precursor. The ratio of Hg:Te = 2:1 is crucial for the dots being non-aggregated. We then explored adding multiple injection steps to achieve some degree of shape control while also providing better size uniformity, similar to other reports on PbS CQDs.[15] For example, splitting the single injection in two steps with a first rapid injection of TMSTe (0.05 mmol) and a second slow injection of TMSTe of also 0.05 mmol, maintaining the final 2:1 ratio of Hg to Te, leads to spherical dots with better size distribution. Fig. 2-1.a,b shows TEM images for two reactions at 86^{o}C and 92^{o}C along with the size distribution. (Fig. 2-1 e,f) However, while the multiple injection has worked very well for PbS[15], we found that further splitting the injections did not improve the size distribution further for the HgTe CQDs but instead resulted in more facetted CQDs.

2.3 Tetrahedral and dispersed HgTe CQDs.

The CQDs shown in Fig. 2-1.c,d are described as "tetrahedral" while it is noted that they are not perfectly tetrahedral and may have differing degrees of truncation of the branches. This shape is obtained by splitting the addition of the total tellurium (0.1mmol) into multiple steps. A first injection consists of 0.025 mmol of TMSTe diluted in oleylamine to initiate the formation of smaller spherical CQDs. After 1 min of reaction, 0.075 mmol of TOPTe is diluted in oleyamine and injected dropwise, keeping the final 2:1 ratio of tellurium to Hg. This leads to the dispersed

dots with a tetrahedral shape. Fig. 2-1.c,d follow the same protocol except that the reaction temperatures are 86°C and 92 °C respectively.

Fig. 2-1 shows that, starting from spherical CQDs, the two growth protocols result in distinct shapes of the HgTe CQDs. The higher the amount of TOPTe added during the growth, the more tetrahedral the shape, whereas less added TOPTe leads to more spherical dots, which demonstrates the importance of TOPTe in controlling the faceting of the dots.[16–18] We propose that the shape change arises from the general propensity for faceting when growth is slow. We believe this kinetics difference is partly due to the coordination of the TOP ligand to the surface of the dots during synthesis, slowing down the HgTe growth.[19] The kinetic argument is supported by further experiments which also lead to facetted CQDs without using TOPTe. For example, four injections of lower concentration TMSTe (0.025mmol each) lead to more facetted particles, although not as nicely tetrahedral as when using TOPTe, as shown in Fig. 2-3.

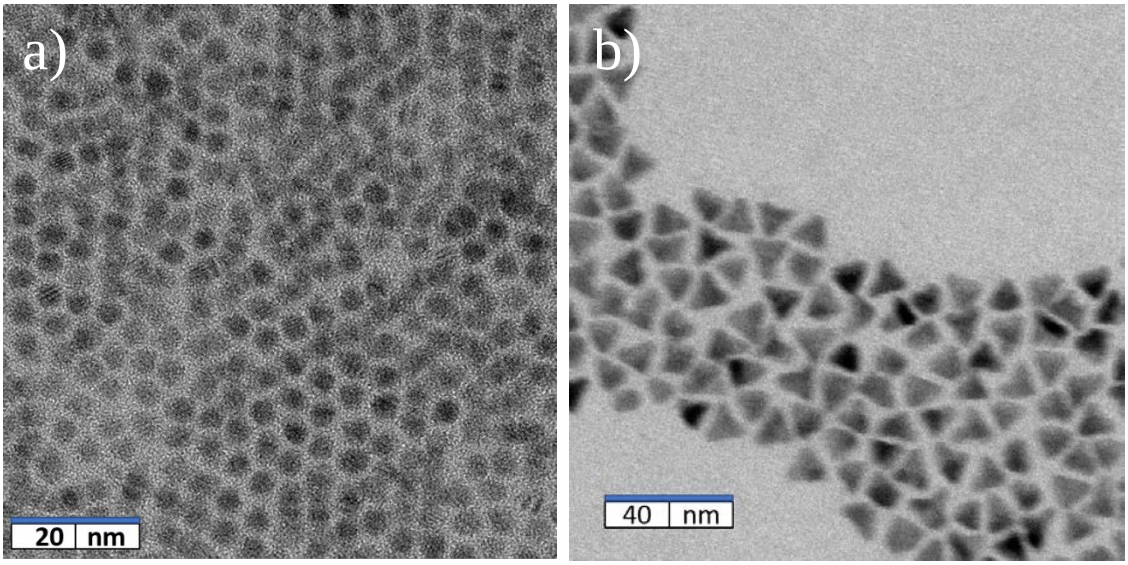

Fig. 2-2. a). Nuclei of the tetrahedral quantum dots synthesis with 0.025 mmol TMSTe after 1 min at 92°C b.) Tetrahedral Dots synthesized using the 0.025 mmol: 0.075 mmol TMSTe:TOPTe protocol at 86°C.

Shape control is well known for other CQDs such as CdSe where quasi-spherical[6], tetrahedral[20], nanorods[4,21,22] and platelets[23] can be synthesized and this is typically attributed to a combination of ligands and kinetic effects. HgTe is only forming in the zinc blend structure, but it is likely that HgTe will be amenable to further shape control in the future.

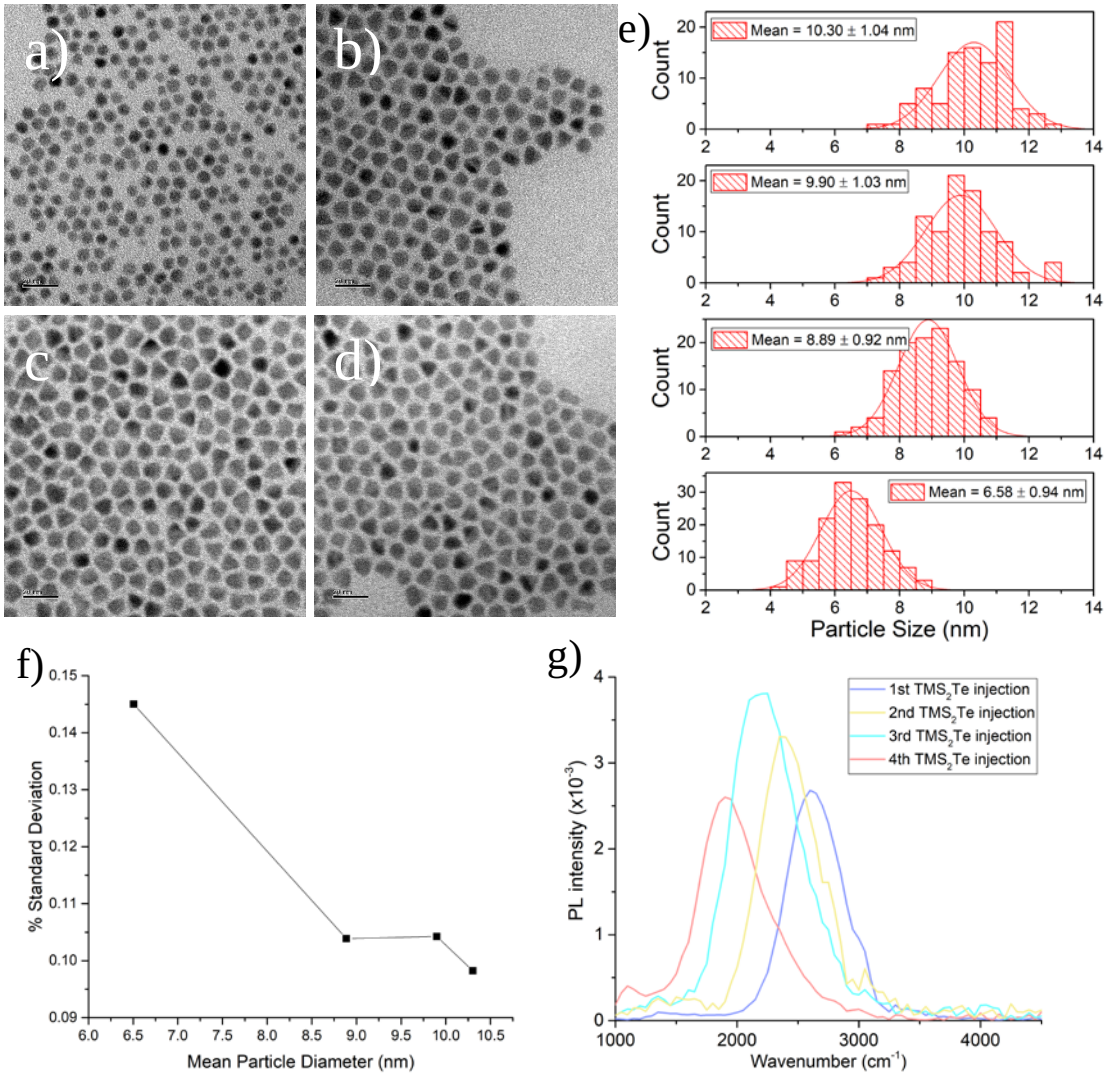

Fig. 2-3. a). TEM of HgTe QD of 1st injection of 0.025 mmol TMSTe after 40 sec at 90°C. b). 2nd injection of 0.025 mmol TMSTe into a). with the same reaction condition. c). 3rd injection. d). 4th injection of TMSTe. e). Size distribution of the HgTe QDs for a-d). f). % Standard Deviation of the dots with respect to size. g). Photoluminescence spectra of the HgTe QD synthesized in a-d).

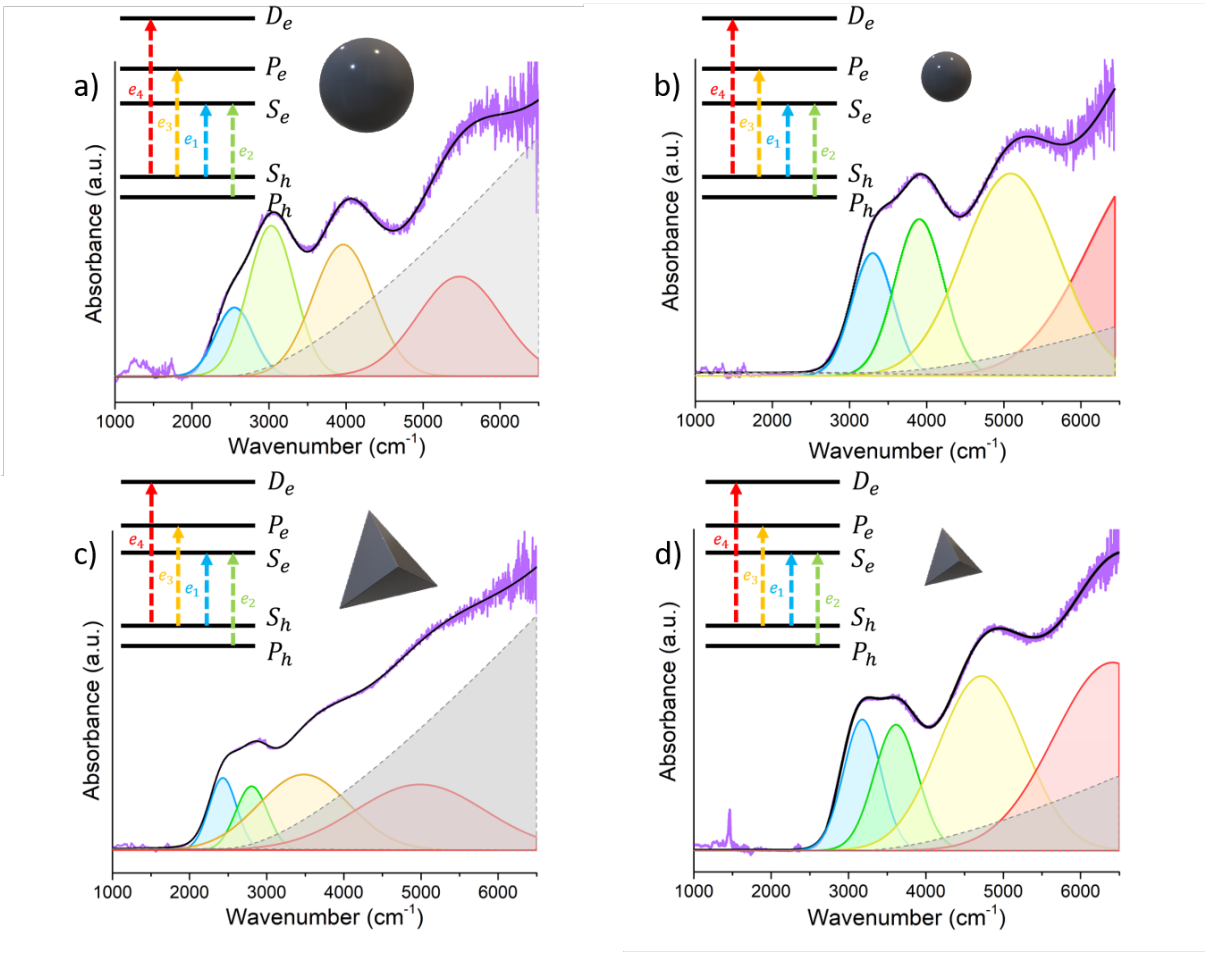

Figure. 2-4. a-b). Absorption spectra of spherical HgTe QDs with absorption edges at 2527 cm^{-1} and 3220 cm^{-1}. The spectra are fitted to a sum of four Gaussians (e1, e2, e3, e4) and a background function. c-d). Absorption spectra of faceted HgTe QDs with absorption edges at 2434 cm^{-1} and 3179 cm^{-1} and similar fits. In all figures, the data is shown with the violet line and the fitted data is shown in black.

A particularly interesting and potentially useful finding in this work is that the shape, spherical or tetrahedral, strikingly affects the absorption spectra. As far as we know, spherical and tetrahedral CQD are not known to exhibit very different absorption spectra. Indeed, CdTe or CdSe CQDs can be synthesized as tetrahedral zinc-blend or as quasi-spherical wurtzite but the absorption spectra vary only in subtle manners.[20,24] Fig. 2-4 shows the absorption spectra of two pairs of the HgTe CQDs with similar absorption edge energy. An obvious difference is a much stronger first exciton for the tetrahedral CQDs and a sharper absorption edge than for the spherical CQDs.

The absorption spectra are further analyzed by fitting a sum of gaussians and a background function describing the higher energy absorption. We tentatively assign the first transition as $1S_h$-$1S_e$. Comparing the spherical and tetrahedral CQDs with the same $1S_h$-$1S_e$ energies, and assuming the shape of the faceted QDs to be regular tetrahedron, their calculated volume is slightly smaller than for the spherical ones, as shown in Table 2-1. At first glance, this might appear in contradiction with the typical notion that smaller dots should have a larger confinement energy. We also observe that the next transitions are closer for the tetrahedral shape. Assigning the second transition to $1P_h$-$1S_e$ and the third transition to $1S_h$-$1P_e$ as justified further below, the tetrahedral CQDs show a noticeably lower energy for the third transition. This is tentatively attributed to a lesser confinement of the P_e orbitals, with the explanation that they can extend further in the tetrahedral shape.

Regarding the improved sharpness of the absorption edge in tetrahedral CQDs, this arises from the relative strengths of the 1st and 2nd transition as shown in Table 2-1. For the spherical CQDs, the 1st transition is weaker than the 2nd transition (about 40%-70%). In contrast, for the tetrahedral CQDs, the 1st transition is stronger that the 2nd transition (about 110-120%).

The fitted Gaussian for the 1st transition of the faceted dots is also slightly narrower compared to the spherical counter parts by ~ 10%. PL spectra of the tetrahedral dots show a correspondingly narrower FWHM as shown in Fig. 2-5.

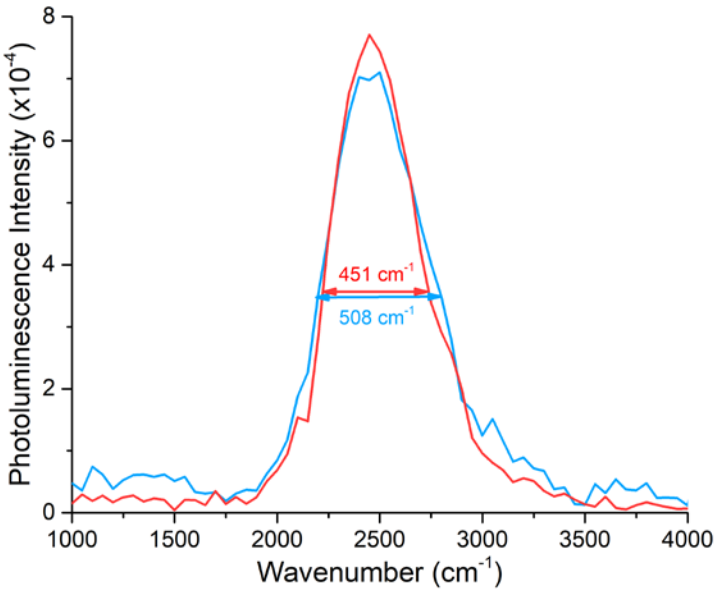

Fig. 2-5. Photoluminescene spectrum of spherical (blue) and tetrahedral (red) HgTe CQDs. The FWHM is measured by fitting a gaussian function and extracted from the fitting.

Table 1	Spherical QD edge (2527)	Faceted QD edge (2434)	Spherical QD edge (3220)	Faceted QD edge (3179)
e_1 peak position	2527 cm^{-1}	2434 cm^{-1}	3220 cm^{-1}	3179 cm^{-1}
e_1 peak amplitude	0.312	0.533	0.440	0.511
e_1 FWHM	579 cm^{-1}	438 cm^{-1}	632 cm^{-1}	574 cm^{-1}
e_2 peak position	3027 cm^{-1}	2769 cm^{-1}	3911 cm^{-1}	3620 cm^{-1}
e_2 peak amplitude	0.688	0.467	0.560	0.489
e_2 FWHM	771 cm^{-1}	483 cm^{-1}	741 cm^{-1}	686 cm^{-1}
e_3 peak position	3965 cm^{-1}	3474 cm^{-1}	5089 cm^{-1}	4719 cm^{-1}
e_3 peak amplitude	0.604	0.567	0.726	0.682
e_3 FWHM	935 cm^{-1}	1313 cm^{-1}	1440 cm^{-1}	1390 cm^{-1}
e_4 peak position	5464 cm^{-1}	4971 cm^{-1}	> 6500 cm^{-1}	6393 cm^{-1}
e_4 peak amplitude	0.455	0.482	NA	0.732
Volume (nm^3)	356.82	344.62	150.53	136.43

Table. 2-1. Peak position, amplitude and FWHM for the fitted absorption spectra. All transitions amplitudes are normalized using $e_1 + e_2 = 1$. The 4^{th} peak for the spherical dots with band edge at 3220 cm^{-1} is outside the range of the absorption spectrum, thus not available. The volume for the tetrahedral dots were calculated as regular tetrahedra, with average measured edge length 14.3 nm and 10.5 nm from TEM. The volume for the spherical dots is calculated using average radii of 4.4 nm and 3.35 nm.

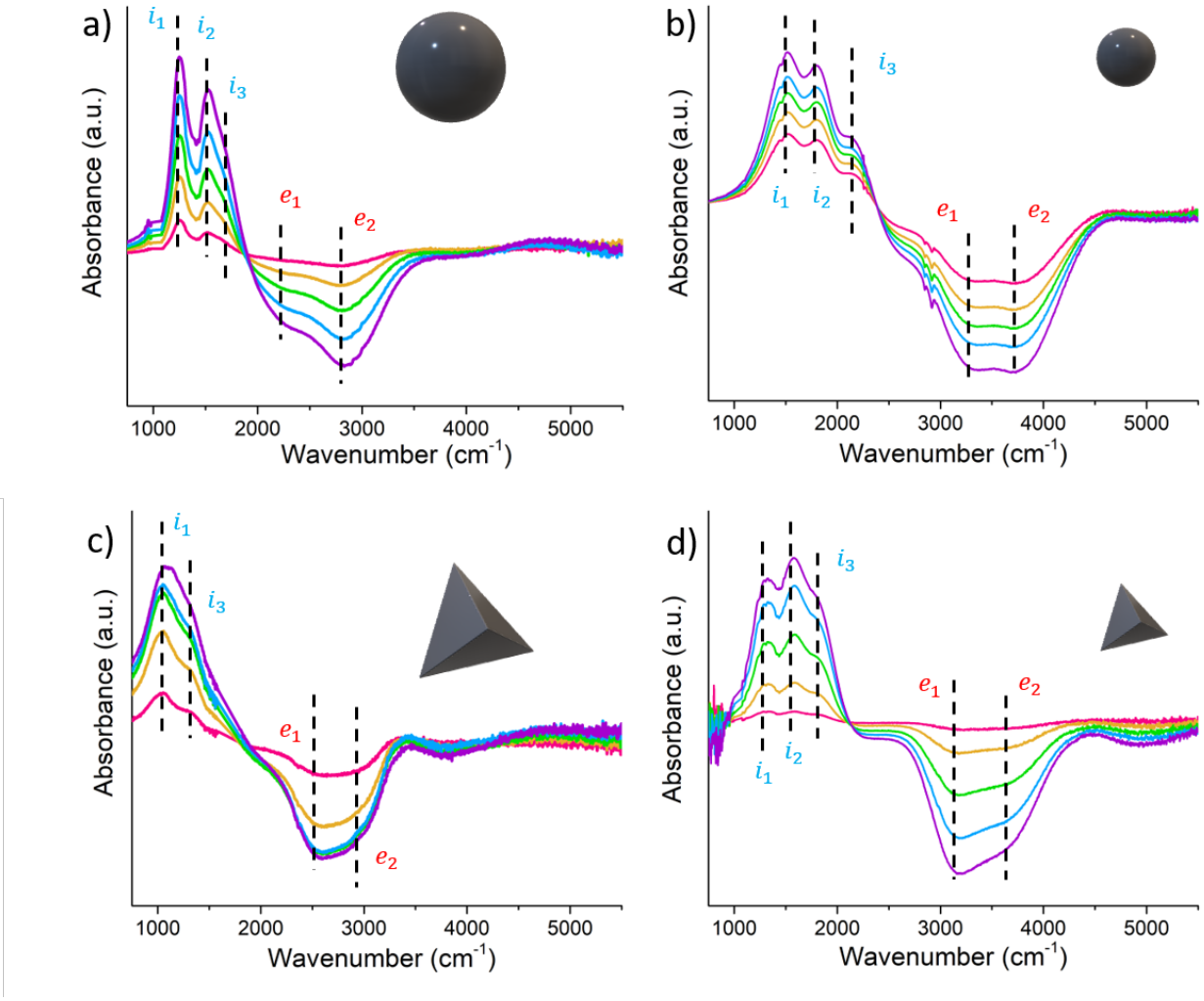

Fig. 2-6. a-d). Spectroelectrochemistry of spherical HgTe QDs with absorption edges at 2527 cm^{-1} and 3220 cm^{-1}, and tetrahedral dots with edges at 2434 cm^{-1} and 3179 cm^{-1}. The potential is measured against an Ag reference electrode, with voltage from -0.1 V (violet) to -0.3 V (red). The positions of the intraband (i_1, i_2, i_3) and interband (e_1, e_2) transitions are indicated.

2.4 Fine structure of the HgTe CQDs

Further information was sought by performing spectroelectrochemistry where the absorbance of CQD films is measured in an electrochemical cell. Fig. 2-6 shows the difference spectra as a function of reducing potentials and displays the increasing intraband absorption and the bleached interband absorption as electrons are added to the CQDs.[13,14] The samples are made from the previous CQD samples and drop cast as a CQD film on the flat end of a polished stainless-steel rod. The films are cross-linked with an ethanedithiol/HCl solution, and the rod is inserted into an electrochemical cell, with an Ag reference and Au counter electrode. The face of the rod is pressed gently against a CaF_2 or NaCl window, leaving a thin layer of electrolyte. Two solvents (dimethyl sulfoxide, DMSO and acetonitrile) and electrolyte (tetrabutylammonium perchlorate) are used, in order to minimize the solvent absorption features overlapping with the intraband peaks. The bias potential is applied using a bipotentiostat with the cell placed inside an FTIR spectrometer. The background spectrum of the QD film is taken at +0.1 V vs Ag/AgCl, where the films are typically undoped as evaluated by the Faradaic current. The difference spectra are taken as a function of potential from -0.1 V to -0.3 V. (Fig. 2-6).[25]

The spectra are each fitted with 5 gaussians and shown in Fig. 2-6 with peak positions tabulated in Table 2-2. An example for the fit is shown in Fig. 2-7. The interband region shows two simultaneous bleaches corresponding to the first two transitions in the absorption spectrum. We note that the position of the bleached transitions are red shifted compared to the absorption in Fig. 2-7, and attribute this to the preferred reduction of the larger dots, which can shift the spectra within the inhomogeneous width. This is also shown in Fig 2-7a, with a smaller red shift about 100 cm^{-1} as the potential becomes more negative, as smaller dots are being reduced.

Keeping the first transition as 1Sh-1Se, the simultaneous bleach of the second transition confirms that the same electron state is involved, supporting the 2Sh-1Se assignment.

This second transition appears rather similar to the case of CdSe where it is assigned to the $2S_{3/2}$-$1S_e$.[3,26] It is noted that the second transition is only at about 500cm^{-1} (60meV) higher energy than the first one, and that it may therefore not be originating from the light hole band which is expected to be deeper for HgTe (150meV).[27]

Table 2-2	Spherical QD edge (2527)	Faceted QD edge (2434)	Spherical QD edge (3220)	Faceted QD edge (3179)
I_1 peak position	1256 cm^{-1}	1105 cm^{-1}	1459 cm^{-1}	1277 cm^{-1}
i_2 peak position	1511 cm^{-1}	NA	1811 cm^{-1}	1577 cm^{-1}
i_3 peak position	1675 cm^{-1}	1478 cm^{-1}	2190 cm^{-1}	1858 cm^{-1}
e_1 peak position	2174 cm^{-1}	2470 cm^{-1}	3192 cm^{-1}	3137 cm^{-1}
e_2 peak position	2828 cm^{-1}	2878 cm^{-1}	3819 cm^{-1}	3663 cm^{-1}

Table 2-2. Peak position of the intraband and interband transition shown in Fig. 2-7

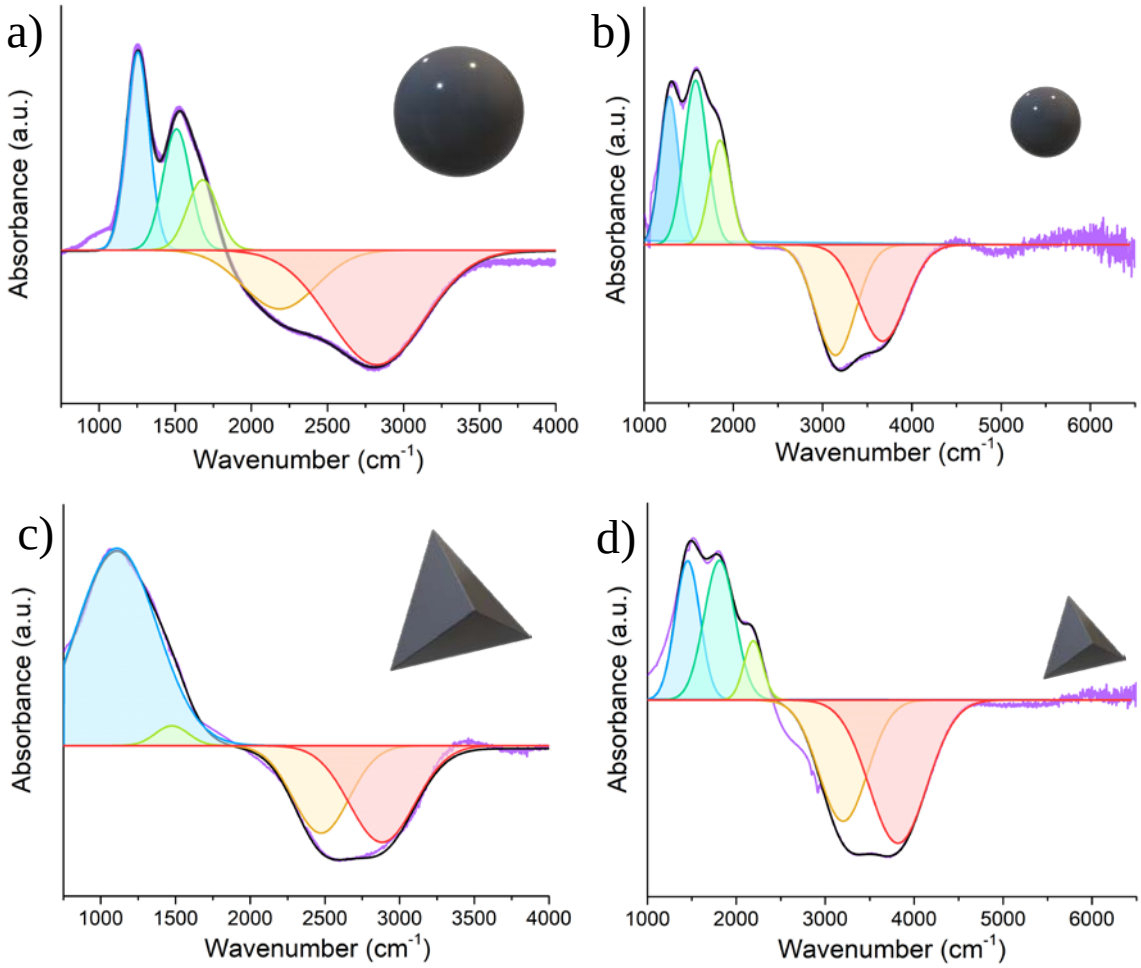

Fig. 2-7. a). Fitted spectroelectrochemical spectrum for the spherical HgTe QDs synthesized at 92°C b.) Fitted spectrum for the spherical HgTe QDs synthesized at 87°C. c). Fitted spectrum for the tetrahedral HgTe QDs synthesized at 92°C. d). Fitted spectrum for the tetrahedral HgTe QDs synthesized at 87°C.

The intraband spectra show further interesting features. There can be up to three peaks which are all assigned to the $1S_e$-$1P_e$ transitions. The position and strength of the three peaks is mostly

constant with increasing bias, suggesting that more than two electrons doping for the $1S_e$ was not reached within the bias range shown. Noting that the films become increasingly unstable when more negative potentials are applied, measurements at more reducing potentials will need to be done at low temperature in future work.

The intraband for the tetrahedral and spherical CQDs are different in significant ways. All three intraband transitions for the tetrahedral CQDs are lower in energy compared to the spherical CQDs with similar band-edge, while the splittings are also smaller. To understand the intraband 1Se-1Pe splittings, Delerue and Allan developed a tight-binding model[14,27] and showed the important role of spin-orbit coupling. They further showed that high symmetry spheres should show two transitions due to spin-orbit coupling, whereas cuboctahedrons would show 3 transitions. For the spherical case, the intraband spectra are rather similar to those previously reported[14] although the 3 peaks are better resolved here due to the improved size distribution. The three peaks are attributed to a cuboctahedron rather than purely spherical shape. In contrast, a perfect tetrahedron is predicted to have no splitting.[28] The qualitative argument is that the tetrahedral shape breaks rotational symmetry and eliminates spin-orbit splitting. The data roughly follow the prediction noting, however, that the splitting is reduced but not eliminated in our tetrahedral CQDs. At this stage, this could be assigned to the imperfect particle shape. This is supported by noting that that the larger dots, which are closer to tetrahedra, do show that the intraband transitions merge nicely together, leaving nearly a single peak as seen by comparing Fig. 2-6a and Fig. 2-6c.

We also note that the intraband transition energy is overall lower for the tetrahedral dots even though the intraband edge is at the same position. This support the previous notion that the 1P orbitals are less confined in the tetrahedral shape potential.

2.5 Conclusion

In summary, a synthetic protocol allows to control the shape the HgTe CQDs between spherical and tetrahedral while keeping them well dispersed. The more monodispersed spherical HgTe CQDs will be beneficial in further studies of transport in CQD films, where hopping or delocalization have been discussed. The tetrahedral shape arises in the presence of trioctylphosphine and with lower growth temperature. Given that TOPTe is a less reactive source of tellurium compared to TMSTe, the shape control is primarily attributed to the reduced reaction rate, although a specific effect of TOP is not ruled out. The interband spectroscopy shows that the tetrahedral shape should be advantageous in future photodetection studies since it provides a sharper absorption edge. Spectroelectrochemistry of n-doped CQDs allows to assign the first transitions and to study the intraband transitions. The decrease in intraband energy in tetrahedral CQDs compared with spherical dots having the same interband energy provides evidence for the weaker confinement potential experienced by the P orbitals in a tetrahedron. The intraband spectroscopy further highlights that the spin-orbit splitting of the $1P_e$ orbital is reduced in the tetrahedral shape.

2.6 Methods

Materials. HgCl2 (≥98%), iodine (99.99%), 1,2-ethanedithiol (≥98.0% (GC)), HCl (ACS reagent, 37%), tetrabutylammonium perchlorate (for electrochemical analysis, ≥ 99.0%), DMSO (99%), Acetonitrile (99.9%), iso-propanol (99%), ethanol (99%) and anhydrous solvents

(tetrachloroethylene, hexane, methanol) were all purchased form Sigma-Aldrich and used as received. Oleylamine (technical grade, 70%) was purchased from Sigma-Aldrich and directly transferred to the nitrogen glove box before opening. The purified oleylamine was dried under dynamic vacuum at 120 °C for 2−3 h and stored in a nitrogen glovebox. Bis-(trimethylsilyl)telluride (98%) was purchased from Acros and stored frozen in a nitrogen glovebox.

HgTe Synthesis. The standard synthetic protocol of HgTe CQDs is based on a previously reported method in ref 9. A portion of 54 mg $HgCl_2$ (0.2 mmol) and 8 mL oleylamine (OAm) is heated to 100^{o}C under nitrogen till all $HgCl_2$ solids have dissolved. The solution is then put under nitrogen and cooled to the desired temperature for nanocrystal growth (85-95 °C, with larger nanocrystals obtained at higher temperature). Meanwhile, a solution of 7μL or 21 μL of bis-(trimethylsilyl)telluride (TMS2Te, 0.025 mmol or 0.075 mmol) in 500 μL OAm , and 75 μL or 25 μL of 1 M trioctylphosphine telluride (TOPTe, 0.075 mmol or 0.025 mmol) in 500 μL OAm are prepared in a N_2 glovebox. The TMS_2Te solution is injected into the HgCl2 solution and heated at the injection temperature for exactly 1 min. Then, the solution of TOPTe is added dropwise over a period of 30 sec, followed by further reaction of 4.5 min. The reaction is quickly cooled by injection of 8 mL of anhydrous tetrachloroethylene (TCE) and cooled to room temperature under ambient conditions. This reaction is robust with respect to scaling in reaction content. After the reaction, the QDs are isolated by twice the addition of ethanol nonsolvent and subsequent centrifugation. The QDs are further washed with chlorobenzene with 0.1 M didodecyldimethylammonium bromide (DDAB), 0.1 M trioctylphosphine oxide and 0.1 M of dodecanethiol to increase QD stability, and subsequent precipitation with isopropanol and centrifugation. The resulting QDs are dispersed in chlorobenzene for optical measurements.

Optical Absorption. Infrared spectra were collected with a Thermo Nexus 670 FTIR in transmission mode with the film prepared on a ZnSe prism and the absorption measured in total internal reflection.

Transmission Electron Microscopy (TEM). TEM images were obtained on a FEI Technai Spirit or F30 microscopes at 300 kV.

Size Distribution Measurement. TEM images were analyzed manually, and its statistic is summarized histrogram and fitted with a gaussian function. The volume is calculated using the mean radius/apex to base distance assuming they are perfect spheres and tetrahedrons.

Photoluminescence (PL). Samples were prepared as drop-cast films on an aluminum substrate, if necessary, treated with ammonium sulfide to de-dope the QDs. The aluminum plate was pre-treated with (3-Mercaptopropyl) trimethoxysilane to increase the adhesiveness of dots with the surface. The film is then dried at 40^{o}C and treated with ethanedithiol/HCl solution.

The films are photoexcited by an 808 nm diode laser chopped at 100 kHz. The PL is measured with a step-scan FTIR with an MCT detector and a lock-in amplifier. The PL intensity at different wavelengths is normalized by taking the ratio of the signal from a blackbody source to the calculated blackbody spectrum at its temperature.

Spectroelectrochemistry. HgTe QD solutions in TCE are drop cast then crosslinked using ethanedithiol/HCl solution on a polished stainless streel surface. An Ag wire serving as a pseudo reference electrode and an Au counter electrode is placed in the electrochemical cell near the working electrode. The spectroelectrochemical cell is assembled and filled with 0.1 M tetrabutylammonium perchlorate (TBAP) in either DMSO or acetonitrile, to avoid overlap of the intraband and solvent peaks. The sample electrode is then pressed gently against the KBr or $NaCl_2$ window to minimize the infrared absorption from the electrolyte. Then the cell is placed in an

FTIR (Nicolet Magna IR 550). After flushing with N_2 for 30 min, infrared spectra are measured in reflectance mode. We first characterize the cyclic voltammetry with a potentiostat. Then, we set the potential +0.1 V to take the background. Then the difference absorption spectrum is taken at potentials from -0.1V to -0.3V, as the difference. A new background was taken before each measurement. We note that, with potentials more negative than -0.5V, the film became permanently altered, unable to return to its initial state even after un-doping electrochemically.

2.7 Appendix

HgTe synthesis with 0.050 mmol TMSTe injection with 2 multiple injections

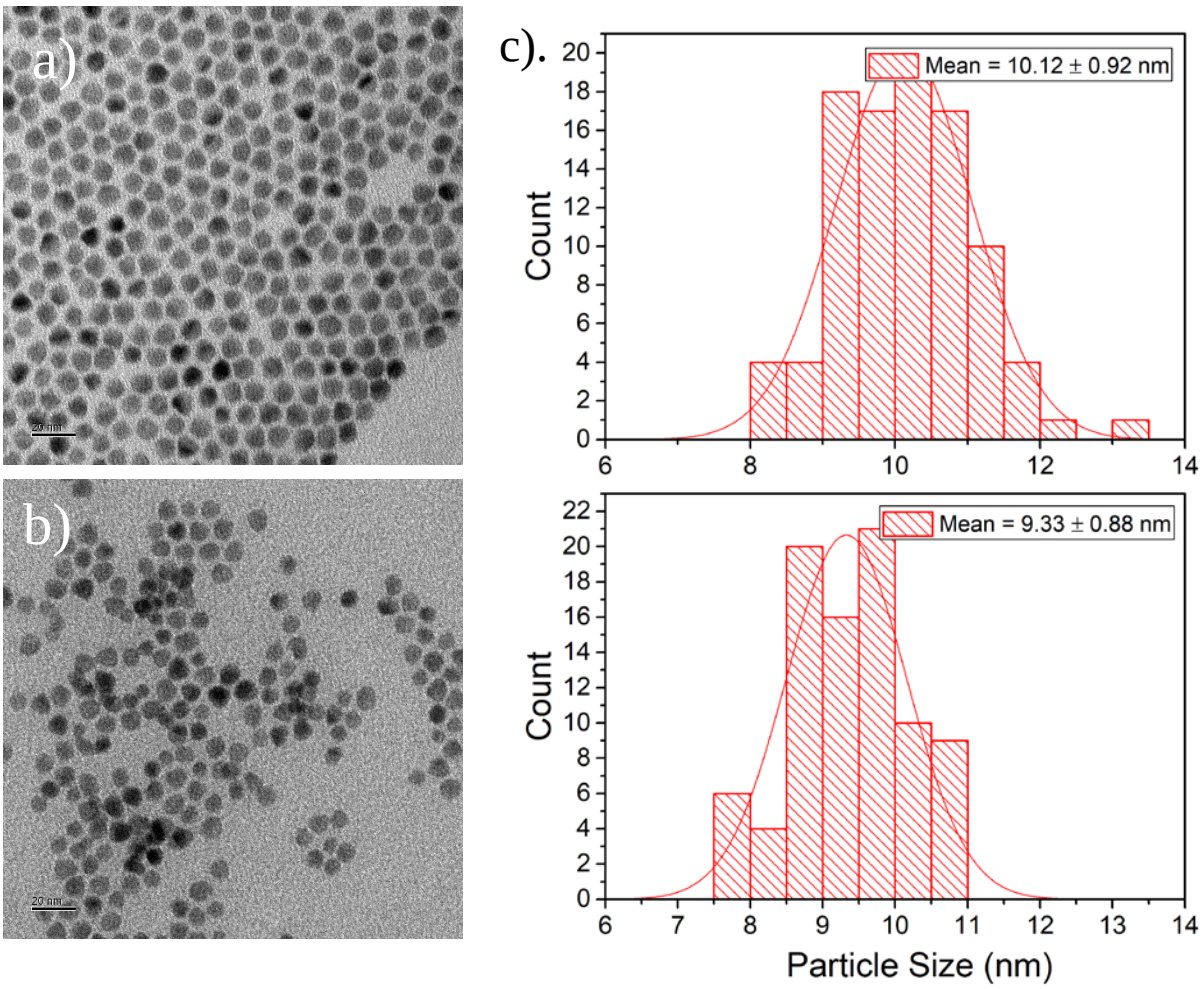

Figure. 2-8. a). TEM of HgTe QD of 1st injection of 0.05 mmol TMSTe after 40 sec at 90°C. b). 2nd injection of 0.05 mmol TMSTe into a). with the same reaction condition c). Size distribution of the HgTe QDs for a-d).

REFERENCES:

1. Sargent, E. H. Colloidal quantum dot solar cells. *Nature Photonics* 6, 133–135 (2012).
2. Wood, V. & Bulović, V. Colloidal quantum dot light-emitting devices. *Nano Rev.* 1, 5202 (2010).
3. Norris, D. & Bawendi, M. Measurement and assignment of the size-dependent optical spectrum in CdSe quantum dots. *Phys. Rev. B - Condens. Matter Mater. Phys.* 53, 16338–16346 (1996).
4. Peng, X. *et al.* Shape control of CdSe nanocrystals. *Nature* 404, 59–61 (2000).
5. Nair, P. S., Fritz, K. P. & Scholes, G. D. Evolutionary Shape Control During Colloidal Quantum-Dot Growth. *Small* 3, 481–487 (2007).
6. Kumar, S. & Nann, T. Shape Control of II–VI Semiconductor Nanomaterials. *Small* 2, 316–329 (2006).
7. Hines, D. A. & Kamat, P. V. Recent advances in quantum dot surface chemistry. *ACS Applied Materials and Interfaces* 6, 3041–3057 (2014).
8. Keuleyan, S., Lhuillier, E. & Guyot-Sionnest, P. Synthesis of colloidal HgTe quantum dots for narrow mid-IR emission and detection. *J. Am. Chem. Soc.* 133, 16422–16424 (2011).
9. Shen, G., Chen, M. & Guyot-Sionnest, P. Synthesis of Nonaggregating HgTe Colloidal Quantum Dots and the Emergence of Air-Stable n-Doping. *J. Phys. Chem. Lett.* 8, 2224–2228 (2017).
10. Tang, X., Ackerman, M. M. & Guyot-Sionnest, P. Thermal Imaging with Plasmon Resonance Enhanced HgTe Colloidal Quantum Dot Photovoltaic Devices. *ACS Nano* 12, 7362–7370 (2018).

11. Rogach, A. L. *et al.* Colloidally Prepared CdHgTe and HgTe Quantum Dots with Strong Near-Infrared Luminescence. *Phys. status solidi* 224, 153–158 (2001).

12. O'Connor, É. *et al.* Near-infrared electroluminescent devices based on colloidal HgTe quantum dot arrays. *Appl. Phys. Lett.* 86, 1–3 (2005).

13. Chen, M. *et al.* High Carrier Mobility in HgTe Quantum Dot Solids Improves Mid-IR Photodetectors. *ACS Photonics* acsphotonics.9b01050 (2019). doi:10.1021/acsphotonics.9b01050

14. Hudson, M. H. *et al.* Conduction Band Fine Structure in Colloidal HgTe Quantum Dots. *ACS Nano* (2018). doi:10.1021/acsnano.8b04539

15. Lee, J. W., Kim, D. Y., Baek, S., Yu, H. & So, F. Inorganic UV-Visible-SWIR Broadband Photodetector Based on Monodisperse PbS Nanocrystals. *Small* 12, 1328–1333 (2016).

16. Li, H. *et al.* Size- and shape-controlled synthesis of PbSe and PbS nanocrystals via a facile method. *CrystEngComm* 12, 1127–1133 (2010).

17. Abel, K. A., Shan, J., Boyer, J. C., Harris, F. & van Veggel, F. C. J. M. Highly photoluminescent PbS nanocrystals: The beneficial effects of trioctylphosphine. *Chem. Mater.* 20, 3794–3796 (2008).

18. Yang, Z. & Klabunde, K. J. Synthesis of nearly monodisperse palladium (Pd) nanoparticles by using oleylamine and trioctylphosphine mixed ligands. *J. Organomet. Chem.* 694, 1016–1021 (2009).

19. Keuleyan, S. E., Guyot-Sionnest, P., Delerue, C. & Allan, G. Mercury telluride colloidal quantum dots: Electronic structure, size-dependent spectra, and photocurrent detection up to 12 μm. *ACS Nano* 8, 8676–8682 (2014).

20. Liu, L. *et al.* Shape control of CdSe nanocrystals with zinc blende structure. *J. Am. Chem.*

Soc. 131, 16423–16429 (2009).

21. Peng, Q., Dong, Y., Deng, Z. & Li, Y. Selective synthesis and characterization of CdSe nanorods and fractal nanocrystals. *Inorg. Chem.* 41, 5249–5254 (2002).
22. Shieh, F., Saunders, A. E. & Korgel, B. A. General shape control of colloidal CdS, CdSe, CdTe quantum rods and quantum rod heterostructures. *J. Phys. Chem. B* 109, 8538–8542 (2005).
23. Ithurria, S. & Dubertret, B. Quasi 2D colloidal CdSe platelets with thicknesses controlled at the atomic level. *J. Am. Chem. Soc.* 130, 16504–16505 (2008).
24. Yang, Y. A., Wu, H., Williams, K. R. & Cao, Y. C. Synthesis of CdSe and CdTe Nanocrystals without Precursor Injection. *Angew. Chemie Int. Ed.* 44, 6712–6715 (2005).
25. Chen, M. & Guyot-Sionnest, P. Reversible Electrochemistry of Mercury Chalcogenide Colloidal Quantum Dot Films. *ACS Nano* 11, 4165–4173 (2017).
26. Zorman, B., Ramakrishna, M. V. & Friesner, R. A. Quantum confinement effects in CdSe quantum dots. *J. Phys. Chem.* 99, 7649–7653 (1995).
27. Allan, G. & Delerue, C. Tight-binding calculations of the optical properties of HgTe nanocrystals. *Phys. Rev. B - Condens. Matter Mater. Phys.* 86, (2012).
28. contact Prof. Delerue, private communication.
29. Zhang, H.; Guyot-Sionnest, P. Shape-Controlled HgTe Colloidal Quantum Dots and Reduced Spin–Orbit Splitting in the Tetrahedral Shape. *J. Phys. Chem. Lett.* **2020**, *11* (16), 6860–6866. https://doi.org/10.1021/acs.jpclett.0c01550.

Chapter 3: Electrical Properties of HgTe QDs with High Carrier Mobility

In Chapter 2, I used electrochemical spectroscopy to measure the intraband and interband spectrum of quantum dot films. One improvement is the development of the synthetic protocol using different ratios of TMSTe and TOPTe to improve the size distribution of HgTe CQDs. This leads naturally to a desire to perform more detailed studies on the carrier transport properties on the better size distributed CQDs. Fundamentally, the transport mechanisms in disordered system like CQD films are not yet well studied. Prior research have showed 'band-like' transport of CQDs which means that the mobility increases as temperature decreases, and it raised questions about delocalization and hopping mechanism inside the CQD films. However, the mobility may still be limited by the size distribution, and the transport at lower temperature is still subject to debate.

From the perspective of making detectors, high mobility enables more efficient carrier extraction and higher responsivity by increasing the current from the photogenerated charges. The effect of mobility on detectivity is less straightforward, as high carrier mobility could also contribute to a nosier device. Therefore, a fundamental understanding of the noise structure of HgTe CQD films would be necessary to reduce the noise in photodetection.

In this chapter, I separate the measurements of the device into two parts. In Part I, I present the measurement of mobility and conductance of the high mobility HgTe film and the transport properties of this film with different variables including temperature, electric field, and channel length. In Part II, I discuss the noise structure of the HgTe film and relationship of noise and conductivity.

PART I

3.1 Introduction

Colloidal Quantum Dots have shown many potentials in optoelectronics, including photodetection, light-emitting diodes, and field effect transistors, through the tunability of their optical and electronic properties.[1,2] The performance of these optoelectronic devices requires good electrical transport of the carriers inside the CQD films, which requires a high enough electron mobility to collect all carriers. At present, 10 cm^2/Vs is considered such a high mobility.[3,4] High electron mobility in a film of CQDs can be achieved through means of ligand exchange, surface passivation, lowering size dispersion, and doping control.[3,5] An electron mobility greater than 10 cm^2/Vs has been observed in systems such as PbSe and CdSe, comparable to the best organic semiconductors.[6,7] A negative temperature dependence of the mobility has also been observed for these high mobility CQDs at room temperature, demonstrating 'band-like' transport behavior.[4,7] The question remains whether CQDs can exhibit metallic transport, i.e. have a finite conductance at T = 0 K. So far, the only report on finite mobility at 0 Kelvin is through sintered, highly doped ZnO nanocrystals.[8,9] CQDs films for which transport is state-resolved have never been observed to have high mobility at low temperatures, though there is discussion of some delocalization at these temperatures.[10]

Bulk HgTe is a zero-band gap semimetal, therefore the energy gap of HgTe CQDs can be tuned across the entire infrared spectrum. The solution processability also provides a cheap alternative to the conventional infrared photodetectors, which is currently limited by high manufacturing cost arising from the requirement of molecular beam epitaxy (MBE) and flip-bonding. HgTe CQD photodetectors have shown good detectivity both in short-wave (1-2 um) and mid-wave (3-5 um) region, reaching background limited infrared performance (BLIP) at low temperature. Thus,

improving the electrical transport properties will be important to further improve HgTe CQD infrared detectors.

The questions are to find the conditions where nanoparticle films would reach metallic behavior at low temperatures, and how to measure this delocalization across quantum dots? Here, focusing on HgTe CQDs following the work by Lan et al., who recorded an electron mobility of 8 cm^2/Vs measured using a hybrid ligand transfer to reduce the interdot distance.[10] HgTe CQDs have the benefit of having distinctively defined $1S_e$ and $1P_e$ states, to identify state-resolved transport, and should benefit from the improvement in synthesis and a size distribution below 10%. Moreover, controlling the electronic doping level is relatively simple if not yet fully controlled.[11,12] Summarizing the prior state of the art, films of HgTe CQDs of ~ 14 nm diameters have shown 'band-like' transport above 80 K with high electronic mobility of ~ $10cm^2/Vs$, but the mobility at lower temperatures dropped to less than 0.1 cm^2/Vs. These results were explained by thermally activated electron hopping between dots, but also provided some evidence on the delocalization of electron between 2-3 dots. This work reports on the detailed transport properties of more monodispersed HgTe CQDs using similar processing, and it also studies the effect of the electric field on the electron transport at low temperatures.

3.2 Motivation

Generally, electronic systems can be characterized into metals and insulators. A system is classified as metallic if it shows an increase in carrier mobility as temperature decreases down to 0 K. In ordered systems which have a band structure, the electronic states are delocalized, and metallic behavior happens when a band is partially filled, unless strong electron correlations lead to a Mott insulator.[3,4,13] In a band conductor, the conductivity typically increases with decreasing temperature, as less and less phonons collide with the electrons, such that the electron mean-free path increase. Amorphous metals also exist, with metallic behavior down to the lowest temperatures. Tunneling across junction can also be ohmic without any activation, down to the lowest temperatures. The behavior of poor metals and amorphous metals is framed in the context of the electronic mean-free path. The Mott-Ioffe-Regel limit is when the electronic mean-free path is longer than the interatomic distance, and this is considered sufficient to have metallic behavior. The wavefunction may then be delocalized, due to coherence between sites or atoms. The delocalization of the electronic wavefunction may however not be permanent, as collisions with phonons can de-phase the states. As temperature is increased, the fluctuation of the delocalized state becomes larger, and one recovers something like the band-like behavior.

For insulators, the transport is always thermally activated with conductance increasing with temperature. Applying a large electric field can lead to space charge limited transport or the extraction of charges from deep states, and this complicates the temperature dependence. Nevertheless, in the limit of zero electric field, an insulator has zero conductivity at zero temperature.

The question addressed here is, for semiconductor nanocrystals (quantum dots) films, which have some electrical properties similar to those of bulk semiconductors, what is the necessary criterion

for electrical transport to be metallic or insulating.

Before quantum dots, metal nanoparticles such as silver or gold nanocrystals of the size of 4-5 nm have shown metallic transport, staying ohmic and with steady electrical conductivity as temperature is brought close to 0K.[14–16] However, quantum dots have never shown such metallic behavior, where the first synthesized CdSe CQDs was not even ohmic at room temperature.[17] By exchanging long ligands with a shorter chain amine, an ohmic conductivity was finally observed with electron mobility of the order ~ 10^{-2} cm^2/Vs.[18,19] However, the transport of the CdSe film behaves like an insulator, with the electron mobility decreasing with decreasing temperature.[19,20] Through the past decades, various ligand exchange techniques to reduce interdot distance and methods to improve interdot coupling, improved the mobility greater than 10 cm^2/Vs to this day.[6,11] However, it is still far from reaching metallic transport, despite showing "band-like" behavior which refers to an increase of carrier mobility with decreasing temperatures, over some temperature range. [4,7,12]

One major difference between quantum dots and metallic nanoparticles arises from the density of states between the two systems. Metallic NCs have a high density of states which are filled with electrons, with a number of electrons effectively determined by the number of atoms. Thus, though the probability for any electron in a single state to hop between the nanoparticles may be low, a metallic transport can be observed due the high density of possible channels between them. The conductance across the metal nanoparticles can reach the quantum conductance, and this is a threshold for establishing coherence between two particles, which is the Mott-Ioffe-Regel limit. In a simple square lattice, the square resistance becomes the quantum resistance as well. The conductivity defined by the thickness of the film is $\sigma = e^2/hd$, where d is the particle size, which is also the particle center to center distance.

For quantum dots which have only two spin-orbital states for electronic transport, for example $1S_e$, the situation is quite different. As they can be doped around 0 ~ 1 electrons, the number of channels between the dots is low, therefore metallic conductivity if the electronic transmission is of order unity, and therefore the coupling between dots is large and energy difference is small, in effect if coherence is near perfect. This can only be interpreted as the time for electron to tunnel through the dots to become extremely short. For example, quantum dots such as CdSe, HgSe and HgTe have such a single defined $1S_e$ state with a defined spin, there is only a single channel for the electrons to hop through the quantum dots. CQDs with 4x-degenerate $1S_e$ states such as PbSe can have up to 16 channels, which is still quite small compared to metal nanocrystals.[11,17,21,22] Therefore, we cannot expect metallic transport to arise in quantum dot systems easily, unlike the metal nanoparticles, and one needs to work harder to reduce the size disorder and increase the coupling between particles.

3.3 Theory on Metallic Transport

To estimate the minimum mobility required for the quantum dots to show a metallic conductance, we start with the Mott-Ioffe-Regel theory for amorphous metals.[23,24] To observe metallicity, it is required that the mean free path of the electrons to be comparable to the interatomic distance. For a system of quantum dots, the mean free path must be equal to the distance between the quantum dots.

Considering the Drude model of metallic transport

$$\mu_{Drude} = \frac{e\tau_0}{m^*}$$

where τ_0 is the average scattering time of electrons.

The metallicity limit can be reached if the scattering time exceeds the coherence of the electrons between dots, i.e.

$$\tau_0 > \frac{J}{\hbar} = \frac{\left(\frac{\hbar^2}{2m^* d^2}\right)}{\hbar} = \frac{\hbar}{2m^* d^2}$$

where J is the coupling energy between the quantum dots. The value of $J = \frac{\hbar^2}{2m^* d^2}$ is derived from a tight-binding linear band structure and is used only to provide an estimate. This gives the carrier mobility of dots needed to reach metallic transport.

$$\mu > \frac{ed^2}{2\hbar}$$

With on average 1 electron per dot, this also implies that the interdot resistance reaching a value of the order of the quantum resistance, consistent with the prior discussion.

$$R_{NC} = \frac{1}{\sigma d} = \frac{1}{ne\mu d} = \frac{2\hbar}{e^2 n d^3} = \frac{2\hbar}{e^2}$$

Taking HgTe dots with diameter of 15 nm, this gives μ = 1700 cm^2/Vs. The best mobility recorded so far is ~ 7 cm^2/Vs, less than 200 times lower than needed. Thus, while the discussion is only semi-quantitative, it highlights the fact that a mobility of 10cm2/Vs is still, in principle, very far from the value needed to reach metallic transport.

To reach higher mobility, it will be necessary to both improve the dot-to-dot coupling energy and to reduce disorder between dots. This can be done by better size dispersion, increasing the size of quantum dots, and reduce the interdot distance.

1. Size Dispersion ($\delta r/r$)

The size dispersion has a direct relation with the distribution of energy levels. We can model the tunneling probability of the electrons from one dot to another as electrons tunneling through a barrier with height V.

$$P = e^{-2(2mV/\hbar^2)^{1/2} l} = e^{-\beta l}$$

where l is the barrier width, β can be viewed as the attenuation of the electron wavefunction out

of the dots.

If the electron transport process is thermally activated with some barrier, we expect $P = e^{-\beta l - \frac{E_a}{k_B T}}$, where E_a is the activation energy for the electron transfer. E_a constitutes two components. The activation energy arises from the disorder of the energy levels ΔG as the energy levels of $1S_e$ states are different due to variation in size, and from the reorganization energy λ due to the charge reorganizing between the quantum dots. Thus, we expect that reducing the size dispersion will reduce the energy disorder ΔG between quantum dots.

Currently, HgTe CQDs are dominated by the energy disorder ΔG. For example, dots around the size of 10 nm are estimated to have ΔG = 17 meV where λ = 7 meV.

Size of CQDs have an indirect relation with the energy disorder. This can be understood from two aspects. First, increasing the size of quantum dots reduces the effect of energy variation for the same size distribution of dots within the film. Since the energy level of the quantum dots scales with $\sim \frac{1}{r^2}$, the effect on the change in energy levels is related to the size variation is proportional to $\sim \frac{1}{r} \delta r$. Thus, δr contribute less to the change in energy as the radius increases. Secondly, for charge transfer between the quantum dots, one crucial energy barrier is the charging energy due to the electron-electron repulsion. This charging energy is related to the dielectric constant of the dot matrix, and proportional to $\sim \frac{1}{r}$, thus larger dots reduce the energy needed for the charge to reorganize.

2. Interdot Distance (l)

The interdot distance can be understood as the length of the barrier between the wavefunctions between the two dots. It is expected that the interdot distance is dominated by the length of surface ligands, thus replacing long chain ligands with shorter one could improve the carrier mobility for

the same dots. Indeed, research has shown that replacing long chain amine ligands with short chain thiol ligands improve mobility by three orders of magnitude, and further replacing them with inorganic/hybrid ligands allows mobility of up to 7 cm^2/Vs. Right now, the interdot separation for the inorganic ligands is around 0.5 nm, close to the diameter of atoms. The zeta-potential measured from DLS (Dynamic Light Scattering) have shown that the surface is largely stabilized by electrostatic charge. One would doubt if further shortening of the interdot distance is possible without the dots sintering and thus losing the quantum confinement within a single dot, causing a broadening of the energy levels of the electron states, and losing the state-resolved requirement.

3.4 Improved Synthesis of High Size Dispersion CQDs

The synthesis of non-aggregated HgTe CQDs was first developed by Shen et al., though the size dispersion of these CQDs was moderate, with mobility of these dots at the order of 10^{-2} cm^2/Vs.[25] Following the hybrid ligand exchange protocol of HgTe developed by Lan et al., the mobility improved by two orders of magnitude and reaches 7 cm^2/Vs. However, to enable the study of the HgTe QDs at high conductance, we modified the synthetic protocol by Zhang et al. and the hybrid ligand exchange protocol developed by Lan et al.[11,26–28] A more uniform size distribution has been found previously by using a two-step injection method of first TMSTe followed by TOPTe into a solution of $HgCl_2$ dissolved in oleylamine. To further increase the size uniformity, we changed the standard $HgCl_2$ precursor to a more reactive 1:2 mixture of $Hg(OAc)_2$: $HgCl_2$. This ratio of Hg $(OAc)_2$: $HgCl_2$ is chosen as it is the most reactive precursor that produces a stable dot solution. A further increase in $Hg(OAc)_2$ results in aggregation during the nucleation phase and thus is unable to separate. A 6% size dispersion can be reached with a sharp intraband absorption feature.

After the synthesis, the solution is cleaned once and transferred to a polar solution of DMF, following the method by Chen et al. To remove the impurities and increase size uniformity in the polar solution, we redispersed the precipitate of HgTe in DMSO. Instead of directly using the polar solution for drop-casting, we add 10 ul of 2-mercaptoethanol and re-precipitate it with Toluene. The final solution is dispersed in DMSO and drop-casted on the FET at 70^{o}C to prevent aggregation during solvent evaporation. A polymer layer of polyvinyl butyral (PVB) is cast on the dot film and dried under nitrogen at 70^{o}C overnight to ensure stable doping during the measurements.

The absorption spectrum, TEM image and size dispersion are shown in the Appendix.

3.5 Transport of HgTe CQDs at High Temperatures

1. Mobility measurement

The mobility is measured using a bottom-gated field-effect transistor (FET). The current is measured with a HgTe CQD film drop-casted across the gold source (S) and drain (D) electrodes with different gap lengths. The length of the FET channel was set to three values, 10 μm, 5 μm, and 2 μm to investigate the effect of the channel length upon the CQD film, where the bias voltage is applied depending on the length of the FET channel, as such, the electric field is normalized cross with respect to the length of the channel. The width of the FET channel is set to 500 μm, 250 μm and 100 μm, making the length-to-width ratio constant. This ensures that the conductance of the HgTe film is directly comparable across the three devices.

The highest mobility that has been previously measured is the 13.1 nm HgTe films with hybrid ligand exchange, Chen et al. reported mobility up to 7 cm^2/Vs. In this study, with a modified synthesis that produces a slight increase in dot size of 14.2 nm, and a different film processing, the mobility measured directly from the FET at 70 K is close to 30 cm^2/Vs for a gap length of 10 μm, and over 62 cm^2/Vs for gap length of 2 μm, shown in Fig. 3-1a). Despite the 70°C annealing, the FET still maintains state-resolved transport. We also note that the mobility shows a strong channel length dependence, increasing with narrower channels. This contrasts with the result reported by Lan et al., where the author reported that gap length has no significant impact on device performance. A possibility is that the HgTe film in the present experiment have a greater delocalization, which will be discussed further below.

Fig. 3-1b) shows the plot of FET mobility at temperature ranges from 4 K to 298 K across devices of the three gap lengths. As previously reported, the mobility above 60 K or 70 K, depending on the sample, shows a 'bank-like' transport of negative $\partial\mu/\partial T$. The transport at these high

temperatures is theorized as following activated hopping of electrons across dots, which follows the Marcus electron transfer model.

Fig. 3-1b). also shows the best fit of the Marcus model above 70 K, assuming a reorganization energy of λ = 4.2 meV.

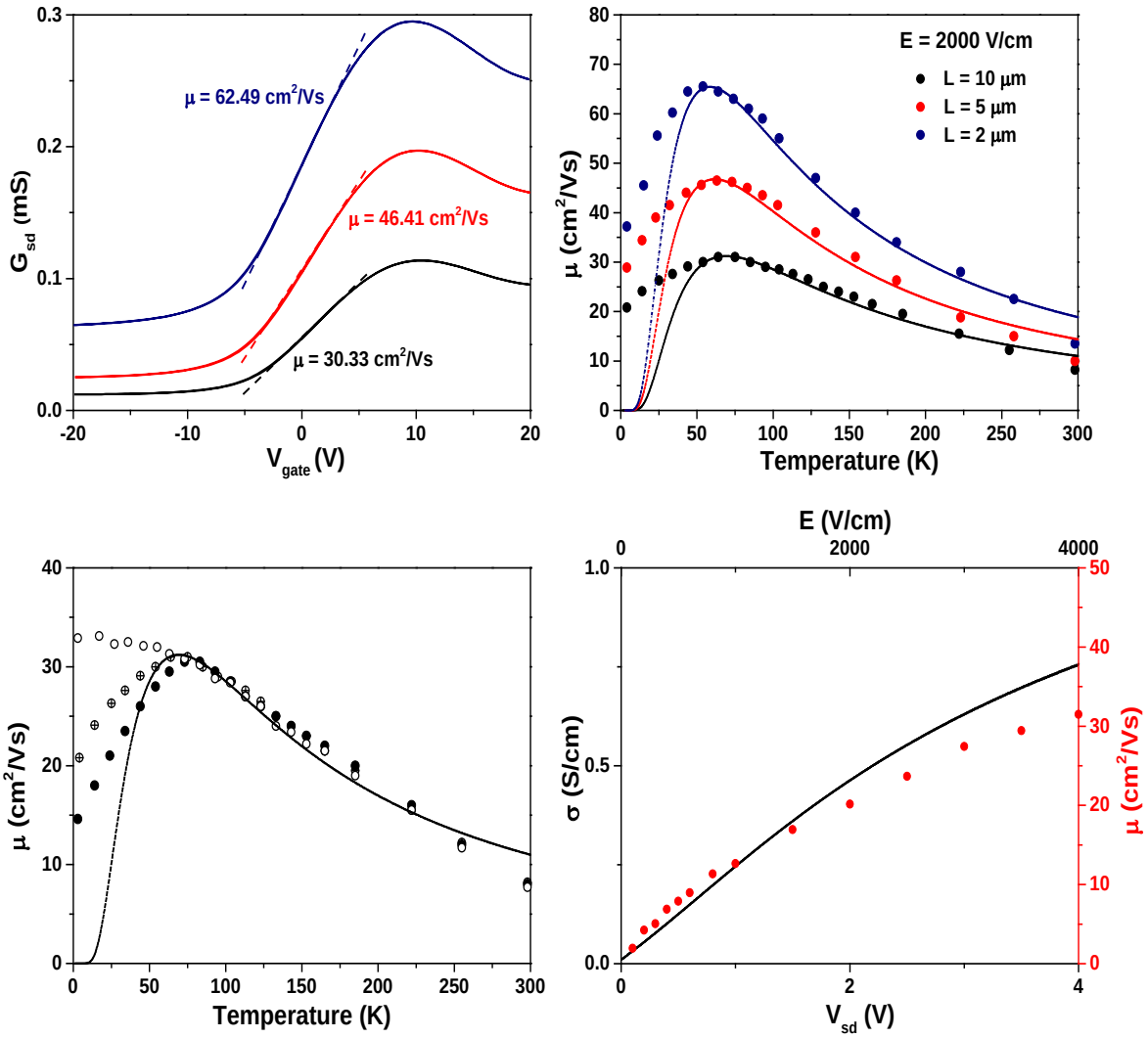

Fig. 3-1 a). The conductance curve of FETs (at 70 K) with different gap sizes shows gap-dependent conductance. The differential mobility of 1Se electrons is shown as the dash lines. Black: 10 μm, Red: 5 μm, Navy: 2 μm. b). Differential mobility measured from 4K to 298K, with different gap lengths. The solid dots are differential mobility measured from the conductance curve on the FET, where dashed lines are the theoretical behavior based on the Marcus Model. (See Table 3-1) c). Mobility of the electrons at different bias voltage, showing a divergence at low temperatures. Solid: 1 V, Cross: 2 V, Open: 4 V. d). Measured conductance (Black Line) and differential mobility (Red Dot) with different bias voltages at 4 K. Both measurements show a voltage bias-dependent behavior at low temperature.

2. The Marcus Model

A hopping model of electron between quantum dots can be described by the Marcus Theory:[29,30]

$$\mu(T) = \frac{2\pi}{6}\,\frac{e(d+l)^2}{\hbar}\,\frac{J^2}{\sqrt{4\pi\lambda(k_BT)^3}}exp\left(\frac{-(\lambda+\Delta G)}{4\lambda k_BT}\right)$$

where d is taken to be the dot diameter of 15 nm, l is the dot-to dot distance taken to be 0.5 nm, the key parameters are J the electronic transfer integral or coupling energy, λ the reorganization energy, and ΔG is energy disorder.

The reorganization energy is the change in polarization of the material due to charge transfer. One estimate of this energy is using the electron-electron repulsion, assuming the dots are an isolated sphere embedded in a uniform matrix of dielectric constant ε. This is given by

$$E_{c0} = \frac{e^2}{4\pi\varepsilon\varepsilon_0 r}$$

With a dot of $r = \frac{d}{2} = 7.5$ nm, the surrounding matrix with a dielectric constant $\varepsilon = 7.3$, using optical constant estimated from previous studies of HgTe CQDs exchanged after hybrid ligands. This estimate gives E_{c0} = 26.3 meV. However, this has no effect of dot-dot distance. A better estimate is to introduce the capacitance of a conductive sphere in a conductive shell with the insulating gap l. In this case,

$$E_c = \frac{l}{l+r}E_{c0} = \frac{e^2 l}{4\pi\varepsilon\varepsilon_0 r(l+r)}$$

using l of 0.5 nm, the estimated charging energy would be given as E_c = 1.64 meV.

Prodanovic et al have proposed another estimate of this reorganization energy given by[30]

$$\lambda = \frac{e^2}{4\pi\varepsilon_0}\left(\frac{1}{r} - \frac{1}{2(r+l)}\right)\left(\frac{1}{\varepsilon} - \frac{1}{\varepsilon_{st}}\right)$$

the difference is the introduction of the static dielectric constant ε_{st} into the equation, where ε is the optical dielectric constant in the infrared region. The estimation of ε_{st} for the film of CQDs may take hints from the dielectric constant from bulk HgTe. The static dielectric constant of bulk HgTe ε_{st} = 21 and the optical dielectric constant ε = 15.6. Therefore, taking CQDs films as less dense HgTe, we scale the ε_{st} by the same ratio, thus taking the value of ε = 9.8. With similar assumptions of r and l, the estimated reorganization energy is approximately λ ~ 4.2 meV. The discrepancy of the estimates depends on how polarizable the dot matrix is, as more polarizable matrix result in smaller λ.

Since λ can be estimated, the only fitting parameters are the coupling energy J and energy disorder ΔG. These two parameters are then extracted from the experimental data through fitting the mobility measurement above 70 K, and they are given in Table 3-1.

Table 3-1: Fitting Parameters for the Marcus Model and Mobility Measurements

Gap Length	*Mobility (70K)*	*J*	λ	ΔG
10 μm	*30.3 cm^2/Vs*	*2.1 meV*	*4.2 meV*	*7.9 meV*
5 μm	*46.4 cm^2/Vs*	*2.2 meV*	*4.2 meV*	*7.3 meV*
2 μm	*62.5 cm^2/Vs*	*2.5 meV*	*4.2 meV*	*7.0 meV*

From the fit to the Marcus Model, as the electrode gap gets shorter, J increases and ΔG decreases. Given that the drop-cast is done on three devices built on the same FET, such a variation cannot be easily explained. Instead, it is suggested that it reflects a microscopic non-uniformity inside the device. As the HgTe CQDs form delocalized domains in the film with a variation in size, and the delocalization get closer to the gap length, more of the transport is through the regions with the largest domains, and thus leading to a larger mobility. However, the exact size of such delocalized domains would need to be characterized through more experiments.

It should be noted that the fitting of the Marcus Electron Transfer Model extends only to approximately 70 K, where the measured FET mobility does not approach zero, as the theory would suggest.

As shown in Fig. 3-1c), it is also seen that the measured mobility has a strong dependence on the source-drain bias applied during the measurement. Taking the device with a gap length of 10 μm at 4 K as an example, the measured mobility ranges from 0.2 cm^2/Vs at V_{sd} = 0.1 V, to over 32 cm^2/Vs at V_{sd} = 4 V, as shown in Fig. 3-1d). We also measured the conductivity of this device between 0 to 4 V bias, and it is consistent with the differential mobility measurement done using

the FET. Conductivity σ and mobility μ are related by $\mu = \sigma V_{dot}/ne$, where n is the number of carriers per dot and V_{dot} is the effective unit volume of each QD. The FET indicates n between 0.45 to 0.55 e^-/dot, and this gives $V_{dot} = 4000\ nm^3 \pm 400\ nm^3$. Assuming the dots are spherical with a diameter of 15 nm, this implies the packing fraction of the dots is between 39% to 47%, which is far from closed packed. This is also observed from the SEM image since a few empty gaps/cracks can be seen in the film.

When the source-drain bias is held at 4V during the mobility measurement, we do not see a drop in mobility at all as temperature decreases, which does not fit with any activated transport theory. This would mean that the HgTe CQD films behave as metallic conductors at high bias. However, since the transport of electrons below 60 K is clearly dependent on the field applied, we investigated further this voltage dependence below 60 K.

3.5 Transport of HgTe CQDs at Low Temperatures

1 Efros-Shklovskii Variable Range Hopping

At lower temperatures, the transport of the electrons in the film of HgTe CQDs is no longer ohmic. It is also observed that this transport deviates from the Arrhenius behavior, with a mobility that is always higher than predicted by the Marcus theory. This can be assigned to the variable range hopping (VRH) when electron can tunnel to dots further away from the nearest neighbor.[20]

A simple picture can be viewed from the perspective of electrons tunneling though nearby quantum dots.

Since tunneling of electrons to the nearest neighbor can be expressed as $T = e^{-\beta l}$, we need to consider the probability of tunneling through several dots. A constant $\xi = \frac{2d}{\beta l}$ is defined, which is called the 'localization length' in variable range hopping. Thus, for an electron tunneling through

one dot.

$$P = e^{-\beta l} = e^{-2d/\xi}$$

where ξ can be viewed as an exponential decay length of the electron wavefunction. Similarly, tunneling of the electron through n-dots can be expressed as

$$P^n = e^{-2nd/\xi}$$

Combining this probability with the activation energy ΔE_n for the nth dot, we can get the formula for the conductance between n dots.[13]

$$G \sim e^{-2nd/\xi} e^{-\Delta E_n/k_B T}$$

At high temperatures, we expect transport to be dominated by nearest neighbor hopping due to the term $e^{-2nd/\xi}$ being exponentially small. However, when the temperature is sufficiently low, $e^{-\Delta E_n/k_B T}$ is close to zero unless for dots with identical energy levels. Thus, a longer tunneling range becomes more probable.

The *Efros-Shklovskii* theory of variable range hopping predicts that the transport of electrons at low temperatures should follow

$$G \propto exp\left(-\sqrt{T^*/T}\right)$$

This VRH argument is purely a scaling argument, and it gives no prescription for the preexponential factor, which includes probability of tunneling through the barrier of surface ligands, as well as the attempt frequency of electron trying to tunnel. The argument is also limited to weak coupling between dots where the conductance varies by several orders of magnitude with temperature. Nevertheless, experimentally, HgTe CQD systems have shown transport that approximately follows the VRH theory at low temperatures.

The above argument has no dependence on the bias applied, and it is valid when the field is low. At high bias where eV between dots becomes larger than $k_B T$, the ES-VRH predicts a temperature

independent conductance such that

$$G \propto exp\left(-\sqrt{E^*/E}\right)$$

where E is the external field applied. Thus, the electron transport between CQDs is largely field driven, where the field helps to overcome the Coulomb barrier (instead of T) between CQDs and creates temperature independent transport. When E is much larger than E^*, electrons are always hopping to the nearest neighbors. This tends to be a conductance limit of VRH of $G \propto exp((-2d/\xi)$.

2. Conductance measurement

As the conductivity and mobility shows a strong electric field dependence when measured below 60 K, the question remains whether the transport of electrons at low temperatures follows the variable range hopping. Lan et al. reported that the mobility of the HgTe CQDs exhibited transport properties that deviates from the activated transport predicted by the Marcus Model, and more closely follow the Efros-Shklovskii Variable Range Hopping (VRH). The variable range hopping of electrons in CQDs at low temperatures have been seen in multiple systems, including CdSe, PbSe and HgTe.

The ES-VRH model predicts the transport of the electrons at low temperatures, along with the field and temperature dependence. In the limit of weak field, the conductance of electrons follows the formula $\sigma = \sigma_0 exp(-\sqrt{T^*/T})$. As VRH is a scaling argument, the preexponential factor σ_0 is related to the attempted frequency of tunneling through the barrier.

Experimentally, at low field, the FET derived differential mobility measurement is too noisy. Therefore, the conductivity is directly extrapolated from the IV curve, using the measurement at 70 K as a baseline, because the mobility is field independent at that temperature. Fig. 3-2a) shows the IV curve of the device with 10 um gap length, with temperature from 4 K to 62 K. We note

that the measured IV curve is strongly non-linear at 4 K, where it resumes to ohmic at 62 K. This is consistent with the observation that the mobility is strongly field dependent at 4 K, whereas this dependence vanishes above 62 K.

Taking the current density measured at fixed 20 mV bias voltage, we plot the conductivity against temperature up to 62 K, shown as red circles in Fig. 3-2b). We also show the conductivity measured at a fixed 2 V bias voltage as blue circles. The data demonstrates a trend towards zero conductance as temperature decreases, which is consistent with hopping transport. It also fits the ES-VRH shown as the black line in Fig 3-2b), with the T^* extrapolated from the model to be around 245 K. It shall be noted that the datapoint at 4 K deviates from the model by a factor of 2.3. This deviation can be partly explained by the thermal fluctuations of the cryostat at 4 K. Given that the bias applied is extremely small, we also believe that Joule heating is insignificant to cause this increase in mobility. A discussion on Joule heating follows further below.

The T^* is predicted by the ES-VRH model by $T^* = \beta e^2/(4\pi\varepsilon\varepsilon_0 k_B \xi)$. β is a numerical constant taken as 6.1 for two-dimensional transport. We used ε = 7.3 estimated using the optical dielectric constant of HgTe CQD films. ξ is the electron localization length, using T^* = 245 K, we estimate this localization length ~ 56.9 nm, which is about 4 dot diameters. Though this estimate is subject to disagreement due to the choice of β and ε used in this model, the data affirm the validity of the VRH transport at low temperatures.

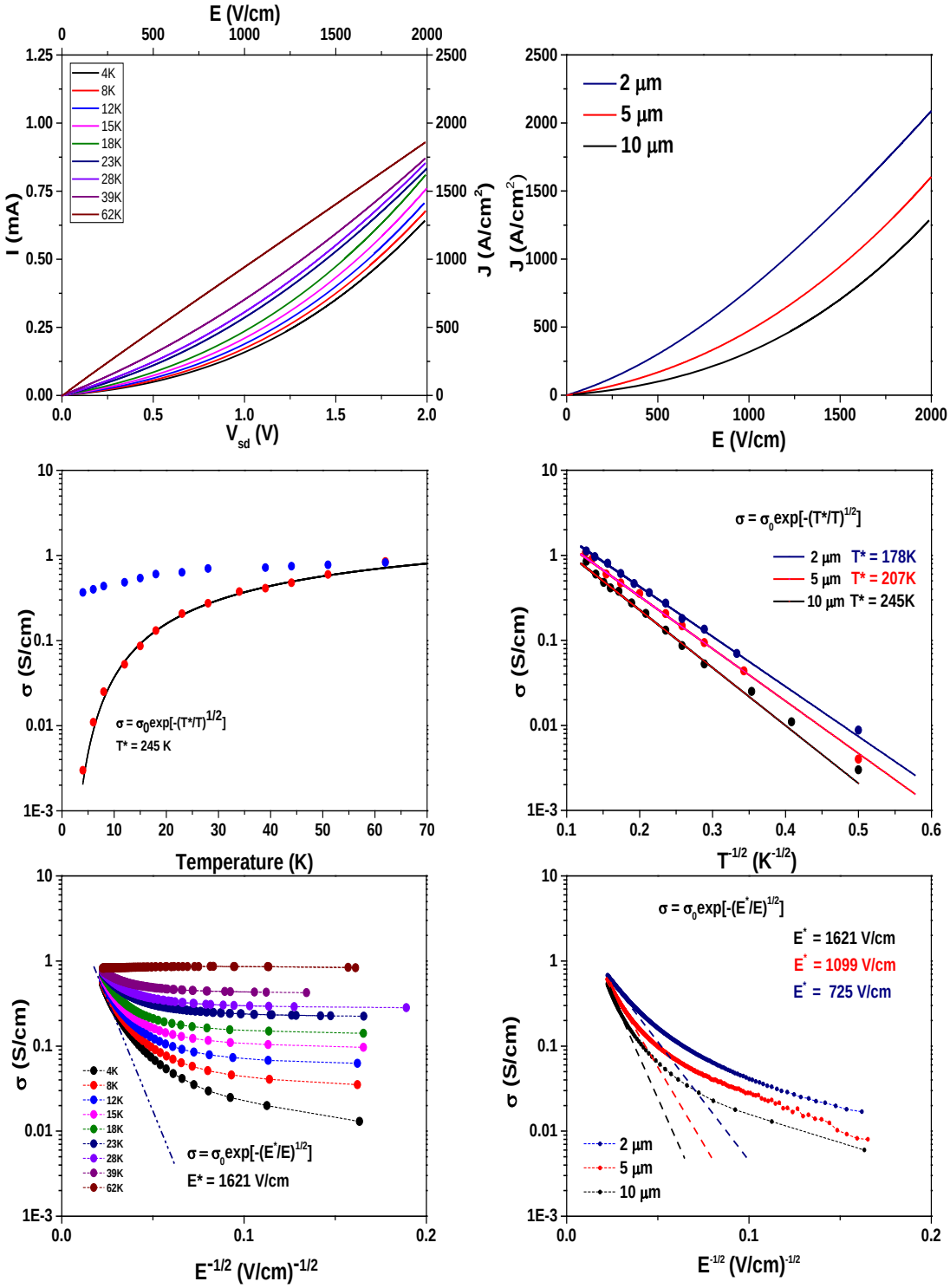

Fig. 3-2 a). Temperature-dependent I-V curve with T ranging from 4 K to 62 K. The I-V curve shows a strong non-linearity below 62 K, showing non-ohmic transport. b). Conductivity of the CQD film versus temperature at different bias. Red: 0.02 V, Blue: 2 V. The black curve is the

fitted data using ES-VRH model. c). Conductivity of HgTe CQDs plotted against inverse root of the electric field. From 4 K to 62 K. d). Current density versus Electric field for HgTe CQD film measured at different gap length. Black: 10 μm, Red: 5 μm, Navy: 2 μm. e). Log of Current density versus inverse root of temperature, with electric field at 25 V/cm. f). Conductivity of HgTe CQDs plotted against inverse root of the electric field for different gap size. The dotted line corresponds to the linear fit towards the high field.

The ES-VRH model also predicts that the conductance asymptotically approaches the relationship $\sigma \propto \exp\left(-\sqrt{E^*/E}\right)$. Therefore, we plotted the inverse root of the electric field and conductance shown in Fig. 3-2c), which shows indeed that the conductance is reaching a limit at high field. The slope of this transition is extrapolated at high electric field with E^* = 1621 V/cm. If electron transport follows the theory correctly, one can directly compare the relative value of T^* and E^*, which are related by $E^* = k_B T^*/2e\xi$. This gives a second way to estimate the electron localization length ξ, which is independent of the choice of β and ε used. ξ is calculated to be 65.1 nm. The close agreement of the two values shows that the choice we made in the previous sections is not far from the actual ones and suggests the delocalization of electrons over a range of 4 to 5 dots.

We also measured the IV curve of films with gap length 5 and 2 μm. To ensure a direct comparison across the three-gap size, we plotted E and J, instead of I and V shown in Fig. 3-2d). Films with all gap length shows a strong non-linearity and is consistent with devices of a smaller gap showing a higher mobility.

Fig. 3-2d) also shows that the non-linearity of the device cannot be limited by any electrode-film Schottky barrier. Since the existence of a barrier would mean that the contact resistance

$R_{contact} \propto \frac{1}{W}$, for the device dominated by the contact resistance, this would imply $\sigma \propto W$. As the W/L ratio is fixed for all devices, we would expect that the device with the 10 μm gap having the highest conductance and thus highest current density under the same applied field. In fact, the opposite is observed, which rules out the non-linearity limited by the contact barrier. Following the same reasoning as before, we also plotted the conductance-temperature dependence at low electric field limit of 20 V/cm in Fig. 3-2e) and conductance-electric field dependence at 4 K in Fig. 3-2f). The extrapolated data are shown in Table 2.

Table 3-2. Parameters extracted from the plots using the ES-VRH theory

Gap Length	E^* *V/cm*	T^* *K*	ξ $(\beta e^2/4\pi\varepsilon\varepsilon_0 k_B T^*)$ *nm*	ξ $(k_B T^*/2eE^*)$ *nm*	Ratio of ξ
10 μm	*1621*	*245*	*56.9*	*65.1*	*1.14*
5 μm	*1099*	*207*	*67.4*	*81.2*	*1.20*
2 μm	*725*	*178*	*78.4*	*105.8*	*1.35*

The ξ calculated shows a consistent trend of increasing localization length as gap length decreases, which is confirming the reasoning behind a higher mobility at smaller gap length. Considering the $\xi = \beta e^2/4\pi\varepsilon\varepsilon_0 k_B T^*$ estimate, as ε should not be dependent on the gap length, this would suggest that β could be larger than 6.1 theorized for 2D transport and closer to 8.7 for 1D transport ($\beta = 13$) as gap length decrease to 2 μm. As regions with the largest localization length would also have the highest conductance, the transport of electrons through the HgTe film over the gap can be seen as through many parallel channels with various conductance depending

on the domain size. Since the majority of electrons flows through the channel with the highest conductivity, the hopping may be closer to a 1D than 2D hopping. This would be the strongest when the gap length is closest to the localization length, and thus a higher β is observed as gap length decrease.

To attempt to visualize the size and length of electrons transport channels inside CQD films, we used a high voltage (10 V) pulse applied across the 2-μm device at 4 K. This should result in the channels of higher conductance to overheat due to the large amount of power flowing through, and to cause the dots to be blasted from the device. What is observed is a gradual stepwise decrease in the conductance, as could be expected if discrete channels get burned out. As shown in the Fig. 3, at the end of a run, there are clearly a few "burned" channels in the device, with the width of such channels on the order of 100 nm.

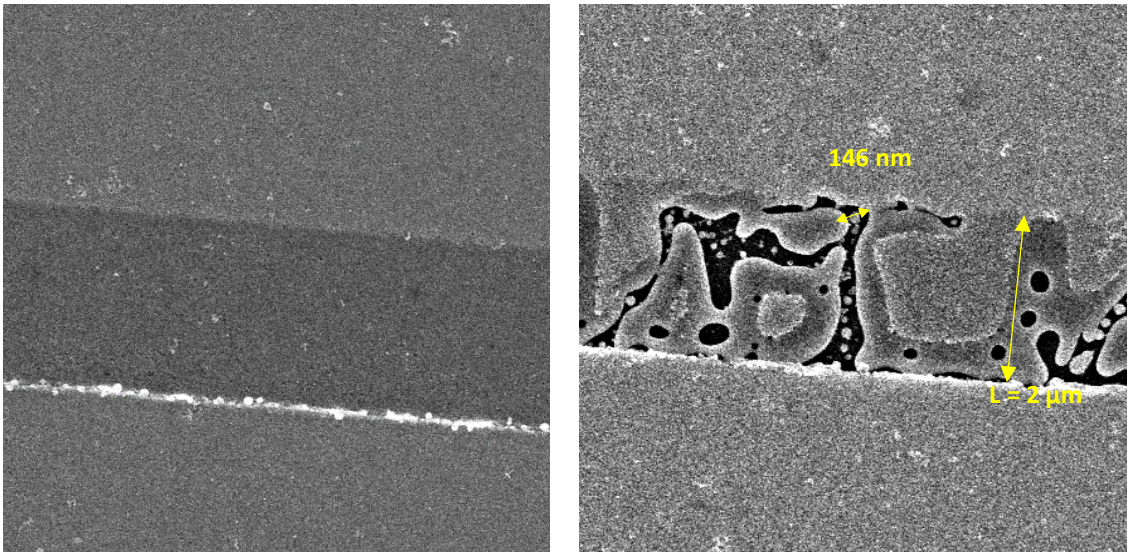

Fig. 3-3. HgTe CQD films drop-casted between Au electrodes with a gap length of 2 μm. Left: Before a 10 V pulse is applied; Right: After the electric pulse blasted the conductive channels of the CQD films.

Yu et al. proposed the variable range hopping conductance converge to nearest neighbor hopping when the external field applied is significantly larger than the critical field.[20] $E_0 = 2k_BT/e\xi$. Using the estimate for ξ described before, we get E_0 > 6000 V/cm. This is larger than the maximum electric field applied in our experiments. Therefore, even at high field in this experiment, we are not yet reaching the nearest-neighbor hopping. However, the convergence of conductance at high fields in Fig. 3-2c). may suggest that we are approaching a constant conductance by nearest-neighbor hopping.

3.6 Joule Heating During Measurement

One could wonder if the temperature set in the cryostat is representative of the temperature of the HgTe CQD film during the measurements and if the observation of non-zero mobility as the sample approach 0 K may be the consequence of an imprecision on the value of said temperature. In the case of a short conductive channel, Joule heating may have a predominant effect due to the increased conductivity of the device. To address this point, COMSOL® simulations were conducted to estimate the heat generation in the device featuring a 2µm long channel.

The simulated system consists of a 1 cm x 1 cm substrate with a 400µm thick silicon layer and a 300nm thick SiO_2 layer. On top of the oxide, the HgTe CQD channel is defined as a 100 µm x 2 µm layer with 100nm thickness. The electrical power P dissipated as heat in the device was calculated using $P=V^2/R$ with values of the resistance R extracted from the experimental I-V curves and V=0.4V the maximum bias applied during voltage sweeps. The influence of the electrodes on heat dissipation is neglected and all the dissipated electrical power is distributed homogeneously over the volume of the HgTe CQD channel. To mimic the situation of a sample in contact with a cryostat, the back surface of the silicon substrate is defined as a thermostat with set temperature. We assumed ideal thermal contact at the interface between the QDs film and the substrate while

the boundaries of the system were defined as perfect thermal insulators. Temperature dependent thermal conductivities were taken from the literature for the Si layer and the SiO2 layer.[31–33] To make sure to not overestimate the capability of our device to evacuate the generated heat, the thermal conductivity of the HgTe CQD layer was assumed to be very low and was arbitrarily set as the thermal conductivity of SiO2 divided by a factor 20, which is roughly one order of magnitude lower than thermal conductivities measured for other types of semiconductor nanocrystal films.[34,35] The average temperature in the film is calculated in the stationary regime and no further investigation has been made to know if thermal equilibrium is reached during the voltage sweeps performed in the experiments.

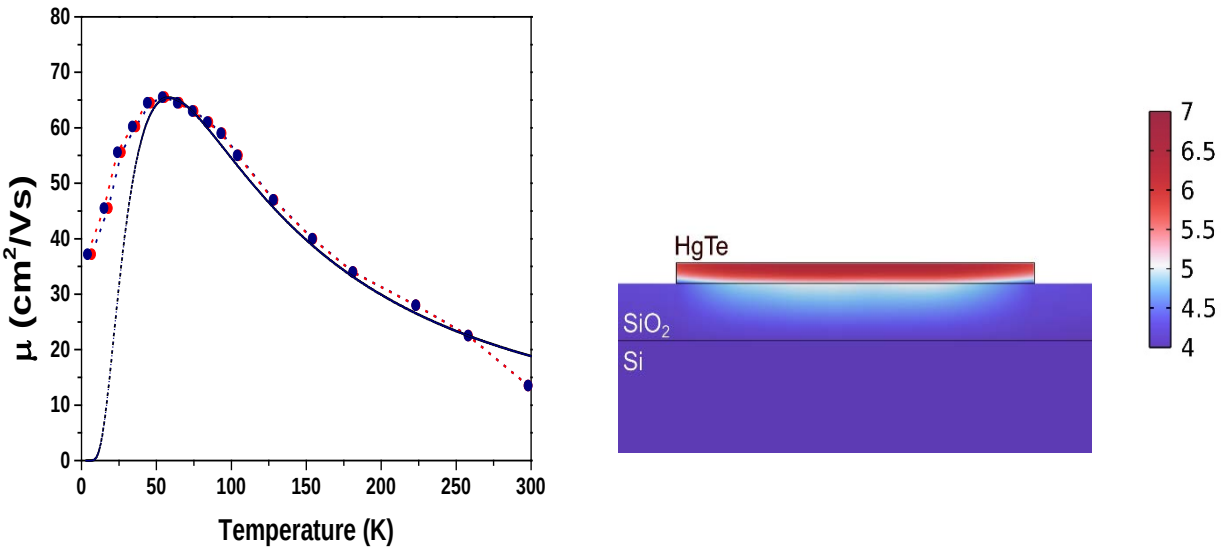

Fig. 3-4 a). Measured differential mobility with the cryostat (Navy) and simulated (Red) temperature after considering Joule Heating. b). Cross section of the device with dissipating thermal power at high biases. The sink is set at the bottom of the Silicon Wafer at T = 4 K.

Fig. 3-4b) shows the calculated temperature across the cross-section of the system for values of the dissipated electrical power and cryostat temperature corresponding to the mobility measurement at 4K. We observe that the calculated temperature in the CQD film is a few kelvins higher than the temperature of the cryostat, illustrating the fact that Joules heating can indeed have a noticeable influence on the temperature of the device. Running the simulation with parameters corresponding to each data points of Fig. 3-1 b), we obtain a new set of adjusted temperatures for the HgTe CQDs. Fig. 3-4 a). presents the mobility measurements performed on the 2µm device with adjusted temperatures obtained from the simulations, along with the experimental data reproduced from Fig. 3-1 b). The largest variations from the experimental curve occurs at low temperature and are limited to a few Kelvins, which slightly alters the shape of the curve but does not mitigate the results of the experiments as one can still observe non-zero mobility as the temperature approach 0 K. Additional simulations were also made adding a thick SiO_2 layer on the back of the substrate resulting in an increase of the temperature by only one thousandth of a kelvin.

PART II

3.7 Introduction

In the experiments presented previously, I used FET to measure the carrier mobility in HgTe CQD films with small size distribution. Increased mobility in theory improves the performance of HgTe CQD devices by improving carrier extraction efficiency. It also improves detectivity if the noise does not increase more than the responsivity. This naturally led to determining the relationship between the device conductance and noise in the device.

In most electronic devices, 1/f noise is a major noise source, and it has been extensively studied. Though 1/f is undesirable for device applications, it is also a useful tool to explore the mechanism of carrier transport in these materials. 1/f noise can be attributed to many independent fluctuations inside the material, each with a single exponential decay time, but with an exponential distribution of time constants. Two models, McWhorter and Hooge, have been proposed to explain the origin of the 1/f noise.[36–38] Since the current fluctuations can be expressed as $\Delta I = e\mu\Delta n + en\Delta\mu$, the fluctuations in carrier number Δn, is described by the McWhorter Model. This is also the dominant source of noise in CMOS transistors, where charge carriers have a fixed mobility, but traps exist inside the channel of conductance. As these carriers flow through the channel they enter and exit these traps creating fluctuations in carrier number. On the other hand, the fluctuations in mobility $\Delta\mu$ is described by the Hooge model, which is attributed to the scattering of these carriers between phonons or impurities. Previous research on other CQD systems assigned the 1/f noise to mobility fluctuation. Another work on CQD FET assigned the 1/f noise to trap states on the oxide layer of the FET, however this effect exist only when the contact with the film is not optimized.[39]

In following chapter, I will discuss the relationship of conductance and the measured 1/f noise

inside the HgTe CQD conductors, following the film preparation directly following method discussed in Chapter 3.

3.8 Noise and Conductance Measurement

One interesting question is the effect of the higher conductance on the noise of this device. Reports on the noise of both HgTe treated with EdT ligand exchange and the hybrid ligand exchange shows the noise spectrum dominated by the 1/f noise below 10 kHz. Therefore, it would be useful to investigate the effect of temperature, electric field, and channel length on the noise spectrum of these high mobility CQDs. To measure the noise level and the relationship to transport inside the CQD films, we applied a range of biases and measured the noise spectrum using an SR760 spectrum analyzer.

Starting with the device with a gap length of 10 μm, where the noise of the device is measured at 4 K with bias ranging from 0.04 V to 2 V, Fig 3-5a). shows the noise measured at 500 Hz plotted against the applied bias. The shot noise limit and the Johnson noise limit are also plotted as a comparison. It can be seen that the noise level is close to the shot noise and an order of magnitude above the Johnson noise. Hooge proposed an empirical formula where $S_I/I^2 = A/f$, where I is the (dark) current and $S_I = i_n^2$, is the frequency dependent noise spectral density.[40,41] Interestingly, the devices are all dominated by the 1/f noise as shown in Fig. 4b) for all biases and frequencies up to 10 kHz. We do observe that noise spectrum tends to flatten out at low biases and high frequencies, however it is likely due to the limitation of the instrumentation given the measured current is low.

At 4 K, we observe that the measured noise is significantly above the shot noise at high bias. However, as shown in Fig. 3-5b, at low enough bias, the noise always goes below the shot noise at high frequencies.

The noise is also measured at two other temperatures, 80 K and 298 K. At 298K, the 1/f noise at 500 Hz is always an order of magnitude above the shot noise. The S_I/I^2 measurements are shown in Fig. 3-5c)., where we plotted the noise at 500 Hz versus the bias applied. A clear slope of -1 can be extrapolated at temperatures 80 K and 298 K, which means the S_I/I^2 scales as V^{-1}. This would be the same scaling for the shot noise, and therefore, the noise at 298K in the device scales like the shot noise with respect to bias but is orders of magnitude larger. Previous studies have shown the same noise dependence of the bias for CdSe/CdS, which signifies increased I/i_n at higher bias. The noise is lowered at higher bias.[42]

The noise at 4 K shows an exponent with bias of -1 at lower biases and -1.5 at higher biases. This implies that the fluctuations in mobility at lower field is similar to those at high temperatures, but at high field, this is further suppressed by the applied electric field. This could be cause by the applied field between dots becomes larger to k_BT at this bias. Since $k_BT = 34\ \mu eV$ at 4 K, with a dot-to-dot distance around 15 nm, this would imply the applied field between dots would exceed k_BT when $V_{Bias} > 0.25\ V$, This is indeed approximately where the transition between the two slopes took place.

In addition, we also measured the noise power density S_I and its dependence on the dark current. As shown in Fig. 3-5d, in the limit where the noise scales similarly to the shot noise with bias, we expect $S_I \propto I$. This is what is observed for this device at high temperatures. The deviation arises again at 4 K, where $S_I \propto I^{1.25}$ at high bias applied. This indicates that the noise power density is greater than the shot noise, however, it is observed that in general the slope decreases as the dark current increase, indicating a return to conventional behavior.

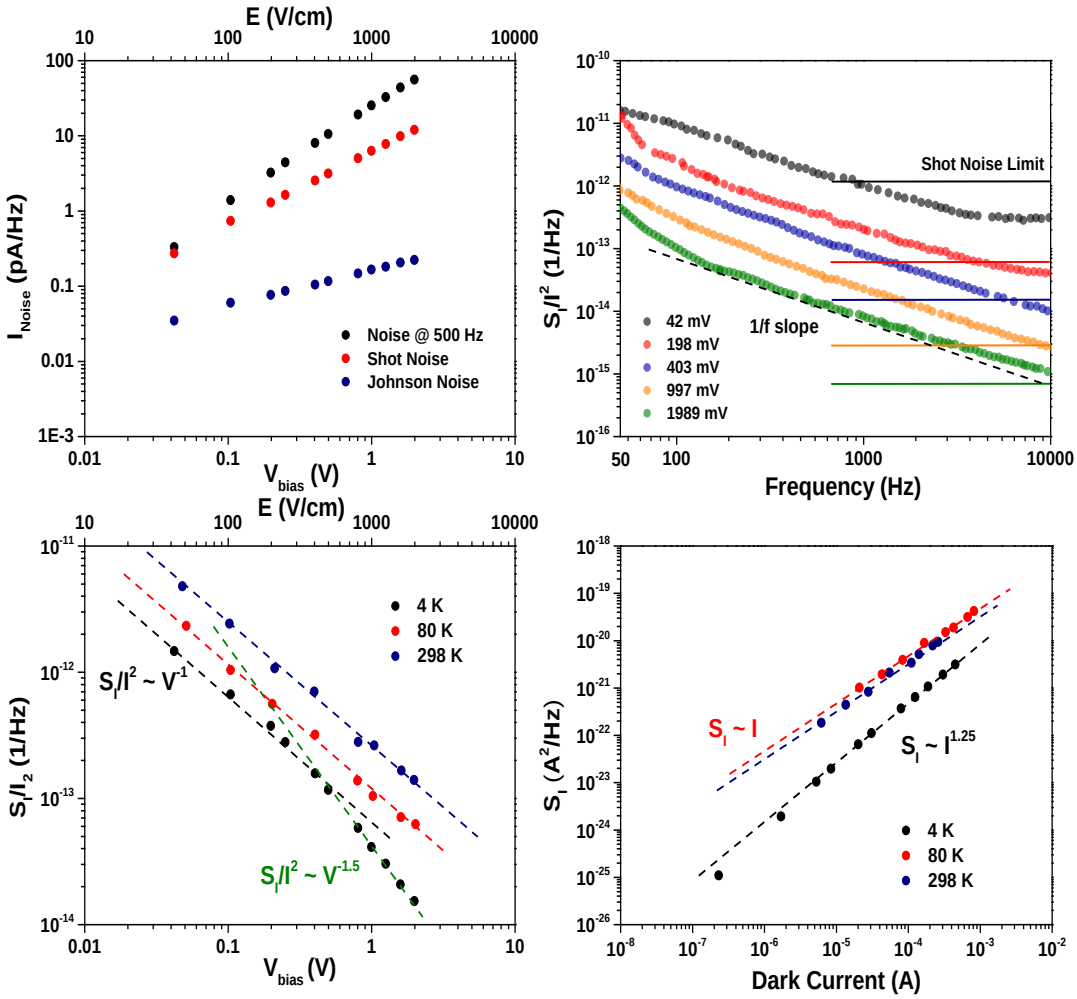

Fig. 3-5 a). Measured Noise current at 500 Hz versus electric field applied for HgTe CQD film with 10 μm gap size. (Black) The Shot Noise limit (Red) and Johnson Noise limit (Navy) are also shown in the figure. b). 1/f noise of HgTe CQD film at five different biases applied, from 50 Hz to 10kHz. c). The Noise power density at 500 Hz versus the voltage bias applied. Dash line represents the best fit with $\beta = -1$, or -1.5. Temperature ranges from 4 K (Black), 80 K (Red) to 298 K (Navy). d). The Noise spectral density at 500 Hz versus the Dark Current. Dash line represents the best fit with $\gamma = 1$, or 1.25. Temperature ranges from 4 K (Black), 80 K (Red) to 298 K (Navy).

3.10 Noise and its dependency on the Channel Length

The study naturally leads to the study on the dependency of the noise on the channel length. Lai et al. reported, in the study of CdSe CQDs on an FET, that, depending on the source of the 1/f noise, the S_I/I^2 can be proportional or inversely proportional to the channel length L.[39] The author uses FET devices made with L ranging from 30 μm to 200 μm, with a fixed W/L ratio of 15, the author also used a fixed source-drain bias of 50 V.

The devices used in this experiment are with channel length L of 2 μm, 5 μm, and 10 μm. This implied that, with the same applied source drain bias, the effective field on the quantum dots ranges over a factor of 5. Therefore, it is more natural to compare the noise power density of devices under the same applied field. Thus, in this study, we applied a range of biases that scales with the channel length. When comparing the 1/f noise between devices, the applied electric field is held at a constant with sample variation less than 5%,

Fig. 3-6a and Fig. 3-6b shows the noise power density divided by the square of dark current S_I/I^2, with frequencies ranging from 50 Hz to 10 kHz, at an applied electric field of 200 V/cm and 2000 V/cm respectively. It can be seen in that, in both cases, the device is dominated by the 1/f noise. We describe $E = 200\,\mathrm{V/cm}$ as low field, as k_BT at 4 K is equivalent to a field strength of $250\,\mathrm{V/cm}$ between neighboring quantum dots. i.e., $eEd < k_BT$. Conversely, $E = 2000\,\mathrm{V/cm}$ is 8 times higher than the k_BT limit, which is described as high field.

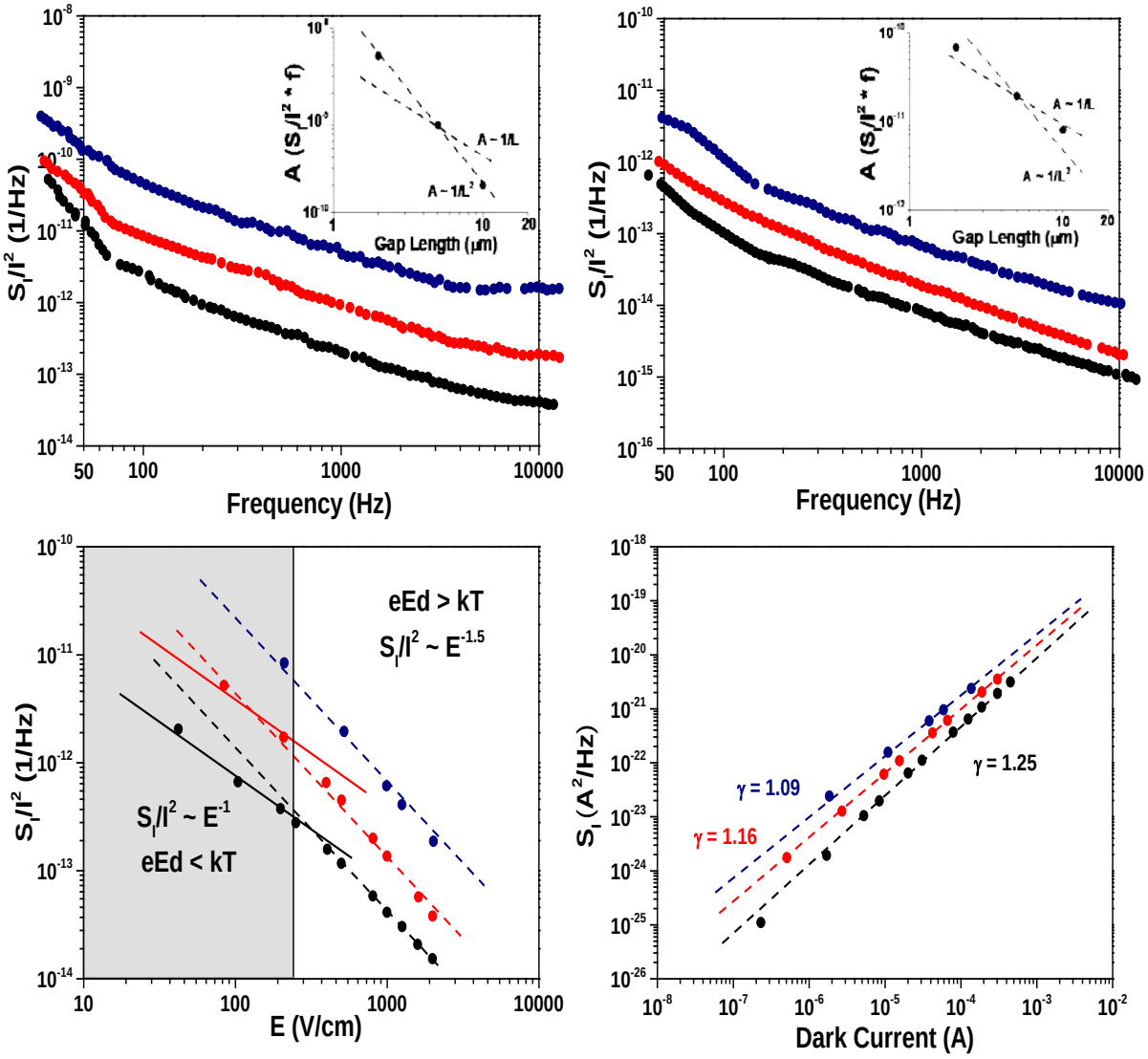

Fig. 3-6 a). 1/f noise of HgTe CQD film at five different biases applied, from 50 Hz to 10kHz normalized to E ~ 200 V/cm. With gap size of 10 μm (Black), 5 μm (Red) and 2 μm (Navy). b). 1/f noise of HgTe CQD film at five different biases applied, from 50 Hz to 10kHz normalized to E ~ 2000 V/cm. With gap size of 10 μm (Black), 5 μm (Red) and 2 μm (Navy). c). The Noise power density at 500 Hz versus the applied Electric Field at 4 K. Dash line represents the best fit with β = -1.5. With gap size of 10 μm (Black), 5 μm (Red) and 2 μm (Navy). d). The Noise spectral density at 500 Hz versus the Dark Current. Dash line represents the best fits. Temperature ranges from 4 K (Black), 80 K (Red) to 298 K (Navy).

For homogeneous semiconductors, the noise can be expressed as $\frac{S_I}{I^2} = \frac{A}{f}$, where the constant A captures the scaling of the noise with the design of the conductor.[41] As shown in Fig. 3-6a, in the limit of low electric field applied, S_I/I^2decreases as the channel length L increase. The inset of Fig. 5a), shows the scaling of the constant $A \propto \frac{1}{L^2}$. Since the device have a fixed W/L ratio, the $\frac{1}{L^2}$ is proportional to the inverse of the device area and thus the number of CQDs inside the conductance channel. Therefore, this is consistent with the 1/f noise coming from the fluctuations mediated by the quantum dots, as increasing the number of CQDs averages the variation in carrier number/mobility, and thus reduce the 1/f noise from the device.

Shown in Fig. 5b, the scaling of S_I/I^2 as channel length L increase is different in the limit of high field applied, the constant A shown **in the inset of** Fig. 3-6b), shows a clear deviation from the $A \propto \frac{1}{L^2}$ scaling and closer to $A \propto \frac{1}{L}$. This suggests that 1/f noise in the device no longer comes from the dot alone but may have contributions from the dot-electrode contact. Since the contact only scales with the width of the channel, we expect $S_{Contact} \propto \frac{1}{W} \propto \frac{1}{L}$, consistent with the scaling we see when the applied field is high.

The scaling of S_I/I^2 with the channel length is shown in Table 3-3. If the noise is limited by the channel noise, $A \propto \frac{1}{L^2}$, we expect the ratio of L = 5 μm/L = 10 μm and L = 2 μm/L = 10 μm to be 4 and 25 correspondingly. Else, if the noise is limited to the noise of the contact, $A \propto \frac{1}{L}$, thus the ratio would be 2 and 5. The scaling in Table 3-3 shows the dependency of this ratio with the field applied. A higher applied field would decrease the ratio from $A \propto \frac{1}{L^2}$ to $A \propto \frac{1}{L}$ clearly in one direction. It would imply that the channel noise of the device is suppressed as field applied increase, where the device would be more limited by the change in mobility at the contact surface. A similar trend discussed before can be seen in Fig. 5c, where S_I/I^2 is plotted with the applied

electric field with the three devices. We separate the discussion of the device noise according to the electric field strength relative to k_BT, as $eEd < k_BT$, or $eEd > k_BT$. In all three devices we have seen a different behavior in the two regions, as $\frac{S_I}{I^2} \propto E^{-1.5}$ when $eEd > k_BT$, and $\frac{S_I}{I^2} \propto E^{-1}$ when $eEd < k_BT$. The crossover of the 1/f noise in the two regions signifies that the contribution of noise at the two regimes

Fig. 3-6d). shows the trend of the noise power density S_I with the different dark current applied. S_I shows different dependency $S_I \propto I^{\gamma}$, where γ = 1.25, 1.16 and 1.09 respectively. Thus, S_I always scales larger than the dark current.

Table 3-3. S_I/I^2 for different gap size normalized to the same electric field. The ratio of S_I/I^2 for different gap size are also shown.

E (V/cm)	L = 10 μm S_I/I^2 (1/Hz)	L = 5 μm S_I/I^2 (1/Hz)	L = 2 μm S_I/I^2 (1/Hz)	Ratio (L = 5/L = 10)	Ratio (L = 2/L = 10)
200±10	3.76E-13	1.73E-12	8.42E-12	4.59	22.39
400±4	1.58E-13	6.56E-13	--	4.15	--
500±10	1.17E-13	4.50E-13	1.95E-12	3.85	16.69
800±6	5.84E-14	2.00E-13	--	3.43	--
1000±10	4.12E-14	1.37E-13	6.12E-13	3.33	14.85
1250±5	3.04E-14	--	4.09E-13	--	13.46
1600±12	2.08E-14	5.72E-14	--	2.75	--
2000±15	1.54E-14	3.82E-14	1.87E-13	2.48	12.18

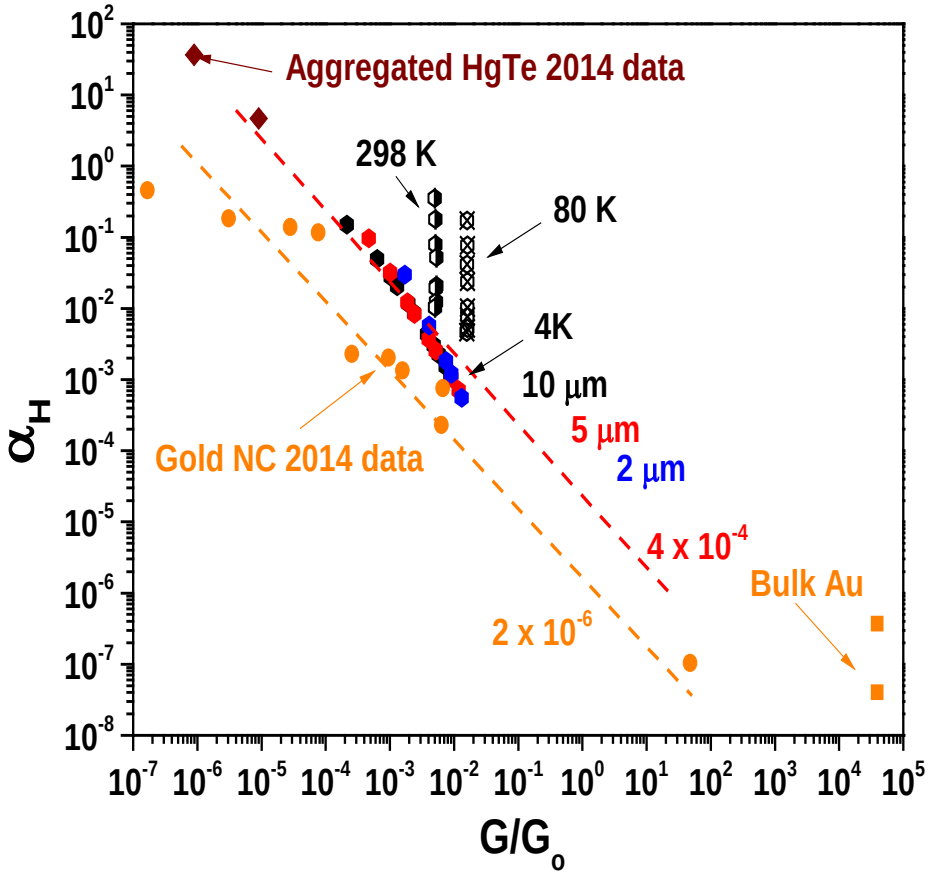

Fig. 3-7. Plot of the Hooge constant α_H versus the interdot conductance G/G_o. The measurement of the device at 4 K are shown as black (10 μm), red (5 μm) and blue (2 μm) hexagons. Measurement of the 10 μm device at 80 K are shown as crossed black hexagon and ones at 298 K are shown as half-filled black hexagon. Data from the 2014 HgTe data are shown as brown-colored dots. Gold Nanoparticles are shown as gold-colored circles. Bulk Au measurement are shown as gold-colored squares. Two dashed lines with gradient of -1 are added to the figure to guide the trend, the intercept of the two lines is 4×10^{-4} (red) and 2×10^{-6} (gold).

Lastly, to compare the 1/f noise level of our HgTe with other nanocrystal systems, we used an

effective nanocrystal Hooge constant defined such that $\alpha_H = \frac{S_I}{I^2} N_{nc} f$, where N_{nc} is the number of nanocrystals in the conductor, and f is the frequency during the measurement. α_H is the Hooge unitless constant independent of the device structure and size of the dots. We also calculated the interdot conductance $G_{NC} = \sigma d$, where d is the dot-to-dot distance. G_{NC} is normalized to $G_0 = 2e^2/h$, the quantum conductance, such that G_{NC}/G_0 is also unitless. The plot of α_H versus G_{NC}/G_0 is shown in Fig. 3-7). The previous literature data from Au NCS and Bulk Au is also shown for comparison.[42]

We note that, the measurements at 80 K and 298 K show that the HgTe CQD film have an order of magnitude more noise when compared to the Au nanoparticles of similar conductance, while they are in a similar trend as other HgTe CQDs shown in Fig. 3-7. As the conductance is ohmic at high temperatures, the data points are nearly purely vertical and do not follow the previous published trend. However, the transport of electrons at 4 K shows a large variation over two orders of magnitude depending on the bias applied during measurement. Interestingly, the overall trend fits on to a single line with gradient of -1 at lower electric field applied. This indicates that the higher interdot conductance suppress the 1/f noise inside the film, consistent to other nanoparticles. From the trend line, we can extrapolate a constant such $\alpha_H G/G_o = 4 \times 10^{-4}$. This is two orders of magnitude compared to the measurement from gold nanoparticles $\alpha_H G/G_o = 2 \times 10^{-6}$, which indicates further room for improvement in noise. At high biases, the Hooge constant α_H at the smallest gap length is comparable to Au nanoparticles.

It is interesting to note that the transport of electrons at 4 K and 80 K at high biases have drastically different noise level, even though both have similar conductivity. This would mean that the field driven nearest-neighbor hopping at 4 K have much lower noise compared to the activated hopping at 80 K. The reasoning behind this may be explored further by from perspective of electron transfer

theories.

3.11 Noise and its dependency on the film quality

As previously reported, one important contribution to the 1/f noise is the film quality, and only "good film" should be studied.[42] Depending on the number of defects and cracks in the CQD film, we also observe that the 1/f noise can be 100 to 1000 times larger. The different films are shown in Fig. 3-8a-c, where we tested the 1/f noise over film with 3 different conditions, a 'good' film which is used for all measurements previously discussed, and two 'poor' films where defects are seen either in the film or at the edge around the contact. Fig. 3-8d shows the $\boldsymbol{S_I/I^2}$ of the device against various biases applied.

Both devices with defects in the film show a significantly increased noise levels compared to 'good' films. This is especially the case when higher biases are applied. The trend of $\boldsymbol{S_I/I^2}$ scaling as $\boldsymbol{V^{-\beta}}$ where $\boldsymbol{\beta} > 1$ breaks down, where typically the $\boldsymbol{S_I/I^2}$ becomes a constant in the case of holes inside the film or start to increase again in the case where cracks exist on the edge of the electrodes. Therefore, one keeps in mind the possibility that much of the discussion of the 1/f noise above may reflect only the best film quality obtained, and that this may not be a rigorous lower limit of the 1/f noise.

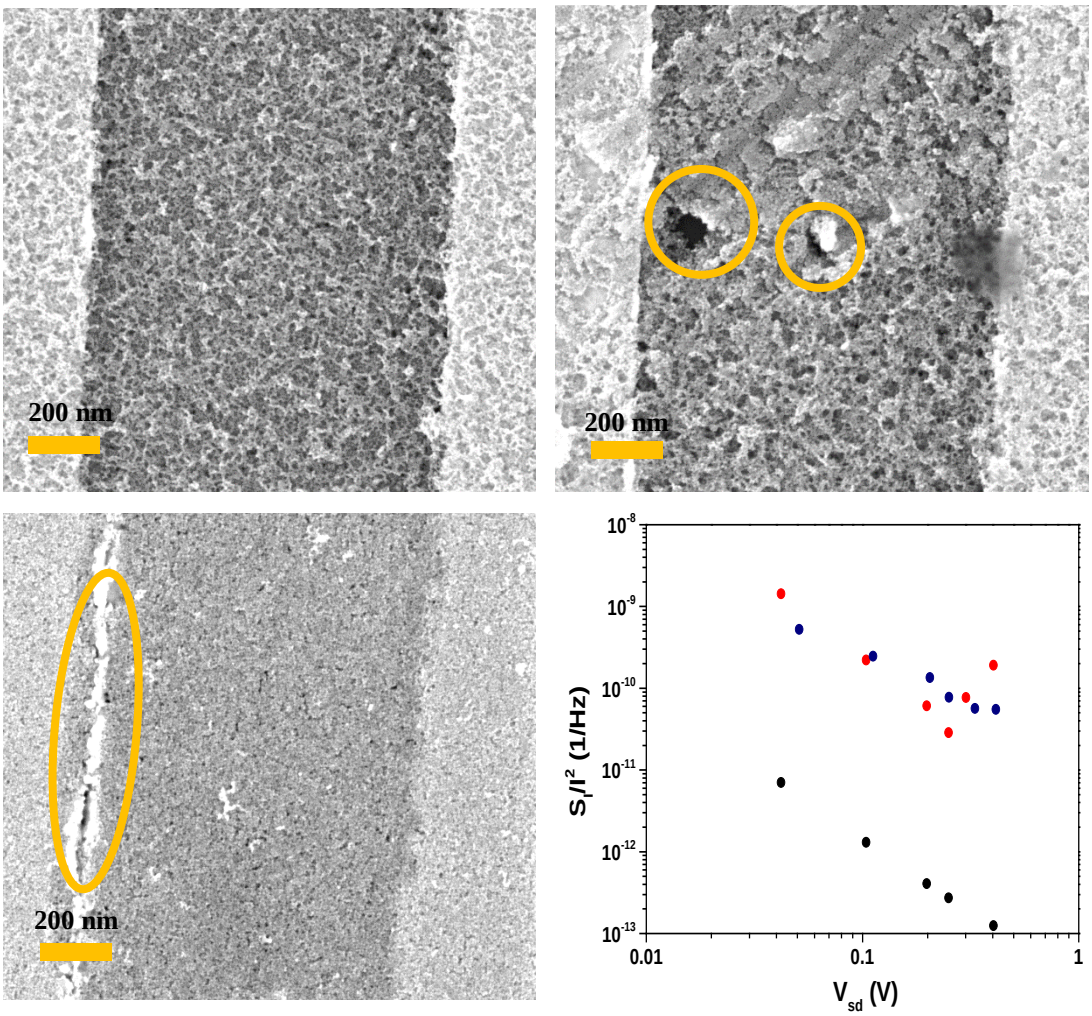

Fig. 3-8. HgTe CQD films drop-casted between Au electrodes with a gap length of 2 μm. a): Drop-casted film with no cracks. b): Drop-casted film with defects in the film. c): Drop-casted film with cracks on one side of the Au electrode. d). S_I/I^2 measured against biased applied across the three different devices. Black: The 'good' device used in all measurement discussed in this chapter. Blue: 'poor' devices with holes inside the film. Red: 'poor' devices with cracks on one side of the electrodes.

3.12 Methods

Materials. $HgCl_2$ (≥98%), $HgBr_2$ (97%), 1,2-ethanedithiol (≥98.0% (GC)), HCl (ACS reagent, 37%), 2-Mercaptoethanol (≥99.0%), butylamine (99.5%), isopropanol (≥99.7%, FG), and anhydrous solvents (octane, toluene, chlorobenzene, and methanol) were purchased from Sigma Aldrich and used as received. Anhydrous N,N-Dimethylformamide (DMF, 99.8%) and HgCl2 (98+%) were purchased from Alfa Aesar and used as received. Oleylamine was purified following our reported procedures. Bis(trimethylsilyl)telluride (98%) was purchased from Acros and stored inside the freezer in a nitrogen glovebox. N-type Si wafers (Res. ≤0.005 ohm.cm) with 300-nm-thick thermal oxide were purchased from WaferPro.

HgTe Synthesis. The synthesis of HgTe CQDs is modified upon a previously reported method. A solution of 36 mg $HgCl_2$ (0.133 mmol), 21 mg $Hg(OAc)_2$ (0.067 mmol) and 4 mL oleylamine (OAm) is heated to 90^{o}C temperature inside a nitrogen glovebox until all Hg compounds have dissolved. The solution is then rapidly heated up to the desired temperature for nanocrystal growth (110 °C, with larger nanocrystals obtained at higher temperature). Meanwhile, a solution of 10 μL of bis-(trimethylsilyl) telluride (TMS_2Te, 0.035 mmol) in 500 μL of anhydrous toluene. The toluene must be fully transparent after adding the TMS_2Te to ensure no small nuclei of Te is formed. This TMS_2Te solution is rapidly injected into the Hg compound solution and heated at the injection temperature for exactly 1 min. Another solution of 65 μL of TOPTe is dissolved in 500 μL of oleylamine preheated to 100^{o}C. After the 1 min reaction of TMS_2Te, this TOPTe solution is also injected into the reaction mixture dropwise slowly over 5 minutes. The solution is immediately quenched with 4 ml of cold Toluene.

The QDs are redispersed in Toluene, and subsequently precipitated again with isopropanol and centrifugation. The resulting QDs are dispersed in Octane before ligand transfer. For the high-

mobility HgTe QDs, the oleylamine capped in Octane are mixed with 5 mL of DMF with 0.025 mM HgCl2, 140 μL of 2-mercaptoethanol, and 400 μL of butylamine in a glovebox. Shaking resulted in the transfer of HgTe QDs from Octane to DMF phase. The solution of dots is cleaned twice with Octane. The solution is then precipitated with antisolvent toluene and centrifugation at 4000 rpm for 1 min, the final precipitate is redispersed in a small amount of DMSO.

Device Fabrication. The FET is made with three pairs of evaporated gold electrodes with width/gap-length pair of 10 μm/500 μm; 5 μm/250 μm; 2 μm/100 μm. The underlying substrate is made with doped Si wafer with 300 nm of thermally grown SiO_2. The device is first heated to 70^{o}C and treated with 1% HCl/H_2O. The hybrid ligand exchange HgTe CQD is dropcasted onto the FET and quickly dried by removing excess solvent from the surface using Kimwipe. After the dropcasted HgTe film is dried on the hotplate for 1 hour under nitrogen, a layer of polyvinyl butyrol is spincoated on the surface of the FET, and device is further dried under nitrogen overnight. The device is then used for measurement.

Mobility Measurement. The differential mobility of the HgTe film is measured using the slope of the FET transport curves. The maximum biases applied in the device is around 2 V, the gate voltage we applied is between -15 V to 15 V. As the FET is in the linear regime, the formula for the mobility is given as, $\mu = \frac{\partial I_{ds}/\partial V_g}{V_{ds}} \frac{L}{WC_i}$ where I_{ds} is the drain−source current, V_g is the gate potential, V_{ds} is the source-drain bias voltage, C_i is the capacitance of the 300 nm SiO_2 gate dielectric, L is the channel length, and W is the channel width.

Optical Absorption. Infrared spectra were collected with a Thermo Nexus 670 FTIR in transmission mode with the film prepared on a ZnSe prism and the absorption measured in total internal reflection.

Transmission Electron Microscopy (TEM). TEM images were obtained on a FEI Tecnai Spirit

or F30 microscopes at 300 kV.

Size Distribution Measurement. CQD sizes are analyzed manually from the TEM images, and the size histogram is fitted with a gaussian function. The volume is calculated using the mean radius/apex to base distance as the diameter of a perfect sphere.

3.13 Appendix

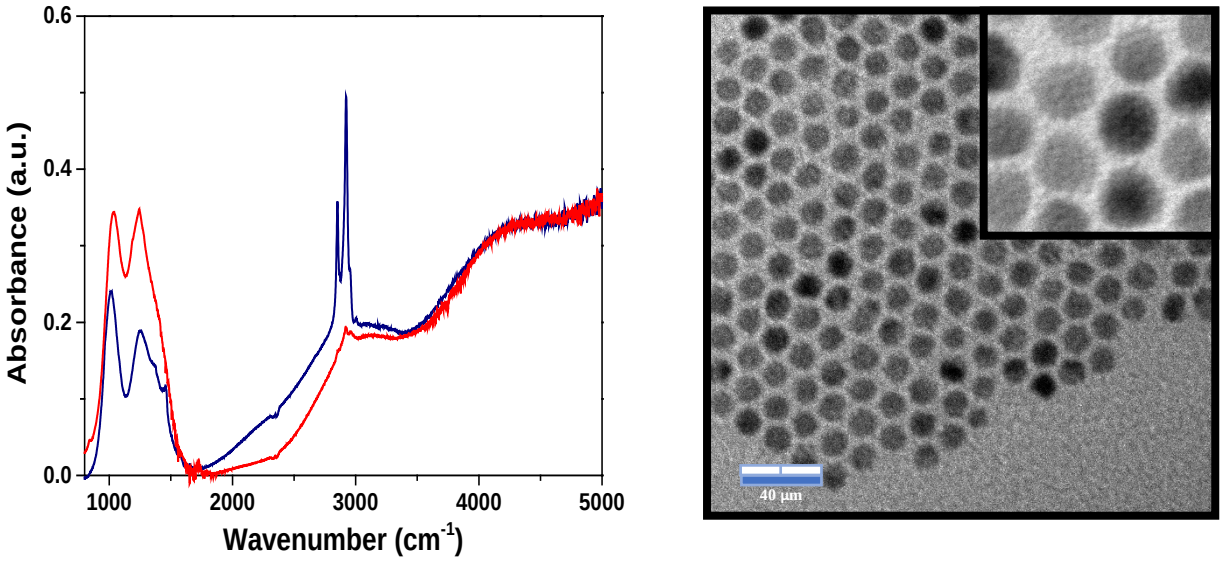

Fig. 3-9. a). Absorption Spectrum of the HgTe CQD film, after cleaning 2 times with oleylamine ligands (Red) and after hybrid-ligand transfer (Blue) b): FET image of the HgTe CQDs synthesized as discussed in Section 3.12.

References:

(1) Kovalenko, M. V.; Scheele, M.; Talapin, D. V. Colloidal Nanocrystals with Molecular Metal Chalcogenide Surface Ligands. *Science* **2009**, *324* (5933), 1417–1420. https://doi.org/10.1126/science.1170524.

(2) García de Arquer, F. P.; Talapin, D. V.; Klimov, V. I.; Arakawa, Y.; Bayer, M.; Sargent, E. H. Semiconductor Quantum Dots: Technological Progress and Future Challenges. *Science* **2021**, *373* (6555), eaaz8541. https://doi.org/10.1126/science.aaz8541.

(3) Kagan, C. R.; Murray, C. B. Charge Transport in Strongly Coupled Quantum Dot Solids. *Nat. Nanotechnol.* **2015**, *10* (12), 1013–1026. https://doi.org/10.1038/nnano.2015.247.

(4) Choi, J.-H.; Fafarman, A. T.; Oh, S. J.; Ko, D.-K.; Kim, D. K.; Diroll, B. T.; Muramoto, S.; Gillen, J. G.; Murray, C. B.; Kagan, C. R. Bandlike Transport in Strongly Coupled and Doped Quantum Dot Solids: A Route to High-Performance Thin-Film Electronics. *Nano Lett.* **2012**, *12* (5), 2631–2638. https://doi.org/10.1021/nl301104z.

(5) Chen, T.; Reich, K. V.; Kramer, N. J.; Fu, H.; Kortshagen, U. R.; Shklovskii, B. I. Metal–Insulator Transition in Films of Doped Semiconductor Nanocrystals. *Nat. Mater.* **2016**, *15* (3), 299–303. https://doi.org/10.1038/nmat4486.

(6) Balazs, D. M.; Matysiak, B. M.; Momand, J.; Shulga, A. G.; Ibáñez, M.; Kovalenko, M. V.; Kooi, B. J.; Loi, M. A. Electron Mobility of 24 Cm2 V−1 S−1 in PbSe Colloidal-Quantum-Dot Superlattices. *Adv. Mater.* **2018**, *30* (38), 1802265. https://doi.org/10.1002/adma.201802265.

(7) Lee, J.-S.; Kovalenko, M. V.; Huang, J.; Chung, D. S.; Talapin, D. V. Band-like Transport, High Electron Mobility and High Photoconductivity in All-Inorganic Nanocrystal Arrays. *Nat. Nanotechnol.* **2011**, *6* (6), 348–352. https://doi.org/10.1038/nnano.2011.46.

(8) Greenberg, B. L.; Robinson, Z. L.; Reich, K. V.; Gorynski, C.; Voigt, B. N.; Francis, L. F.; Shklovskii, B. I.; Aydil, E. S.; Kortshagen, U. R. ZnO Nanocrystal Networks Near the Insulator–Metal Transition: Tuning Contact Radius and Electron Density with Intense Pulsed Light. *Nano Lett.* **2017**, *17* (8), 4634–4642. https://doi.org/10.1021/acs.nanolett.7b01078.

(9) Roest, A. L.; Kelly, J. J.; Vanmaekelbergh, D.; Meulenkamp, E. A. Staircase in the Electron Mobility of a ZnO Quantum Dot Assembly Due to Shell Filling. *Phys. Rev. Lett.* **2002**, *89* (3), 036801. https://doi.org/10.1103/PhysRevLett.89.036801.

(10) Lan, X.; Chen, M.; Hudson, M. H.; Kamysbayev, V.; Wang, Y.; Guyot-Sionnest, P.; Talapin, D. V. Quantum Dot Solids Showing State-Resolved Band-like Transport. *Nat. Mater.* **2020**, *19* (3), 323–329. https://doi.org/10.1038/s41563-019-0582-2.

(11) Chen, M.; Lan, X.; Tang, X.; Wang, Y.; Hudson, M. H.; Talapin, D. V.; Guyot-Sionnest, P. High Carrier Mobility in HgTe Quantum Dot Solids Improves Mid-IR Photodetectors. *ACS Photonics* **2019**, *6* (9), 2358–2365. https://doi.org/10.1021/acsphotonics.9b01050.

(12) Chen, M.; Guyot-Sionnest, P. Reversible Electrochemistry of Mercury Chalcogenide Colloidal Quantum Dot Films. *ACS Nano* **2017**, *11* (4), 4165–4173. https://doi.org/10.1021/acsnano.7b01014.

(13) Guyot-Sionnest, P. Electrical Transport in Colloidal Quantum Dot Films. *J. Phys. Chem. Lett.* **2012**, *3* (9), 1169–1175. https://doi.org/10.1021/jz300048y.

(14) Collier, C. P.; Saykally, R. J.; Shiang, J. J.; Henrichs, S. E.; Heath, J. R. Reversible Tuning of Silver Quantum Dot Monolayers Through the Metal-Insulator Transition. *Science* **1997**, *277* (5334), 1978–1981. https://doi.org/10.1126/science.277.5334.1978.

(15) Zabet-Khosousi, A.; Dhirani, A.-A. Charge Transport in Nanoparticle Assemblies. *Chem. Rev.* **2008**, *108* (10), 4072–4124. https://doi.org/10.1021/cr0680134.

(16) Zabet-Khosousi, A.; Trudeau, P.-E.; Suganuma, Y.; Dhirani, A.-A.; Statt, B. Metal to Insulator Transition in Films of Molecularly Linked Gold Nanoparticles. *Phys. Rev. Lett.* **2006**, *96* (15), 156403. https://doi.org/10.1103/PhysRevLett.96.156403.

(17) Leatherdale, C. A.; Kagan, C. R.; Morgan, N. Y.; Empedocles, S. A.; Kastner, M. A.; Bawendi, M. G. Photoconductivity in CdSe Quantum Dot Solids. *Phys. Rev. B* **2000**, *62* (4), 2669–2680. https://doi.org/10.1103/PhysRevB.62.2669.

(18) Guyot-Sionnest, P.; Wang, C. Fast Voltammetric and Electrochromic Response of Semiconductor Nanocrystal Thin Films. *J. Phys. Chem. B* **2003**, *107* (30), 7355–7359. https://doi.org/10.1021/jp0275084.

(19) Yu, D.; Wang, C.; Guyot-Sionnest, P. N-Type Conducting CdSe Nanocrystal Solids. *Science* **2003**, *300* (5623), 1277–1280. https://doi.org/10.1126/science.1084424.

(20) Yu, D.; Wang, C.; Wehrenberg, B. L.; Guyot-Sionnest, P. Variable Range Hopping Conduction in Semiconductor Nanocrystal Solids. *Phys. Rev. Lett.* **2004**, *92* (21), 216802. https://doi.org/10.1103/PhysRevLett.92.216802.

(21) Chen, M.; Shen, G.; Guyot-Sionnest, P. State-Resolved Mobility of 1 Cm2/(Vs) with HgSe Quantum Dot Films. *J. Phys. Chem. Lett.* **2020**, *11* (6), 2303–2307. https://doi.org/10.1021/acs.jpclett.0c00587.

(22) Law, M.; Luther, J. M.; Song, Q.; Hughes, B. K.; Perkins, C. L.; Nozik, A. J. Structural, Optical, and Electrical Properties of PbSe Nanocrystal Solids Treated Thermally or with Simple Amines. *J. Am. Chem. Soc.* **2008**, *130* (18), 5974–5985. https://doi.org/10.1021/ja800040c.

(23) Simon, S. H. *The Oxford Solid State Basics*; Oxford University Press: Oxford, New York, 2013.

(24) Hussey ǁ, N. E.; Takenaka, K.; Takagi, H. Universality of the Mott–Ioffe–Regel Limit in Metals. *Philos. Mag.* **2004**, *84* (27), 2847–2864. https://doi.org/10.1080/14786430410001716944.

(25) Shen, G.; Chen, M.; Guyot-Sionnest, P. Synthesis of Nonaggregating HgTe Colloidal Quantum Dots and the Emergence of Air-Stable n-Doping. *J. Phys. Chem. Lett.* **2017**, *8* (10), 2224–2228. https://doi.org/10.1021/acs.jpclett.7b00775.

(26) Zhang, H.; Guyot-Sionnest, P. Shape-Controlled HgTe Colloidal Quantum Dots and Reduced Spin–Orbit Splitting in the Tetrahedral Shape. *J. Phys. Chem. Lett.* **2020**, *11* (16), 6860–6866. https://doi.org/10.1021/acs.jpclett.0c01550.

(27) Nag, A.; Kovalenko, M. V.; Lee, J.-S.; Liu, W.; Spokoyny, B.; Talapin, D. V. Metal-Free Inorganic Ligands for Colloidal Nanocrystals: S2–, HS–, Se2–, HSe–, Te2–, HTe–, TeS32–, OH–, and NH2– as Surface Ligands. *J. Am. Chem. Soc.* **2011**, *133* (27), 10612–10620. https://doi.org/10.1021/ja2029415.

(28) Tang, J.; Kemp, K. W.; Hoogland, S.; Jeong, K. S.; Liu, H.; Levina, L.; Furukawa, M.; Wang, X.; Debnath, R.; Cha, D.; Chou, K. W.; Fischer, A.; Amassian, A.; Asbury, J. B.; Sargent, E. H. Colloidal-Quantum-Dot Photovoltaics Using Atomic-Ligand Passivation. *Nat. Mater.* **2011**, *10* (10), 765–771. https://doi.org/10.1038/nmat3118.

(29) Chu, I.-H.; Radulaski, M.; Vukmirovic, N.; Cheng, H.-P.; Wang, L.-W. Charge Transport in a Quantum Dot Supercrystal. *J. Phys. Chem. C* **2011**, *115* (43), 21409–21415. https://doi.org/10.1021/jp206526s.

(30) Prodanović, N.; Vukmirović, N.; Ikonić, Z.; Harrison, P.; Indjin, D. Importance of Polaronic Effects for Charge Transport in CdSe Quantum Dot Solids. *J. Phys. Chem. Lett.* **2014**, *5* (8), 1335–1340. https://doi.org/10.1021/jz500086c.

(31) Thompson, J. C.; Younglove, B. A. Thermal Conductivity of Silicon at Low Temperatures. *J. Phys. Chem. Solids* **1961**, *20* (1), 146–149. https://doi.org/10.1016/0022-3697(61)90146-9.

(32) Glassbrenner, C. J.; Slack, G. A. Thermal Conductivity of Silicon and Germanium from 3\ifmmode^\circ\else\textdegree\fi{}K to the Melting Point. *Phys. Rev.* **1964**, *134* (4A), A1058–A1069. https://doi.org/10.1103/PhysRev.134.A1058.

(33) Brotzen, F. R.; Loos, P. J.; Brady, D. P. Thermal Conductivity of Thin SiO2 Films. *Thin Solid Films* **1992**, *207* (1), 197–201. https://doi.org/10.1016/0040-6090(92)90123-S.

(34) Nika, D. L.; Pokatilov, E. P.; Balandin, A. A.; Fomin, V. M.; Rastelli, A.; Schmidt, O. G. Reduction of Lattice Thermal Conductivity in One-Dimensional Quantum-Dot Superlattices Due to Phonon Filtering. *Phys. Rev. B* **2011**, *84* (16), 165415. https://doi.org/10.1103/PhysRevB.84.165415.

(35) Yang, B.; Liu, J. L.; Wang, K. L.; Chen, G. Simultaneous Measurements of Seebeck Coefficient and Thermal Conductivity across Superlattice. *Appl. Phys. Lett.* **2002**, *80* (10), 1758–1760. https://doi.org/10.1063/1.1458693.

(36) Hooge, F. N. 1/f Noise Sources. *IEEE Trans. Electron Devices* **1994**, *41* (11), 1926–1935. https://doi.org/10.1109/16.333808.

(37) McWhorter, A. L. (Alan L.; Laboratory, L. 1/f Noise and Related Surface Effects in Germanium. **1955**.

(38) Vandamme, L. K. J.; Hooge, F. N. What Do We Certainly Know About $\hbox1/F$ Noise in MOSTs? *IEEE Trans. Electron Devices* **2008**, *55* (11), 3070–3085. https://doi.org/10.1109/TED.2008.2005167.

(39) Lai, Y.; Li, H.; Kim, D. K.; Diroll, B. T.; Murray, C. B.; Kagan, C. R. Low-Frequency (1/f) Noise in Nanocrystal Field-Effect Transistors. *ACS Nano* **2014**, *8* (9), 9664–9672. https://doi.org/10.1021/nn504303b.

(40) Peransin, J.-M.; Vignaud, P.; Rigaud, D.; Vandamme, L. K. J. 1/f Noise in MODFETs at Low Drain Bias. *IEEE Trans. Electron Devices* **1990**, *37* (10), 2250–2253. https://doi.org/10.1109/16.59916.

(41) Rhayem, J.; Valenza, M.; Rigaud, D.; Szydlo, N.; Lebrun, H. 1/f Noise Investigations in Small Channel Length Amorphous Silicon Thin Film Transistors. *J. Appl. Phys.* **1998**, *83* (7), 3660–3667. https://doi.org/10.1063/1.366586.

(42) Liu, H.; Lhuillier, E.; Guyot-Sionnest, P. 1/f Noise in Semiconductor and Metal Nanocrystal Solids. *J. Appl. Phys.* **2014**, *115* (15), 154309. https://doi.org/10.1063/1.4871682.

Chapter 4: Intraband Transition of HgTe Nanocrystals for Long-Wave Infrared Detection at 12 Microns

In Chapter 3, I studied the charge carrier mobility and the conductance of highly monodispersity sample of HgTe.

The improvement in the transport properties and the lowering of the 1/f noise make HgTe a promising material for infrared detection. Traditionally, infrared photodetection with HgTe uses the interband transition, mostly due to HgTe film have an air-stable intrinsic doping level in the mid-wave and long-wave infrared range. However, the synthesis of large monodispersed HgTe presented allows for controlled n-type doping up to 2 electrons per dot. This enables the intraband transitions to be studied and used in the detection of long-wave infrared light.

Recently, intraband detectors have been made using HgSe CQDs. The greatest advantage of HgSe is the ease of doping due to the naturally populated $1S_e$ states. However, the synthesis of HgSe is not as well controlled as HgTe resulting in poor monodispersity. This causes the mobility of HgSe even after ligand exchange to be an order of magnitude lower than that of HgTe, resulted in HgSe intraband photodetectors having lower detectivity when compared to interband HgTe of the same wavelength. Therefore, study of the intraband transition of HgTe will be beneficial both for understanding its optical properties as well as the making good intraband photodetectors.

In this chapter, I will discuss improvements in synthesis that leads to a stable n-doping of HgTe CQDs with intraband transition in the long-wave infrared range. Its optical properties are characterized, and the temperature dependence of this transition explained using a 14-band model. Finally, I use this film of HgTe to demonstrate a device detectivity over 10^7 Jones at 11 μm. The highest value to date for a long-wave CQD photodetector.

4.1 Introduction

Infrared optoelectronic devices uses mostly crystalline materials, such as InGaAs or HgCdTe and epitaxial superlattices with intersubband transitions.[1,2] Colloidal quantum dots (CQDs) proves to have potential in the field as they have optoelectronic properties that can be readily tuned by controlling the nanocrystal size, shape, and surface passivation.[3–6] Most research on these materials has focused on their interband transitions, which occur between the quantum confined states derived from the bulk valence and conduction bands. However, intraband photodetectors could be advantageous due to its independence on the band gap. [5] The intraband transitions, which are transitions between the quantum confined states within one band have no such restriction. This is potentially advantageous especially in the mid-wave (3-5 microns) and long-wave (8-12 microns) infrared, where there are very few bulk semiconductors with small enough bandgaps.[7]

CQD intraband photodetectors have started to be explored in the mid-wave infrared (MWIR) with quantum dots that include HgSe, HgS, Ag_2Se and PbS.[7–12] HgSe is the most studied because it shows ambient n-doping. Ag_2Se is the main example of a wider gap and low toxicity material that also shows stable ambient n-doping and is being investigated as a intraband photodetector.[8,13] Lead-chalcogenides CQDs do not satisfy the low toxicity requirement but stable n-doping has been recently achieved.[14,15] This has led to the study of the intraband transition of PbS quantum dots close to the long-wave infrared (LWIR) range, and to the demonstration of photoconductive devices up to 8 microns.[15,16] The cubic lead chalcogenides have a 4-fold degeneracy of the band gap. As a result, an intraband detector needs n-type doped CQDs with 8 electrons per dot in order to achieve the maximum intraband absorption as well as the minimum dark current.

A previous demonstration of LWIR detection with CQDs used the interband transition of rather large CQDs, between 15-20 nm HgTe CQDs, and it showed photoconduction up to 12 microns.[16]

The same coverage could, in principle, be obtained with the intraband absorption of smaller HgTe CQDs, around 12-15 nm, which can be stably n-doped in ambient condition.[17] The potential advantage over PbS is that the absorption of the intraband transition is maximized with only 2 electrons doping due to the 2-fold spin degeneracy of the $1S_e$ state. Moreover, the multiple degeneracy (2 x 4 = 8) of the $1S_e$ state in PbS might contribute to a broadened lineshape compared to the 2-fold degeneracy in HgTe.[18] Additionally, in HgTe CQDs, there is a sizable spin-orbit splitting of the $1S_e$-$1P_e$ transition, such that a distinct lower energy transition emerges which is assigned to $1S_e$-$1P_{e1/2}$.[19] It is singly degenerate, except for spin, and could therefore be quite narrow, limited by size distribution and thermal broadening, which makes it a good candidate for LWIR photodetection. This work reports on the absorption coefficient, linewidth, and temperature dependence of this intraband transition of the quasi-spherical HgTe quantum dots, and it explores its use in a thin photoconductive device.

4.2 Synthesis of N-type quantum dots

HgTe CQDs with an intraband transition in the 10-micron range require an average size in the 12-15 nm range. The doping depends on the conditions of the reaction as well as the reactivity of the precursors. The synthesis using TMSTe produces naturally n-doped quantum dots,[19] and in this work, the synthesis is adjusted to dope the HgTe CQD close to $2e^-$ / dot to obtain the lower energy intraband transition between $800cm^{-1}$ and $1000cm^{-1}$.

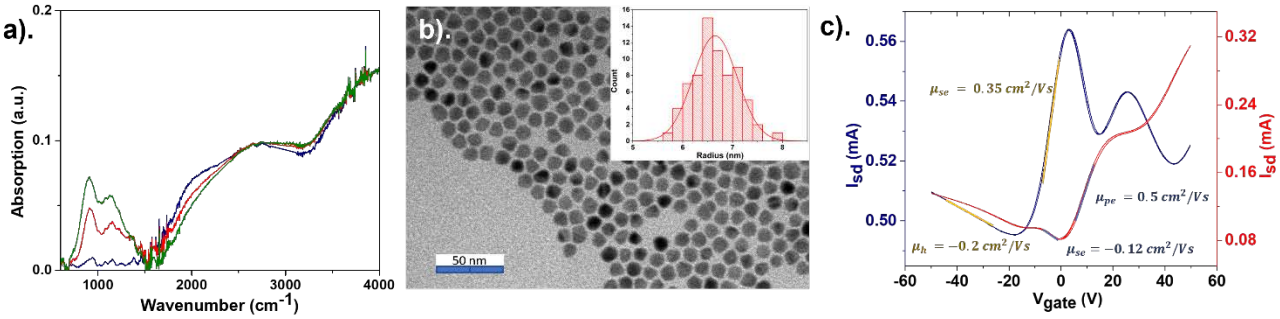

Fig. 4-1. a). Absorption spectra of HgTe CQDs film. The blue spectrum is prepared from the quenched and cleaned reaction mixture and then rinsed with a solution of isopropanol and 2% EDT. Red spectrum, $HgBr_2$ is added before quenching the reaction mixture, the film is rinsed with a solution of isopropanol and 2% EDT/HCl. Green spectrum, same film as the red spectrum after rinsing with a solution of $HgBr_2$/TBP. b). TEM image of the synthesized HgTe CQD, inset: radius histogram. c). FET conductance of the HgTe film at two doping levels, 1e/dot (Blue) and 2e/dot (Red) doping of the $1S_e$ state.

The synthesis follows Shen et al.[19] It involves dissolving 0.2 mmol of $HgCl_2$ in 4ml of oleylamine (OAm), while stirring on a hot plate under an inert atmosphere, at 90°C for 30 min to ensure that the solid is fully dissolved. The temperature is then raised to 110°C before injecting 0.1 mmol of TMSTe prediluted in 500 µl of toluene. The solution turns black immediately and is left to react for 5 mins before quenching by adding 5ml of TCE. The dots are then cleaned twice by precipitation with methanol and redissolution in chlorobenzene. Films are made by drop-casting in ambient conditions. The OAm ligands are removed by rinsing the films with solutions of 2% ethanedithiol (EDT) and 2% hydrochloric acid (HCl) dissolved in isopropanol (IPA) to make the CQD film conductive. The resulting film absorption at this point is shown as the blue curve Fig.

1a. Though the starting dot in solution is n-doped, after the EdT/HCl/IPA treatment in air, there is little residual n-doping. This complicates intraband device fabrication, as the EdT ligands exchange provides conductivity, but also partially removes the n-doping and diminishes the intraband absorption. Therefore, a modified synthesis and film preparation is necessary. The first modification to the synthesis is to add additional Hg^{2+} ions during the reaction. It has been shown that exposing the HgTe CQD solutions or films to more Hg^{2+} ions increase the n-doping.[20–22] This is explained by a decreased electronic potential energy due to presence of Hg^{2+} attracting negative ligands, forming a dipole which stabilizing the electron states in the HgTe CQD to be more n-type. Similarly, polar solution exchange in the presence of excess Hg^{2+} allows to tune the n-doping of the resulting inks.[17,23] Therefore, we first increase the doping in the solution by adding Hg^{2+} in the reaction mixture prior to quenching. A high excess concentration,10-fold or more, leads to rapid and complete dissolution of the colloids, whereas a 4-fold excess or less, does not lead to rapid dissolution but increases the n-doping. To increase the doping, we therefore dissolve 0.2 mmol of $HgBr_2$ in 500 µl of OAm and inject the solution into the reaction mixture at 110ºC, 4 min after the start of the reaction, and the solution is quenched with TCE 1 min afterwards. The quenching prevents potential etching and Ostwald ripening that would eventually take place. The solution is then precipitated with isopropanol and redispersed in chlorobenzene, and a second precipitation and redispersion is used before storage in chlorobenzene. The HgTe solution is then drop-cast in air on a substrate to make a film of 50-100 nm. At this stage, the film doping is around 1e-/ dot corresponding to the red spectrum in Fig. 4-1a).

In order to further increase the doping to $2e^-$/dot, the films are rinsed at 60ºC for 1 minute with a solution of $HgBr_2$ (0.01mmol) and tributylphosphine (TBP) (400 µl) dissolved in 5 ml IPA. This

also increases the n-doping with only minor spectral changes, and the effect is assigned to the adsorption of Hg^{2+} while the TBP is a reductant that counters oxidation in air. Once the film is made, if the doping is not exactly at 2e-/dot, one can modify the doping by placing the samples in different atmospheric conditions. Leaving the films in air slowly lowers the n-doping whereas leaving films under dry N_2 within the infrared spectrometer compartment or under vacuum in a cryostat increases n-doping. This modification is weak but can serve to finely tune the doping before measurement.

The green spectrum in Fig. 4-1a shows data for a typical sample. As the intraband transitions around 1000cm^{-1} gain strength, the interband edge transition around 1700cm^{-1} is bleached, while the higher energy transition are unaffected. Fig.4-1b shows a TEM image of the synthesized dots with a size histogram and standard deviation of around 8%. The doping at 1 e^-/dot and 2 e^-/dot is verified in Fig.4-1c which shows FET data of the samples corresponding to the synthesis and synthesis + $HgBr_2$/TBP treatment.[20]

4.3 Intraband optical constants of HgTe CQD film

For mid-IR HgTe films, an index of refraction of 2.1 + 0.1i has been used to simulate the optical properties.[24] A slightly larger value of 2.25 + 0.13i has been reported for the same type of CQDs.[25] The precise value depends on the band edge, as well as the packing and shape and therefore the nature of the dots. Of particular interest here is the relative strength of the imaginary index between interband and intraband transitions, and their associated absorption coefficients. The refractive index for the intraband transition of HgTe CQDs is determined by fitting transmission data of a

thin film of measured thickness. The CQD solution is drop-cast on a ZnSe window in a single cast and rinsed with EdT/HCl to obtain a fairly intrinsic sample. The ZnSe plate is used because its refractive index of ~2.41 is close to the refractive index of HgTe films, thus reducing the error from the difference in reflection of the HgTe film and the ZnSe itself. The thickness of this film is 80nm, measured using the LEXT microscope.

The position and angle of the sample are maintained during temperature dependent measurements to minimize potential variation due to film thickness and angle of incidence. This also means that changing the doping once the film is deposited cannot be done using the $HgBr_2$/TBP method described in the synthesis section, since this requires moving the sample from the spectrometer. Therefore, the full intraband spectrum is constructed by first measuring two spectra at different doping levels after exposure to air and nitrogen atmospheres. Then, the $2e^-$/dot intraband spectrum is obtained by adding the difference spectrum of the two spectra until the absorbance is minimized between the intraband and interband transitions. The initial spectrum and the spectrum after waiting in a nitrogen atmosphere are shown in Fig. 4-2a). The raw spectra are processed to remove the vibrational features of hydrocarbons, CO_2 and water vapor. The constructed 2 e-/dot spectrum is shown in Fig. 4-2b). The raw transmission spectrum is shown in the appendix.

The absorption coefficient is given by $4\pi k/l$ where k is the imaginary index of refraction and l the wavelength. Thus, Fig. 4-2b already shows that the intraband absorbance at $850cm^{-1}$ is about 2 times that of the interband absorbance at 2400 cm^{-1} and this indicates readily a ~ 5 times larger absorption coefficient for the intraband if this difference is purely due to absorption.

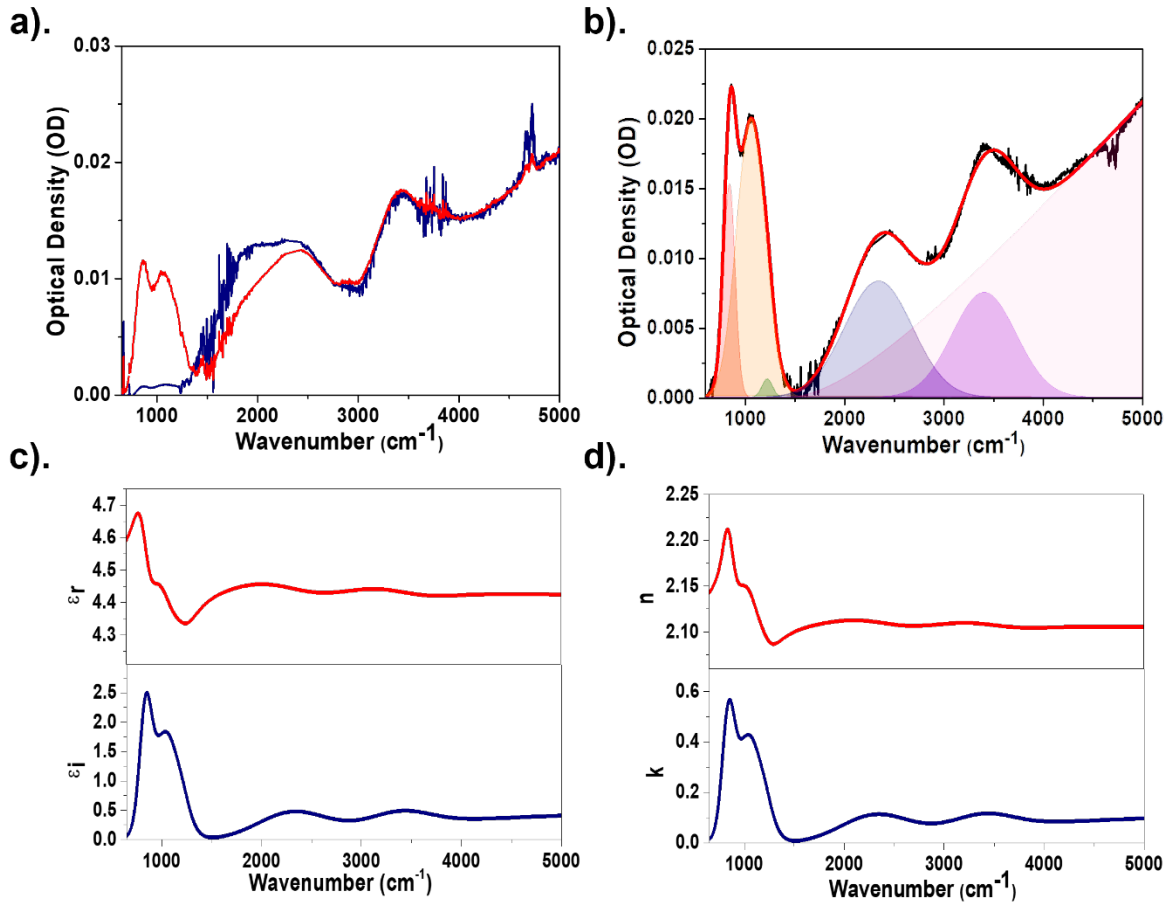

Fig. 4-2. a). Absorbance of the HgTe CQD film measured on a ZnSe plate, with two doping levels, after treatment with 2% EdT/HCl (Blue) and after 30 min in N_2 atmosphere (Red). b). Reconstructed absorbance spectrum when the intraband is fully doped and the first interband peak is bleached. The spectrum is then fitted with 5 gaussian and a parabolic function. c). Derived values of ε_r and ε_i. d). n,k values calculated from the εr and ε_i.

Fig 4-2. b) is fitted with 5 Gaussian and one parabolic/linear function

$$f(\tilde{\upsilon}) = \sum_{i=1}^{5} A_i \, e^{-\left(\frac{(\tilde{\upsilon}-\mu_i)^2}{2\sigma_i^2}\right)} + B_0 \, H(\tilde{\upsilon} - \upsilon_0) \frac{(\tilde{\upsilon} - \upsilon_0)^2}{\tilde{\upsilon}}$$

where $H(\tilde{\upsilon} - \upsilon_0)$ is the Heaviside function which equals to 1 when $\tilde{\upsilon} > \upsilon_0$.

The parameters used to fit the spectra is given as

	A_i	μ_i (cm^{-1})	σ_i(cm^{-1})

Gaussian 1	0.01529	842.37	58.19
Gaussian 2	0.02002	1059.49	144.11
Gaussian 3	0.00131	1223.54	53.75
Gaussian 4	0.00833	2345.73	341.66
Gaussian 5	0.00754	3409.95	323.11

	B_0	$v_0(\text{cm}^{-1})$
Parabolic	8.257×10^{-6}	1418.42

The resulting function is used for the calculation for ε_r and ε_i.

To account for possible changes in reflection, the complex dielectric constant must be determined. To do this, the transmission spectrum is first fitted with five Gaussian functions plus one parabolic function above the band gap as shown in Fig. 4-2b). The imaginary part of the dielectric constant is then calculated from a linear combination of five Gaussians with the same fixed positions and widths, and with adjustable amplitudes. The real part of the dielectric constant is calculated using the Kramers-Kronig relationship with the integral limited to 500cm^{-1} and 7000cm^{-1}, plus a constant ε_∞. Since the transmission spectrum is not very sensitive to the real index of refraction, ε_∞ is chosen such that the real refractive index n = 2.1 at high frequency in order to match previous determinations.

A simple algorithm is then used to adjust the amplitudes to best fit the experimental spectrum. Using the dielectric constants and a film thickness of 80 nm, the transmission spectrum of the film on the ZnSe plate is simulated using the transfer matrix method. The amplitudes are iteratively adjusted in order to minimize the square difference between the calculated and experimental spectra. A more detailed description of the fit and numerical algorithm is discussed in the below in Fig. 4-3. The calculated real and imaginary index of refraction for the film are shown in Fig. 4-2c. The associated real and imaginary refractive index n, k are shown in Fig. 4-2d.

Flow Chart for the Algorithm is given as

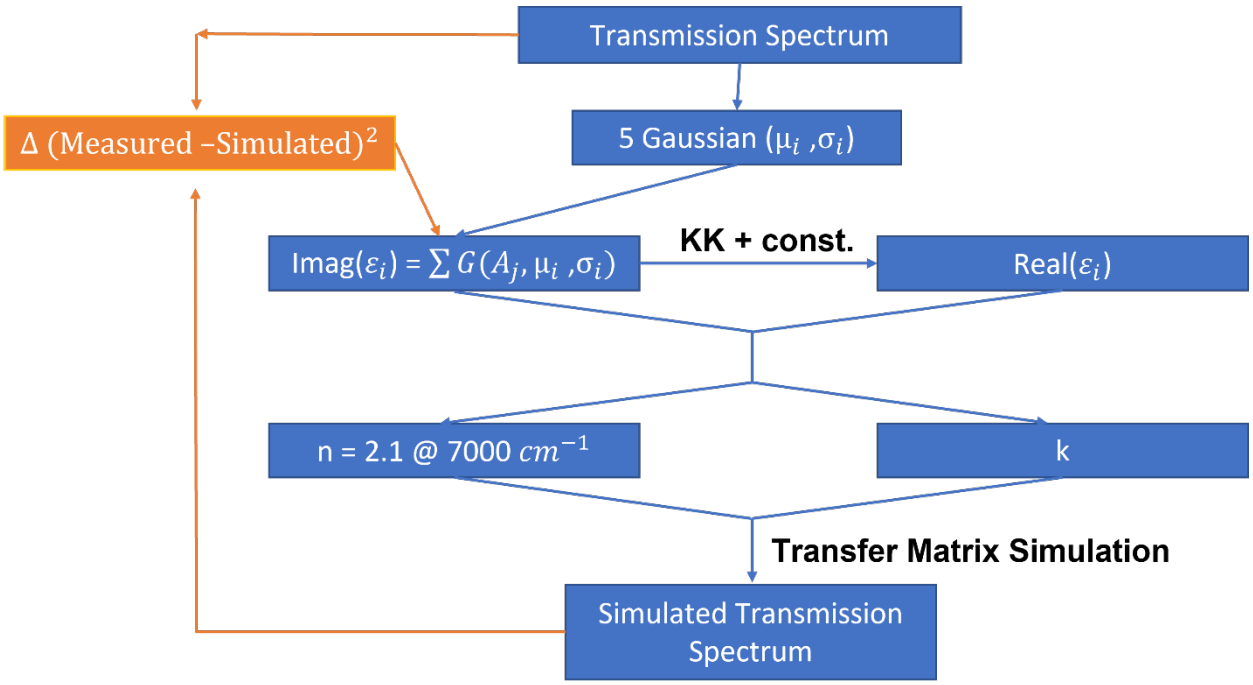

Fig. 4-3, Flow chart for the simulation algorithm for calculating the dielectric constants of the HgTe film.

The real and imaginary index of the dielectric constant is calculated using the following algorithm.

1. From the Transmission Spectrum, fit the data with the 5 Gaussian functions with amplitudes A_i, peak position μ_i and width σ_i. We take this fitted spectrum in Fig. 2b. to be the baseline transmission spectrum for optimization such that the spectrum noise is minimized.
2. Construct the imaginary dielectric constant using 5 Gaussians with the same peak position μ_j and width σ_j, but with a guessed initial amplitude $\tilde{A}_j$. The imaginary dielectric constant is chosen to be fixed at the value after the 5th Gaussian at 3400 cm^{-1}.

3. Using the Kramers-Kronig Relations, the real dielectric constant is calculated from the imaginary dielectric constant by the following formula:

$$\varepsilon_r(\omega) = \frac{2}{\pi}\boldsymbol{P}\int_{500}^{7000}\frac{\omega'\varepsilon_i(\omega')}{\omega'^2-\omega^2}d\omega' + const.$$

where $\varepsilon_i(\omega')$ is the imaginary dielectric constant at wavenumbers from 500 cm^{-1} to 7000 cm^{-1}. The constant in this equation is used to address the fact that the integral is only between a limited range. This constant is chosen to be around ~4.4 at 7000 cm^{-1} such that, when calculating the real dielectric constant n from the dielectric constant, $n = 2.1$ is fixed at 7000 cm^{-1}.

4. n and k values calculated at every wavenumber ω using the simulated dielectric constant.
5. Using the n and k values calculated, we use the TMM simulation for the transmission of the 80 nm HgTe film on the ZnSe plate, taking ZnSe plate to be the background.
6. The square difference of this spectrum is calculated.

$$S = \sum_{500}^{7000}(t_{sim}(\omega) - t_{fitted}(\omega))^2$$

7. Step 2-6 is repeated iteratively such that we optimize the value $\tilde{A}_j$ in step 2 so S is minimized.

The *k* value in the interband absorption region is close to 0.1, similar to the previously reported optical constants. However, a much higher *k* of 0.6 is attained at the peak of the intraband transition around 1000cm^{-1}. The corresponding absorption coefficient is $4\pi k/l$ = 7500 cm^{-1}. For comparison, the absorption coefficient is ~ 3000 cm^{-1} for bulk MCT around 10 microns.[7] The intraband absorption of the HgTe CQDs films is therefore very strong, greater than bulk MCTs despite the

moderate packing density of CQDs. The strength of the intraband absorption is therefore an interesting advantage over the interband transition.

4.4 Temperature dependence of the HgTe CQD intraband transition

The temperature dependent spectra of the HgTe CQD film are shown in Fig. 4-4a. They are measured using FTIR transmission of a thin film of HgTe CQDs on a ZnSe window inside a cryostat with front and back ZnSe windows. These windows prevent measurement below ~ 600 cm^{-1}, thus absorbance is not meaningful below 750 cm^{-1}.

The intraband transitions blue shift and narrows upon cooling to 80K while the spin-orbit splitting increases and the interband transition redshifts. The energies of the intraband and interband transitions are shown in Fig. 3b. The thermal shift, defined as the slope dE/dT, is positive for the interband transition and negative for the intraband transition.

The thermal shifts of semiconductor bandgaps are typically fitted with empirical models, while being physically attributed to the increasing atomic motion which changes the energy of the bands.[26] Fan introduced a 2nd order perturbation model for electron-phonon coupling to describe the thermal shift of wide gap semiconductors.[27] With wide gaps, the lowest energy state of a band couples only with higher energy states within the same band, and this 2nd order intraband coupling leads always to a negative thermal shift, which narrows the gap at high temperatures. Keffer et al later showed that, with narrow gap semiconductors, interband coupling becomes possible and it can induce a positive thermal shift.[28] Moreover, the bands themselves move in various directions with temperature.

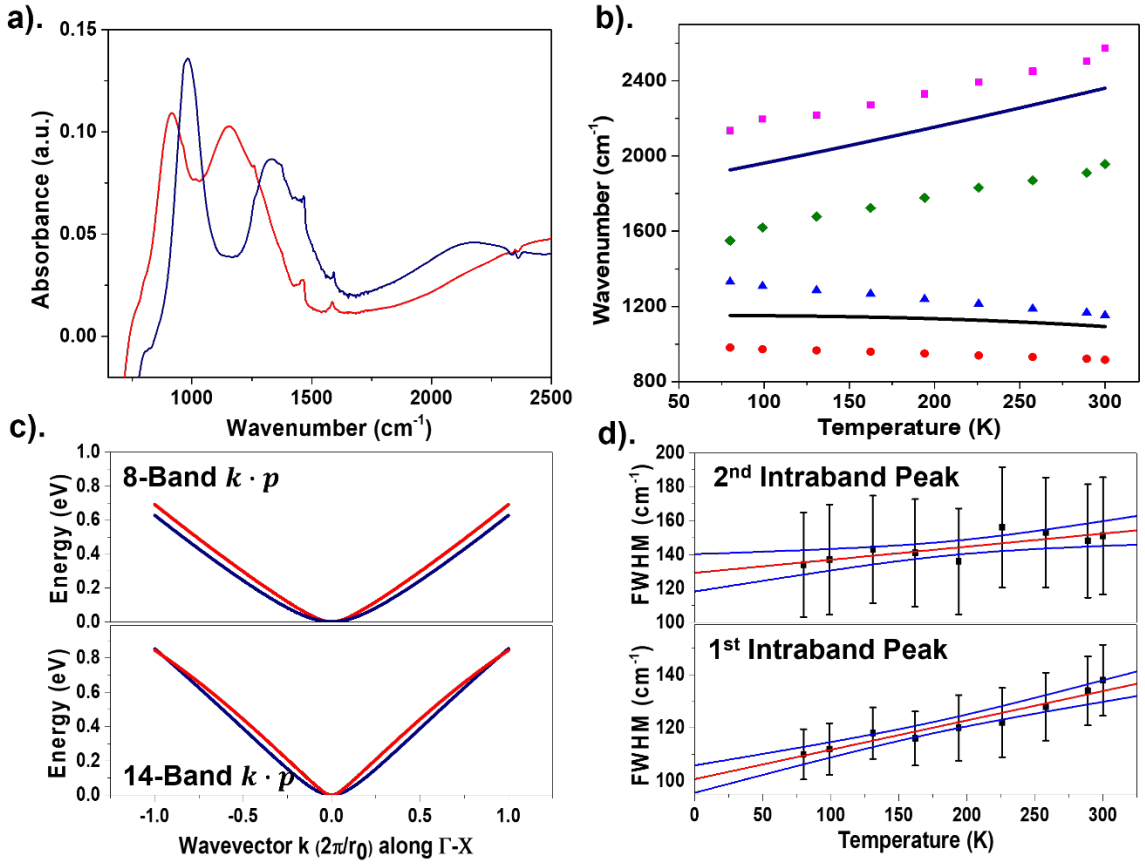

Fig. 4-4. a). Intraband absorption of LWIR infrared HgTe QD from 80K (Blue) to 300K (Red). Measured on the ZnSe substrate. b). Prediction of the intraband (Black) and interband (Blue) transition position using the 14-band model. Experimental data are shown as dots (1^{st} Intraband: Red, 2^{nd} Intraband: Blue, 1^{st} Interband: Green). c). Conductance band structure of the 14-band k.p model (below) and 8-band k.p model (above), dot radius r_0 = 6.6 nm. (80K: Blue, 300K: Red) d). FWHM of the 1^{st} and 2^{nd} intraband absorption peak and extrapolating the inhomogeneous linewidth for the two transitions.

For CQDs, Olkhovets et al first reported the thermal shifts of PbS and PbSe CQDs and observed that they were positive for large particles and negative for small particles.[29] Their qualitative explanation followed Keffer et al. As the large particles follow the bulk band gap, their interband coupling dominates and leads to a positive shift. For the highly confined particles, the intraband coupling dominates giving a negative thermal shift. HgTe nanocrystals showed qualitatively similar behavior.[25] The opposite thermal shift for intraband and interband transitions, seen here as well as in PbS and HgSe CQDs.[15,30] Following Olkhovets et al, Ramiro et al qualitatively argued that $1S_e$, being the lower energy state of the conduction band, has a stronger negative thermal shift than $1P_e$, which then explains a negative thermal shift of $1S_e$-$1P_e$.[29,31,32] However, one also could qualitatively argue that the $1S_e$ is closer to the valence band state than $1P_e$, and that the interband coupling gives it a stronger positive thermal shift than $1P_e$, and reach the oppositive conclusion. Qualitative electron-phonon coupling arguments therefore do not seem very satisfying.

An alternative explanation could rely on a good and independent description of the bands and their temperature dependence. A first order description of the conduction band of HgTe or HgSe is a 2-band or 8-band $k \cdot p$ model. In these models, the only temperature dependent parameter is the gap between the Hg and Te Bloch functions at the Γ point.[33] With a gap varying from -0.31eV at 0 K to -0.15eV at 300 K, the 8-band $k \cdot p$ conduction band is shown in Fig. 4-4c. Assuming a simplistic infinite spherical boundary conditions, the $1S_e$ state is at a wavevector p/R and the $1P_e$ state at 4.49/R. The lower temperature pulls the band down and this reduces the interband energy since the massive hole state is nearly nondispersive. This 8-band model therefore describes the interband thermal shift of large HgTe particles well. However, it fails to reduce or invert the thermal shift for the small particles, and it fails to produce a negative thermal shift for the intraband transition.

The reason is clear in Fig. 4-4c, which shows that the conduction band at 80K is mostly shifted upwards at 300K. This predicts a very small positive thermal shift of the intraband transition, as seen in Fig. 4-4b, which is opposite to what the experimental data have shown.

With the failure of the 8 band model, we explored a 14-band model recently introduced by Moghadam et al, who built it to explain the negative thermal shift of highly confined HgTe platelets, and the effects of pressure, rather than resorting to electron-phonon coupling arguments.[34] The model introduces a second conduction band around 2.2 eV above the band gap, with $k \cdot p$ interactions to the first conduction and the valence band. We then used the same model with slight adjustment to account for the difference in dot size to better model the energy transitions. As shown in Fig. 4-4c, at higher k-values, the increasing interaction with the upper band pushes the first conduction band downward with a stronger curvature at 300K than at 80K. As a result, the slope between $1S_e$ and $1P_e$ is smaller at 300K than at 80K which leads to a negative thermal shift, in the same direction as the experiment. It is this new downward curvature that gives the fair rendering of the thermal shifts of both the interband and intraband shown in Fig. 4-4b. The model is described in the Section 4-9. Admittedly, we use a very simplistic description of the quantum dot states. The additional conduction band and its position will have to be supported by other measurements, and a theory of the quantum dot states will have to include the spin-orbit splitting. Nevertheless, we believe that the thermal changes of the band structure should provide a better explanation than qualitative electron-phonon coupling arguments, while the spectroscopic data can help refine the band parameters.

4.5 HgTe intraband homogeneous and inhomogeneous broadening

The narrowing of the spectra in Fig. 4-4d is striking. With the FWHM of the intraband absorption decreasing from 130cm^{-1} to 110 cm^{-1} to 80K, this is about one third of the interband transitions widths for HgTe CQDs, and it may be the narrowest ensemble linewidth reported for colloidal quantum dot electronic transitions. The inhomogeneous linewidth should arise mostly from the variation in size and shape, and be temperature independent.[30] With this assumption, extrapolating to 0 K, the inhomogeneous linewidth of $1S_e$-$1P_{e1/2}$ is ~100 cm^{-1}. The TEM-derived size distribution standard deviation of 8% shown in Fig. 4-1b, implies a larger inhomogeneous FWHM of 167 cm^{-1} using the dispersion from the 14-band model. It is possible that the size distribution is narrower than the TEM size distribution, which could be broadened by the various projections of the quasi-spherical shapes.

The homogeneous width is typically due to dephasing by electron-phonon coupling.[21,36] With acoustic phonons or low energy optical phonons as for HgTe, the homogeneous linewidth is expected to increase linearly with temperature.[37–39] We can then extract some measure of the the homogeneous width from the temperature dependence. The convolution of a Gaussian and a Lorentzian gives a Voigt lineshape[40] with a width given by

$$f_v \sim \frac{f_L}{2} + \sqrt{\frac{f_L^2}{4} + f_G^2}$$

where the Gaussian widths, f_G, is taken to be 100cm^{-1}, and the Lorentzian width is f_L. The Lorenzian homogeneous linewidth f_L is then calculated to be 70 ± 15 cm^{-1} at room temperature. The narrow width is relevant as it minimizes dark current from low energy thermal excitation and is also relevant for electron transport.

Finally, the spectra show an increasing spin-orbit splitting at low temperatures. The very large

splitting of 400cm^{-1} has previously been discussed by Delerue and coworkers within a tight binding model,[33] and it will be interesting to refine the model and explain the thermal trends.

4.6 Intraband detection and HgTe CQDs

The intraband transition is strongly absorbing, narrow, tunable within the thermal IR detection range of 8-12 microns and is weakly temperature dependent. We therefore explored its use as a LWIR photoconductor using a film prepared as discussed above. In order to maximize the device absorption at 10 mm, we used a ¼ wave reflector as a substrate. An FET is also present on the substrate and is used to measure the doping of the CQD film.

The photoresponse spectrum of the film is measured with an FTIR spectrometer in regular scanning mode. The spectrum shown in Fig. 4-5a is taken at 80K, showing a photoresponse in the 8–12-micron range. It is normalized to the response of a DTGS pyroelectric detector, by dividing by the DTGS spectrum. This should approximately follow the absorption spectrum and spectral detectivity for a fast photon detector. The spectrum is compared to a simulated absorption spectrum calculated using the transfer matrix method and the optical constants determined at room temperature and extrapolated to low temperatures (See Section 4.11). The result is shown in Fig 4-5a and is in a fair agreement except for the additional narrow features around 10-12 microns, which we tentatively assign to interference effects within the interdigitated electrodes.

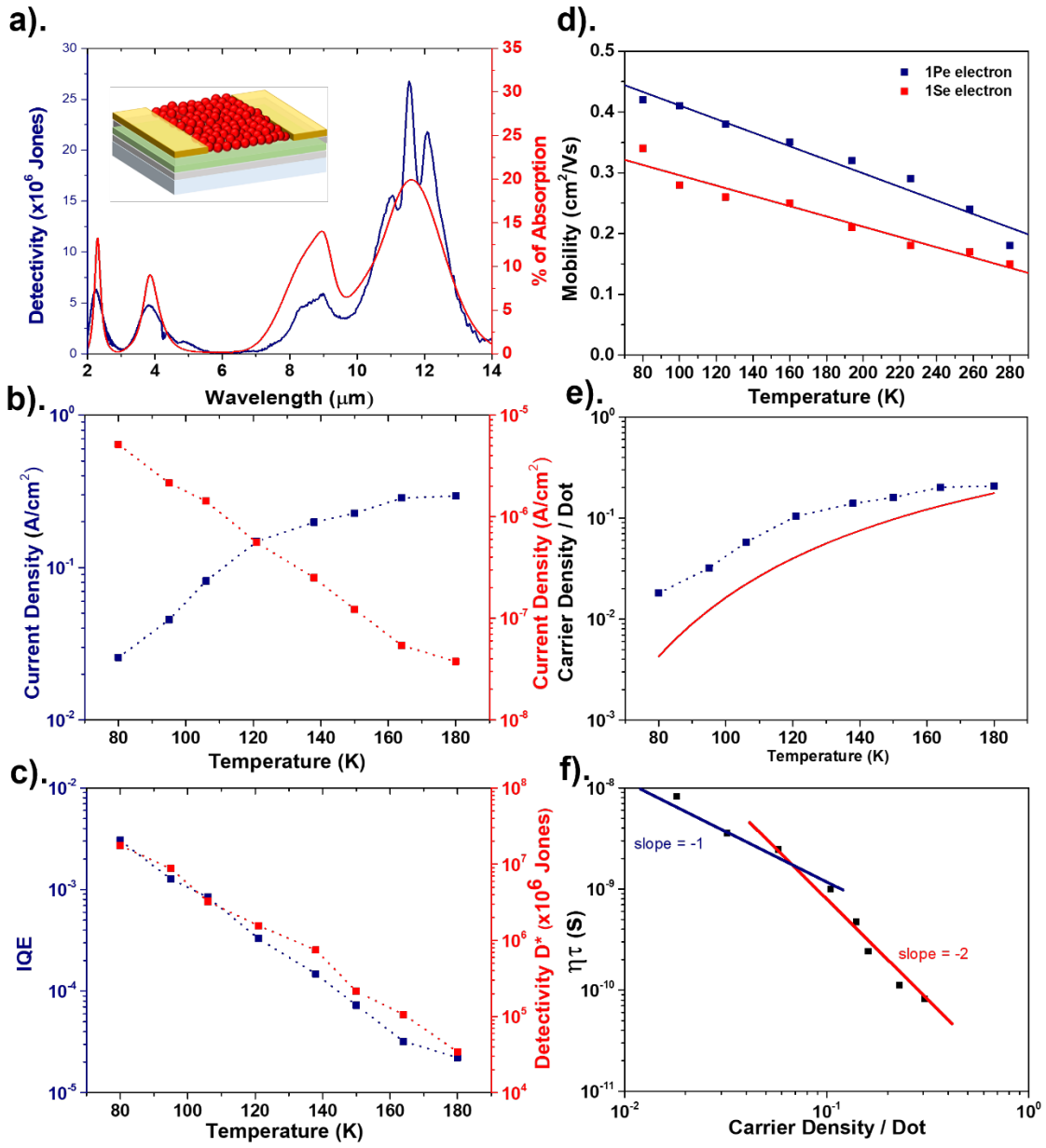

Fig. 4-5. a) Spectral Detectivity D* (Blue) and Simulated Absorption of the 80 nm HgTe film, using n,k value from Fig 2d.) b). Measured dark current density (Blue) and photocurrent density (Red). c) IQE (Blue) assuming the simulated absorption and D* (Red). d). Measured mobility of $1S_e$ and $1P_e$ e). Carrier /dot (Blue) derived from the dark current and expected intrinsic values (Red). f) Value of ητ derived from the photocurrent as a function of the carrier/dot.

The photoresponse is from a blackbody at 873 K of 3.46 cm^2 area and placed 15 cm away. The photocurrent and dark current densities are shown in Fig. 4-5b. The absorption, α, is calculated using the measured film thickness d = 80nm, and the absorbed photon flux, Φ_{abs}, is then calculated using the dielectric constants and frequency shifts determined above. The internal quantum efficiency (IQE) is then given by $IQE = J_l/e\Phi_{abs}$ where J_l is the photocurrent and e is the electric charge. The IQE is 3 x 10^{-3} at 80K, as shown in Fig. 4-5c. No photoresponse could be detected above 180K. The noise is largely dominated by 1/f noise at 500Hz, and detectivity is quoted for 500Hz. The peak detectivity is then D* = 1.65 x 10^7 Jones at 80K at 12 microns, with a rather sharp drop-off by 14 microns. The detectivity is 3 orders of magnitude lower than commercial MCT detectors, but it is an improvement compared to the previous reports of intraband PbS at 8 microns, and interband HgTe in the 10 mm range.[18,41]

The data are analyzed further to provide insight into the performance limitations.[42] The IQE of 3 x 10^{-3} is assigned to the small ratio of the drift length (L_{drift}) to channel length (L= 10 mm), and to the charge carrier generation efficiency, η, with $IQE = \eta\left(\frac{L_{drift}}{L}\right)$. Assuming unity efficiency of carrier generation, the drift length is then only 30 nm, such that the carriers barely move a few quantum dots across at low temperature. The carrier mobility is measured by FET using the largest slopes on either side of the $1S_e$ and $1P_e$ states, and they are shown in Fig. 4-5d. The mobilities have a weak negative temperature dependence from 0.2 cm^2/Vs to 0.4 cm^2/Vs for 180 K and 80 K respectively, with the $1S_e$ mobility slightly smaller than the $1P_e$ mobility. Prior results with this size of HgTe CQDs and higher mobility with hybrid ligand exchange, showed also a negative temperature dependence in this temperature range.[20] With the mobility, we estimate a carrier lifetime τ by $L_{drift} = \mu\left(\frac{V}{L}\right)\tau$. With the voltage applied V = 0.5V, the analysis gives very short

carrier lifetime of ~ 10 ns at 80K, dropping to 100 ps at 180K.

The carrier lifetime can be due to trapping, geminate recombination, and Auger relaxation. Insight into the mechanism can then be obtained by relating the lifetime to the carrier density. To determine the carrier density, we model the dark current density as $J_0 = \left(n_0\mu_e + p_0\mu_p\right)\frac{d}{V_{dot}}\frac{eV}{L^2}$ where n_0 and p_0 are the average carrier number in $1S_e$ and $1P_e$ states respectively. V_{dot} is the effective volume of the dot, including the dot and void volumes. Given the similar mobility in $1S_e$ and $1P_e$, the expression is simplified to $J_0 = (n_0 + p_0)\mu\frac{d}{V_{dot}}\frac{eV}{L^2}$. This equation is used to obtain the total carrier number $n_0 + p_0$ shown in Fig.4e. For this calculation, the dot radius is taken to be 6 nm and the packing fraction is taken to be 50%. The expectation for intrinsic doping is $n_0 + p_0 = 2\sqrt{N_vN_c}e^{-E_g/2k_BT}$ where E_g is the energy gap. We use $N_v = N_c = 2$ because the $1S_e$ state is two-fold degenerate like the $1P_{e1/2}$ state while the $1Pe_{3/2}$ state is likely not thermally populated at 80K. The energy gap is taken as the transition energy of $1S_e$-$1P_{e1/2}$, from the experimental data in Fig. 4-4b. As shown in Fig. 4-5e, the agreement is fair, but an intrinsic system would have a ~ 5 smaller dark current than observed ay 80K and this suggests that the system is not optimally intrinsic, or that the electronic gap is smaller than the $1S_e$-$1P_e$ transition energy.

The value of $\eta\tau$ derived from the photocurrent data can then be compared to the carrier density per dot, as shown in Fig. 4-5f. A trap-assisted relaxation would have no dependence on carrier density, germinate recombination would have a slope of -1, and Auger limited lifetime would have a slope of -2. The plot shows a possible slope change at around 10^{-1} carriers per dot, suggesting geminate recombination at 80 K and Auger relaxation at 180K. Auger relaxation was not expected because a proposed benefit of intraband transitions was that Auger would be reduced due to the

sparse density of state, based on prior works at 5 microns with interband HgTe CQD and with ~ $1e^-$/dot doped HgSe CQDs. [43,44] The reappearance of Auger for the larger intraband HgTe CQDs could be due to the lifting of the $1D_e$ degeneracy by spin orbit splitting, building up a density of state between $1P_e$ and $1D_e$. Since Auger elimination was one attractive aspect of intraband CQD photodetectors, this will need to be investigated further.

4.7 Conclusion

The intraband transitions of CQDs are attractive for infrared applications, since they offer a wide range of tunability with *a priori* a greater range of materials. This work expands the spectral range of investigation with the study of the intraband absorption of HgTe CQDs in the LWIR around $1000cm^{-1}$ or 10 microns. Spectroscopy shows that the intraband transitions of HgTe CQD has a 5-fold higher absorption coefficient than the interband transition, with an absorption coefficient peak value of $7500cm^{-1}$ which enables a strong absorption with thin films. Here we estimate a 20% absorption at 11 mm with a 80nm CQD film on a quarter wave reflector. Another beneficial feature is the smaller thermal shift of the intraband transitions. The magnitude and opposite signs of the interband and intraband thermal shifts were explained by a 14-band *k.p* model recently developed for HgTe. The linewidth of the intraband transition is remarkably narrow for infrared colloidal quantum dots with an inhomogeneous width of $100cm^{-1}$ and with a smaller homogeneous width of ~ $70cm^{-1}$ at room temperature. The spin orbit splitting is very large, nearly $400cm^{-1}$ for these LWIR quasi-spherical HgTe CQDs, and this might be of interest for future magneto-optical studies. The spin orbit splitting also spreads the density of conduction states and might allow Auger relaxation. This last point emerges indirectly from initial tests of the photoconduction properties which show a possible quadratic carrier density dependence of the carrier lifetime already at 180K. The quantitative photoconductor study shows that the lifetime is very short, about 10 ns at 80K

and that carriers barely travel over a few quantum dots given the moderate applied voltage and mobility in these films. Nevertheless, the good attributes that have been found for the intraband transition justify exploring this system further and possibly improving performance with higher mobility, longer lifetimes, shorter electrode spacings, and better control of the doping.

4.8 Methods

Materials. $HgCl_2$ (≥98%), $HgBr_2$ (97%), 1,2-ethanedithiol (≥98.0% (GC)), HCl (ACS reagent, 37%), iso-propanol (99%), ethanol (99%) and anhydrous solvents (tetrachloroethylene, hexane, methanol) were all purchased from Sigma-Aldrich and used as received. Oleylamine (technical grade, 70%) was purchased from Sigma-Aldrich and directly transferred to the nitrogen glove box before opening. The purified oleylamine was dried under dynamic vacuum at 120 °C for 2−3 h and stored in a nitrogen glovebox. Bis- (trimethylsilyl)telluride (98%) was purchased from Acros and stored frozen in a nitrogen glovebox.

HgTe Synthesis. The synthesis of HgTe CQDs is based on a previously reported method.[19] A solution of 54 mg $HgCl_2$ (0.2 mmol) and 8 mL oleylamine (OAm) is heated to 100^{o}C temperature under nitrogen until all $HgCl_2$ solids have dissolved. The solution is then cooled to the desired temperature for nanocrystal growth (85-95 °C, with larger nanocrystals obtained at higher temperature). Meanwhile, a solution of 28 μL of bis- (trimethylsilyl)telluride (TMS_2Te, 0.025 mmol or 0.075 mmol) in 500 μL OAm is prepared in a N_2 glovebox. The TMS_2Te solution is injected into the $HgCl_2$ solution and heated at the injection temperature for exactly 5 min. Then, a solution of $HgBr_2$ is quickly added to the reaction mixture and left stirring for 1 min. The reaction is quickly cooled by injection of 8 mL of anhydrous tetrachloroethylene (TCE) and cooled to room temperature under ambient conditions. After the reaction, the QDs are precipitated by the addition

of ethanol nonsolvent and subsequent centrifugation. The QDs are redispersed in chlorobenzene with 0.1 M didodecyldimethylammonium bromide (DDAB), 0.1 M trioctylphosphine oxide and 0.1 M of dodecanethiol to increase QD stability, and subsequently precipitated again with isopropanol and centrifugation. The resulting QDs are dispersed in chlorobenzene for optical measurements.

Device Fabrication. The device is built upon a silicon/silicon oxide wafer. A square 0.5 x 0.5 mm of Titanium is evaporated onto the silicon dioxide directly as a back reflector. Then, 10 nm of SiO_2, 1 μm of Si, and 100 nm of SiO_2 are subsequently grown by plasma enhanced chemical vapor deposition acting as the dielectric spacer. The top and bottom layer of SiO_2 serve to insulate the slightly conducting CVD-grown Si. A Pt interdigitated electrode is deposited on top of the spacer. The film of HgTe CQD is then drop-casted with the same procedure as described before, forming a final photoconductive device.

Optical Absorption. Infrared spectra were collected with a Thermo Nexus 670 FTIR in transmission mode with the film prepared on a ZnSe prism and the absorption measured in total internal reflection.

Transmission Electron Microscopy (TEM). TEM images were obtained on a FEI Technai Spirit or F30 microscopes at 300 kV.

Size Distribution Measurement. CQD sizes are analyzed manually from the TEM images, and the size histogram is fitted with a gaussian function. The volume is calculated using the mean radius/apex to base distance as the diameter of a perfect sphere.

4.9 The $k \cdot p$ Modelling for HgTe CQDs

The band structure of the HgTe CQD can be best described by the

1. *The 2-Band $k \cdot p$ Model*

The 2-band $k \cdot p$ model arise from the zinc-blend tetrahedral symmetry of the crystal lattice, where we assume the valence band arising from the anion (Te) is p-like and have 3-fold symmetry. The conductance band comes from the cation (Hg) behaving s-like.

The Schrodinger Equation for a single electron of mass m inside a crystal with potential $V(r)$ can be expressed by

$$\left(\frac{\mathrm{p}^2}{2m} + V(r)\right)|\psi(r)\rangle = E|\psi(r)\rangle$$

In the case of being inside a crystal lattice with periodicity of a. Bloch's theorem states that the potential and the electron wavefunction will follow the same periodicity, where $V(r) = V(r + ca)$ and $|\psi(r)\rangle = |\psi(r + ca)\rangle$, where c is any interger. The wavefunction always takes the form

$$|\psi_{n,k}(r)\rangle = e^{ikr}|u_{n,k}(r)\rangle$$

$|u_{n,k}(r)\rangle$ is called the Bloch function and have the same periodicity as the crystal lattice. Substituting the full the wavefunction into the Schrodinger Equation, we would get the Hamiltonian in the basis of the Bloch functions.

$$H_k = \frac{p^2}{2m} + V(r) + \frac{\hbar}{m}k \cdot p + \frac{\hbar^2 k^2}{2m}$$

In this formalism, $p \neq \hbar k$ where k is a vector in the reciprocal lattice where p is an operator in the real lattice. i.e. $k \cdot p = -i\hbar\, k \cdot \nabla_r$.

The best way to think about the Hamiltonian is through perturbation theory when k is close to

the Brillouin zone center, where the unperturbed Hamiltonian being $H_0 = \frac{p^2}{2m} + V$ the energy at the zone center where $k = 0$, and $H_{1,k} = \frac{\hbar}{m} k \cdot p + \frac{\hbar^2 k^2}{2m}$ is the perturbed term can be derived from the 1st and 2nd order perturbation theory.

The simplest example that can be derived from this $k \cdot p$ theory is called the two-band Kane model. Using HgTe semimetal as an example, the system comprises of two bands: the conductance band c and the valence band v. The band gap of the two HgTe being E_g.

Using the Bloch function of the two bands as the basis of our model, we get

$$H = \begin{pmatrix} \langle u_c|H_0|u_c\rangle & \langle u_c|H_0|u_v\rangle \\ \langle u_v|H_0|u_c\rangle & \langle u_v|H_0|u_v\rangle \end{pmatrix} + \begin{pmatrix} \langle u_c|H_{1,k}|u_c\rangle & \langle u_c|H_{1,k}|u_v\rangle \\ \langle u_v|H_{1,k}|u_c\rangle & \langle u_v|H_{1,k}|u_v\rangle \end{pmatrix}$$

$$= \begin{pmatrix} E_g/2 & 0 \\ 0 & -E_g/2 \end{pmatrix} + \begin{pmatrix} \langle u_c|H_{1,k}|u_c\rangle & \langle u_c|H_{1,k}|u_v\rangle \\ \langle u_v|H_{1,k}|u_c\rangle & \langle u_v|H_{1,k}|u_v\rangle \end{pmatrix}$$

To obtain the perturbation term, we need some knowledge of the material. Consider the diagonal term, since $\langle u_c|u_v\rangle = \delta_{cv}$, the question is about the term $\langle u_c|-\mathrm{i}\hbar\nabla_r|u_c\rangle$. For crystal lattice with inversion center, $\langle u_c|-\mathrm{i}\hbar\nabla_r|u_c\rangle = 0$ always. However, crystals of HgTe unit cell have $F\bar{4}3m$ symmetry without an inversion center, corresponding to a Bloch function with T_d symmetry in the group representations where $|u_c\rangle$ is not antisymmetric. Therefore, to justify setting $\langle u_c|-\mathrm{i}\hbar\nabla_r|u_c\rangle = 0$, we require that $k \to 0$ at the zone center where the band is at its extremum, as such the $\nabla_r|u_c\rangle$ is small in this model.,

$$\langle u_c|H_{1,k}|u_c\rangle = \langle u_v|H_{1,k}|u_v\rangle = \frac{\hbar}{m} k \cdot \langle u_c|-\mathrm{i}\hbar\nabla_r|u_c\rangle + \frac{\hbar^2 k^2}{2m}\langle u_c|u_c\rangle = \frac{\hbar^2 k^2}{2m}$$

Similarly, the off-diagonal term.

$$\langle u_c|H_{1,k}|u_v\rangle = \frac{\hbar}{m} k \cdot \langle u_c|-\mathrm{i}\hbar\nabla_r|u_v\rangle + \frac{\hbar^2 k^2}{2m}\langle u_c||u_v\rangle = \frac{\hbar}{m} kP$$

where P is defined as $\langle u_c|-\mathrm{i}\hbar\nabla_r|u_v\rangle$. P has units of same as momentum, and the magnitude

shows the coupling strength between the conductance band and valence band of our model. Thus, the two-band $k \cdot p$ model is formulated. Luckily, this has an analytical solution by diagonalizing the Hamiltonian, we get the energy of the two bands.

$$E = \frac{\hbar^2 k^2}{2m} \pm \sqrt{\frac{E_g^2}{4} + \left(\frac{\hbar k P}{m}\right)^2}$$

Sometimes in literature, the constant P is given in the unit of energy E_p, where $E_p = \frac{P^2}{2m}$. E_p is commonly called the Kane parameter or Kane energy. Overall, the $k \cdot p$ model is useful when the band gap E_g and the Kane energy E_p can be determined in experiments. The extraction of E_p is usually more challenging, and in theory can be calculated from the *ab initio* band structure. In most literature this parameter is fitted to experimental data.

Such is the description for the band structure of bulk HgTe. For the case of a spherical HgTe quantum dot with radius r. k is quantized by the boundary conditions. Therefore, for the intraband transition, the $1S$ state is taken where $k = \frac{\pi}{r}$, the energy transition for this HgTe CQD is described as:

$$\Delta E = \sqrt{E_g^2 + \frac{\hbar^2 \pi^2}{2mr^2} \cdot 4E_p}$$

At room temperature, for a dot at radius of 5 nm and $E_g = 0.122\ eV$ and $E_p = 15\ eV$. It would predict the transition $\Delta E \sim 1.27\ eV$ or 10000 cm^{-1}, much larger than experimentally measured. Therefore, though the two-band Kane model is sufficient for most semiconductors, is bad at predicting the actual energy levels of the HgTe quantum dots. Heavy metals such as HgTe have significant contribution from the spin-orbit interaction in the conductance and valence band, so a simple 2-band model is a poor approximation.

2. The 8-Band $k \cdot p$ Model

Conventionally, the modeling of the energy levels in the HgTe CQDs are done using the 8-band $k \cdot p$ model, where we take the symmetry of the bands and spin-orbit coupling interaction into consideration.

The introduction of the spin-orbit interaction into the Bloch Hamiltonian is given by

$$H_{so} = \frac{\hbar}{(2mc)^2}[(\sigma \times \nabla V) \cdot p + (\sigma \times \nabla V) \cdot k]$$

where σ is a vector of the Pauli Spin matrices. Since in this model $k \ll p$, we can ignore the second term and rewrite the Hamiltonian by taking the fact that$(\sigma \times \nabla V) \cdot p = (\nabla V \times p) \cdot \sigma$.

$$H = \frac{p^2}{2m} + V(r) + \frac{\hbar}{m} k \cdot p + \frac{\hbar}{(2mc)^2}(\nabla V \times p) \cdot \sigma + \frac{\hbar^2 k^2}{2m}$$

As the first three term has no interaction with electron spin, a simple model can be constructed using the $|L, S\rangle$ basis. Where the basis used in this model is given as:

$$|S, \downarrow\rangle, -\frac{i}{\sqrt{2}}|X - iY, \uparrow\rangle, -i|Z, \downarrow\rangle, -\frac{i}{\sqrt{2}}|X + iY, \uparrow\rangle$$

$$|S, \uparrow\rangle, \frac{i}{\sqrt{2}}|X + iY, \downarrow\rangle, -i|Z, \uparrow\rangle, -\frac{i}{\sqrt{2}}|X - iY, \downarrow\rangle$$

Where all the bases are orthogonal. The $|S\rangle$ states are conventionally taken as the conduction band where the $|P\rangle = |X\rangle, |Y\rangle, |Z\rangle$ are the valence band. In the case for HgTe this is incorrect as it has a unique band structure with inverted conductance and valence bands.

From here, one can compute the Bloch Hamiltonian using the following:

The Kane parameter is the interaction term between the conductance $|S\rangle$ and the valence bands $|P\rangle$, which we can denote as.

$$P = -\hbar \left\langle S \middle| \frac{d}{dX} \middle| X \right\rangle = -\hbar \left\langle S \middle| \frac{d}{dY} \middle| Y \right\rangle = -\hbar \left\langle S \middle| \frac{d}{dZ} \middle| Z \right\rangle$$

By the way basis functions are constructed, all term vanishes except for the $|S\rangle$ and $|Z\rangle$ interactions and only when the spins of the electrons match. E.g.

$$\left\langle S,\downarrow \left| -i\frac{\hbar}{m}k\cdot p \right| Z,\downarrow \right\rangle = \frac{\hbar}{m}kP$$

The spin-orbit parameter Δ is the interaction of the angular momentum with the gradient of the potential term V. Naturally this term only exists for the $|P\rangle$ orbitals, which is defined as,

$$\Delta = \; i\frac{3\hbar}{(2mc)^2}\langle X|\nabla V\times p|Y\rangle = \; \frac{3\hbar^2}{(2mc)^2}\left\langle X\left|\frac{\partial \mathrm{V}}{\partial x}\frac{\partial}{\partial y}-\frac{\partial \mathrm{V}}{\partial y}\frac{\partial}{\partial x}\right|Y\right\rangle$$

same for the $|Y\rangle, |Z\rangle$ and $|Z\rangle, |X\rangle$ interactions.

The final matrix, under the bases describe before, would take a block diagonal form,

$$H = \begin{bmatrix} M & 0 \\ 0 & M \end{bmatrix}$$

where

$$M = \begin{bmatrix} E_g + \frac{\hbar^2k^2}{2m} & 0 & \frac{\hbar}{m}kP & 0 \\ 0 & -\frac{2\Delta}{3}+\frac{\hbar^2k^2}{2m} & \frac{\sqrt{2}\Delta}{3} & 0 \\ \frac{\hbar}{m}kP & \frac{\sqrt{2}\Delta}{3} & -\frac{\Delta}{3}+\frac{\hbar^2k^2}{2m} & 0 \\ 0 & 0 & 0 & \frac{\hbar^2k^2}{2m} \end{bmatrix}$$

Δ is the spin-orbit coupling, and $E_P = {}^{2P^2}/_{m}$ is the Kane Parameter in the model.

The Band Structure of HgTe can is shown in Fig. 4-6.[45]

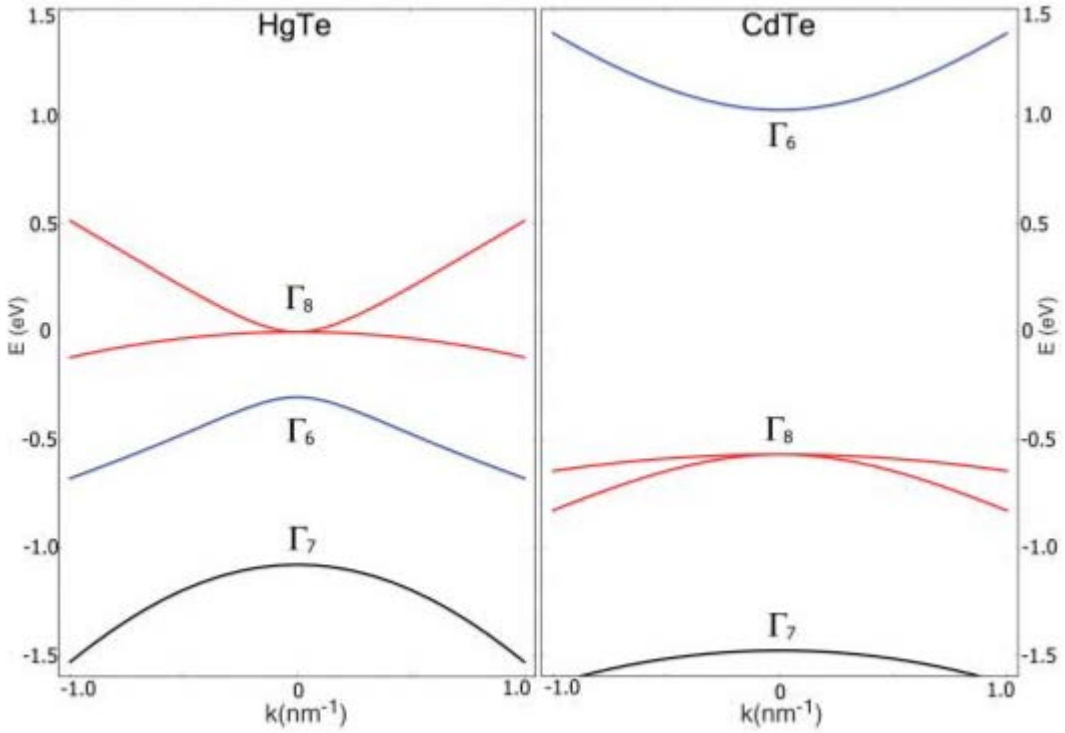

Fig. 4-6. Band Structure of HgTe and CdTe, adapted from Ref. 45

HgTe is commonly referred to be a negative band-gap semiconductor. This is because, as shown in Fig. 4-6, the s-type Γ_6 band lies below the p-type s-type Γ_8 band, under the conventional notation of having a negative E_g. This is opposite for most barrier materials (e.g. CdTe) where the p-type valence band would be below the s-type conduction band. The spin-orbit splitting cause the $|P\rangle$ like bands to split into the Γ_8 bands and Γ_7 bands. Therefore, the conductance band experimentally is the positive curvature Γ_8 band, which would be a light-hole band in other solids such as CdTe.

In most literature, taking only symmetry into consideration, the $k \cdot p$ model constructed with 8-

basis Bloch functions is denoted in the form by the total angular momentum of orbit and spin $|J, m_J\rangle$.

$$\left|\Gamma_6\left(J = \frac{1}{2}\right), +\frac{1}{2}\right\rangle; \left|\Gamma_6\left(J = \frac{1}{2}\right), -\frac{1}{2}\right\rangle$$

$$\left|\Gamma_7\left(J = \frac{1}{2}\right), +\frac{1}{2}\right\rangle; \left|\Gamma_7\left(J = \frac{1}{2}\right), -\frac{1}{2}\right\rangle$$

$$\left|\Gamma_8\left(J = \frac{3}{2}\right), +\frac{3}{2}\right\rangle; \left|\Gamma_8\left(J = \frac{3}{2}\right), +\frac{1}{2}\right\rangle;; \left|\Gamma_8\left(J = \frac{3}{2}\right), -\frac{1}{2}\right\rangle; \left|\Gamma_8\left(J = \frac{3}{2}\right), -\frac{3}{2}\right\rangle$$

However, this basis function does not form a block-diagonal Hamiltonian nicely. This basis is more accurate as it includes the interaction of the spin-splitting and leads to a more accurate band structure. In the 14-band $k \cdot p$ model, this will be the basis sets used in forming the Hamiltonian. In the Section 4.4, we discussed the modeling of the HgTe bands using this 8-band $k \cdot p$ model, the parameters used in the simulation are the following.

Table 4-2: Parameters used for the 8-Band $k \cdot p$ model, the Band Gap and Kane parameters are taken from ref.

R	6.6 nm
E_g	$0.303 - 0.00063 \cdot {T^2}/{(T + 11)}$ eV
E_k	15 eV
Δ	1 eV

The band structure calculated using the 8-Band $k \cdot p$ model is shown in Fig. 4-7.

Band Structure of 8-band model at 300K

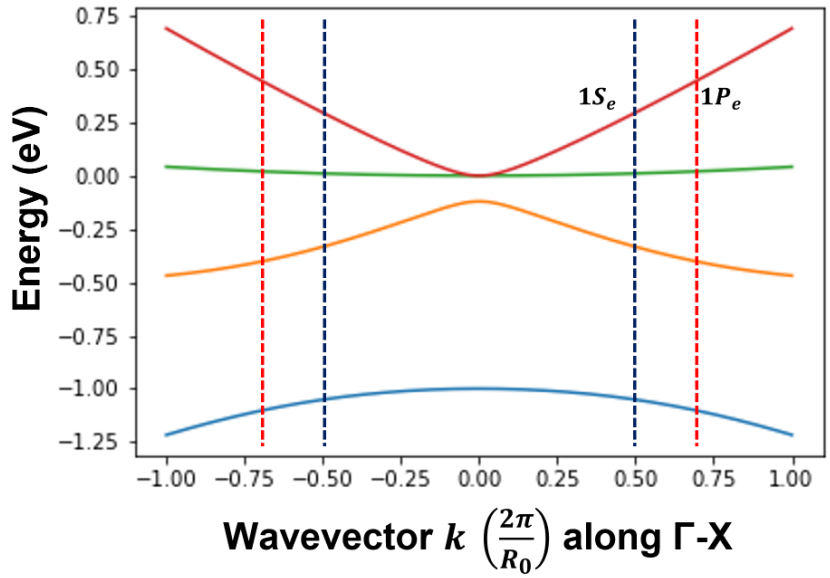

Fig. 4-7 a. Simulated Band Structure of the 8-band $k \cdot p$ model at 300K.

Band Structure of 8-band model at 80K

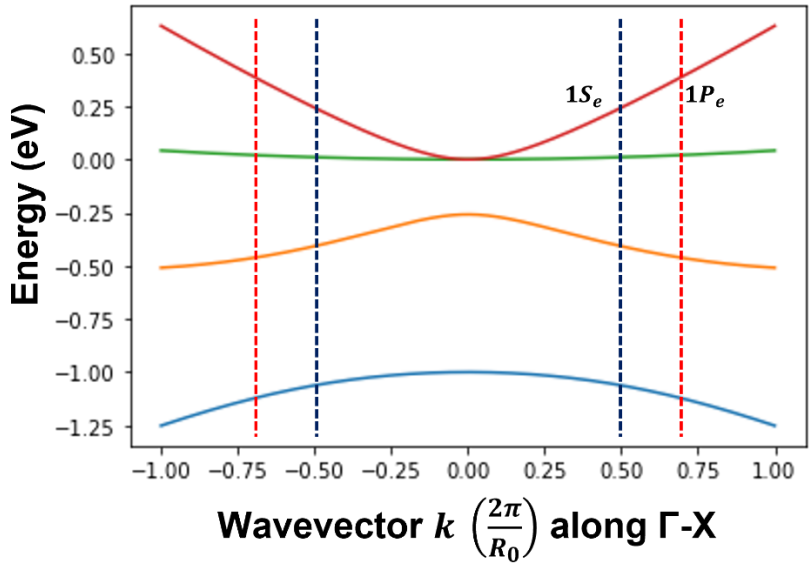

Fig. 4-7 b. Simulated Band Structure of the 8-band $k \cdot p$ model at 80K.

As shown in Fig. 4-2c) and Fig 4-7 a-b., the curvature of the conductance band flattens as temperature decrease, causing the intraband temperature shift to be opposite to the

experimentally measured result.

The simulation also gives a wrong prediction of the sign of the curvature of the heavy-hole band (shown in Fig. 4-7 as the green curve). i.e. the curvature is slightly positive similar to a conduction band, but experimentally the heavy-hole band is still negative. Thus, to explain the band structure more accurately, a larger basis set will be necessary.

3. The 14-band $k \cdot p$ Model

The 14-band $k \cdot p$ model was introduced in El Kurdi et al.,[46] however this section directly follows the work by Moghaddam et al.,[34] which an additional conductance band is introduced to the model around 3 eV higher than the energy gap of HgTe, having a p-like 3-fold degeneracy. Contrary to the 8-band $k \cdot p$ model, we used the $|J, m_J\rangle$ basis function in this model. In addition, we added 6 basis function from the 2nd conductance band from the 1st conductance band above the band structure in Fig. 4-1.

As the 2nd conductance band have p-like Γ_8 and Γ_7 symmetries. The basis function are given as,

$$\left|\Gamma_8^c\ (J\ =\ \frac{3}{2}), +\frac{3}{2}\right\rangle; \left|\Gamma_8^c (J\ =\ \frac{3}{2}), +\frac{1}{2}\right\rangle;; \left|\Gamma_8^c\ \left(J\ =\ \frac{3}{2}\right), -\frac{1}{2}\right\rangle; \left|\Gamma_8^c\ \left(J\ =\ \frac{3}{2}\right), -\frac{3}{2}\right\rangle$$

$$\left|\Gamma_7^c\ (J\ =\ \frac{1}{2}), +\frac{1}{2}\right\rangle; \left|\Gamma_7^c\ (J\ =\ \frac{1}{2}), -\frac{1}{2}\right\rangle$$

The resulting Hamiltonian is of the form:

$H =$

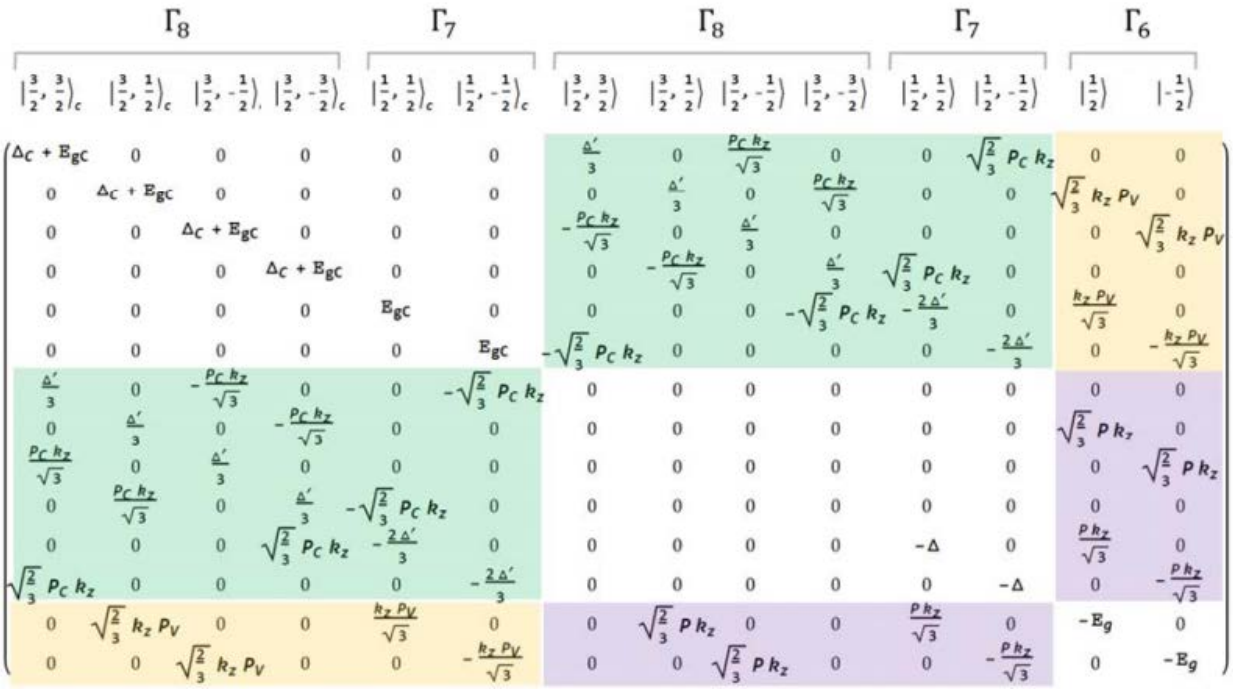

$+\frac{\hbar^2 k^2}{2m}\, Id_{14}$

Where E_g, E_{gC} are the 2 band gaps (conductance-valence and conductance-2nd Conductance). Δ, Δ' and Δ_C are the 3 spin-orbit couplings, $P = \sqrt{E_p \hbar^2/2m}$, $P_C = \sqrt{E_{pC} \hbar^2/2m}$ and $P_V = \sqrt{E_{pV} \hbar^2/2m}$ are the 3 interaction matrix elements with the corresponding Kane parameters.

The Hamiltonian can be viewed nicely with 4 parts, which is shown with different colors.

The white block matrix is a diagonal matrix stating the energy levels at the Γ point, where k = 0. The green matrix states the interaction between the $|P\rangle$-like 2nd conduction band and $|P\rangle$-like valence band. The yellow and purple matrix is the interactions between the $|S\rangle$-like band and the $|P\rangle$-like 2nd conduction band, and interactions between the $|S\rangle$-like band and the $|P\rangle$-like valence band respectively.

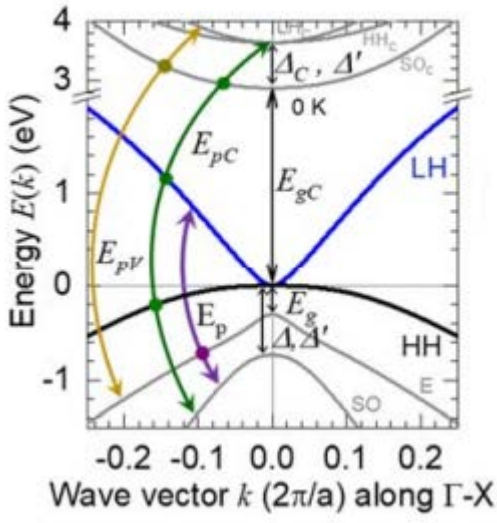

Fig. 4-8. Interactions between bands of HgTe, adapted from Ref. 34

These interactions are shown in Fig. 4-8., note that the blue curve is the LH band, being the actual conduction band measured experimentally. This is similar to the 8-Band model. Most difference arise from the presence of the 2nd conduction band temperature dependence of E_{gC}.

The modeling parameters used in section 4.4 are given below.

These numbers are different from parameter given in Moghaddam et al., which the in this paper the parameter are used to fit experimental data in Hudson et al.[35]

Table 4-3: Parameters used for the 14-Band $k \cdot p$ model, the Band Gap and Kane parameters for the

E_p are taken from ref. Others are fitted to the experimental data.

R	6.6 nm
E_g	$0.305 - 0.00063 \cdot {T^2}/{(T + 11)}$ eV
E_{gC}	$2.2 - 0.003T$ eV
E_p	20 eV
E_{pC}	10 eV
E_{pV}	3 eV
Δ	0.5 eV
Δ'	-2 eV
Δ_C	1 eV

Fitting the 14-band model to Experimental Data from Hudson et al.[35]

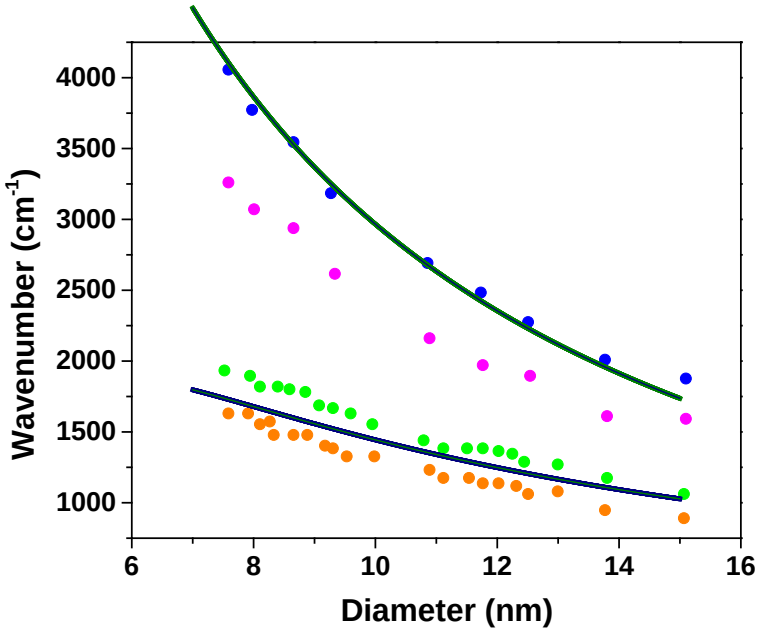

Fig. 4-9, Fit of the 14-band model with data from Hudson et al. Intraband transition (Blue) and Interband transition (Green).

In contrary to Fig 4-10, the curvature of the conductance band increase around the zone edge as temperature decrease, causing the intraband peak to shift bluer as temperature decreases0 the, same direction as the experiments measured.

Band Structure of 14-band model at 300K

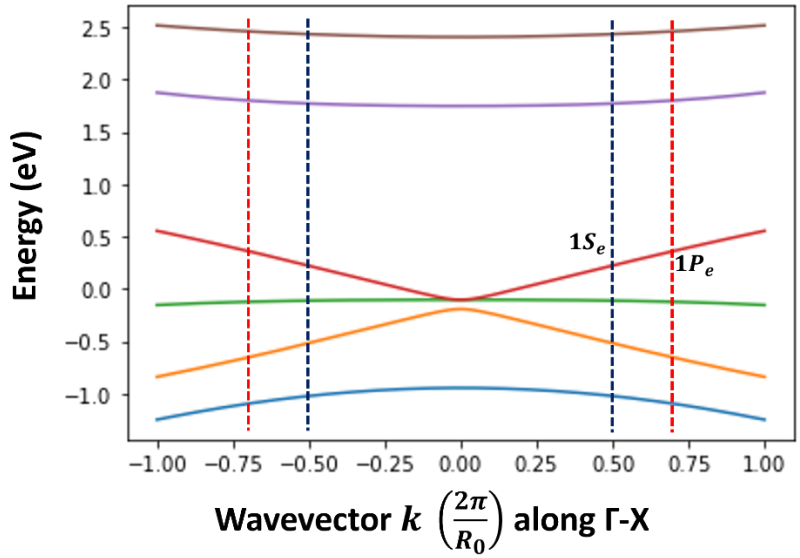

Fig. 4-10 a. Simulated band structure of the 14-band $k \cdot p$ model at 300K. The conductance band is given as the red curve.

Band structure of 14-band model at 80K

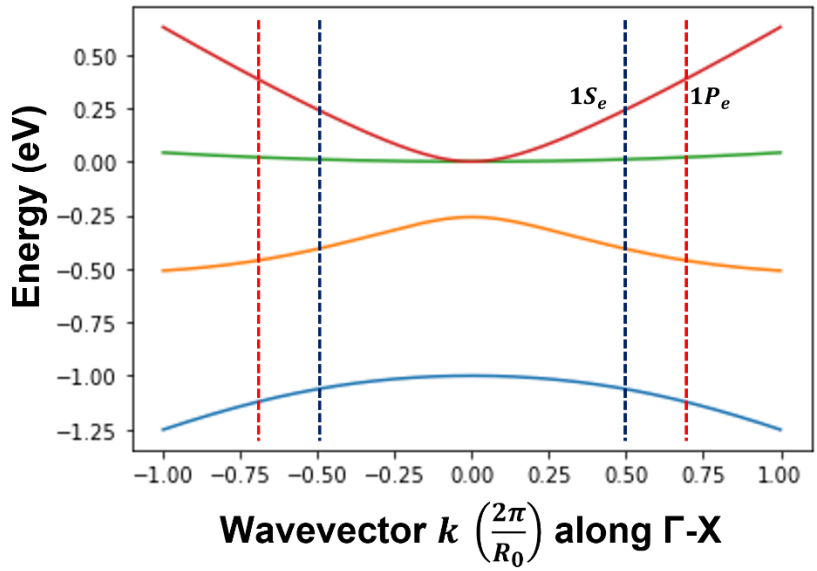

Fig. 4-10 b. Simulated Band Structure of the 14-band $k \cdot p$ model at 80K. The conductance band is given as the red curve.

4.10 Modeling of the Photoconductors

Assuming a photoconductor device with a uniform doping level and thickness, the dark current of this device can be described as,

$$I = (n_e\mu_e + n_h\mu_h)\left(\frac{LWt}{V_{dot}}\right)\frac{eV}{L^2}$$

n_e n_h are the density of electron and hole per dot, τ the carrier lifetime, μ_e μ_h are the electron mobility and hole mobility respectively. L is the length of the channel, W the width of the channel and t the thickness of the film. V_{dot} is the volume of each dot, including the void spaces. Similarity, the photocurrent of this device can be described as,

$$I = \alpha\eta\varphi\tau\,(\mu_e + \mu_h)\,\frac{W}{L}eV$$

α is the optical absorption of the film, η is the probability of ionizing the exciton into separate electrons and holes, φ is the photon flux (1/cm^2 s), and τ the carrier lifetime.

Since α can be simulated using the transfer matrix method using the methods in section 4.11, φ can be estimated using the photon flux using a blackbody with a fixed temperature and solid angle, and $\mu_{e,h}$ can be measured using the in-built FET on the same device. One can calculated the internal quantum efficiency IQE by

$$IQE = \frac{photoelectron\ collected}{photons\ absorbed} = \frac{J_{ph}/e}{\alpha\varphi} = \eta\frac{L_{drift}}{L}$$

J_{ph} is the photocurrent density normalized to the device thickness and area. L_{drift} is the drift length of the generated electron and hole pair. Assuming η ~ 1, one can estimate the L_{drift} and the carrier lifetime τ, given by,

$$L_{drift} = \mu\tau\frac{V}{L}$$

With different relaxation mechanism, τ would have different dependencies on carrier density.

For exciton relaxation dominated by surface trapping,

$$\tau^{-1} = n_{trap}\tau_{exc}^{-1}$$

n_{trap} is the density of traps per unit dot. Therefore, τ would have no dependencies on the electron and hole density.

For germinate recombination relaxation,

$$\tau^{-1} = (n_0 + p_0)\tau_{exc}^{-1}$$

n_0, p_0 are the density of the electron and holes respectively.

For Auger relaxation,

$$\tau^{-1} = 6n_i^2\tau_{exc}^{-1}$$

$n_i = \sqrt{n_0\, p_0}$ is the average density of the electron and holes.

Therefore, one could extrapolate the relaxation mechanism by dependency of τ on the power of the n_i.

4.11 Spectrum Simulation using the Transfer Matrix Method

The simulation of the film absorption is done using the Transfer Matrix Method. The electric field intensity is calculated as every point in the device structure and absorption density is calculated from the electric field using the formula

$$abs_j(z) = \frac{|E_f + E_b|^2 Im(n_j) k_z}{Re(n_0)}$$

where E_f, E_b are the forward and backward electric field magnitude, $Im(n_j)$ is the imaginary refractive index in layer j, k_z is the wavevector at point z, and $Re(n_0)$ is the refractive index for the first layer.

The device structure used in the simulation is given as:

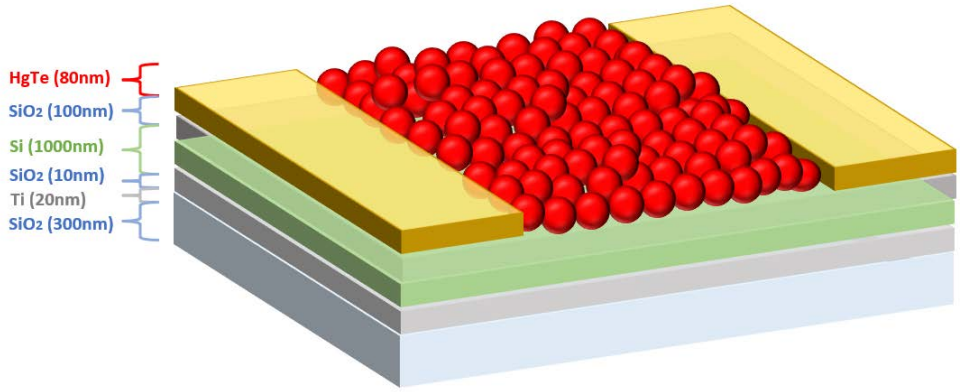

To make the simulation accurate, the refractive index of HgTe discussed in this paper is used, where the 1st and 2nd intraband peak is blue-shifted by 60 cm^{-1} and 150 cm^{-1} respectively to account that the intraband spectrum is measured at 80K. For SiO_2, the refractive index is extrapolated from data in Ref 4.[47] Ti is assumed to be a perfect back reflector for the spectrum shown in Fig. 4a as the width of the reflection is very sensitive to the refractive index of Ti. However, as a comparison, we have also done the simulation using refractive index of Ti given in Ref 5.[48]

The simulated absorption of HgTe and SiO_2 is shown below.

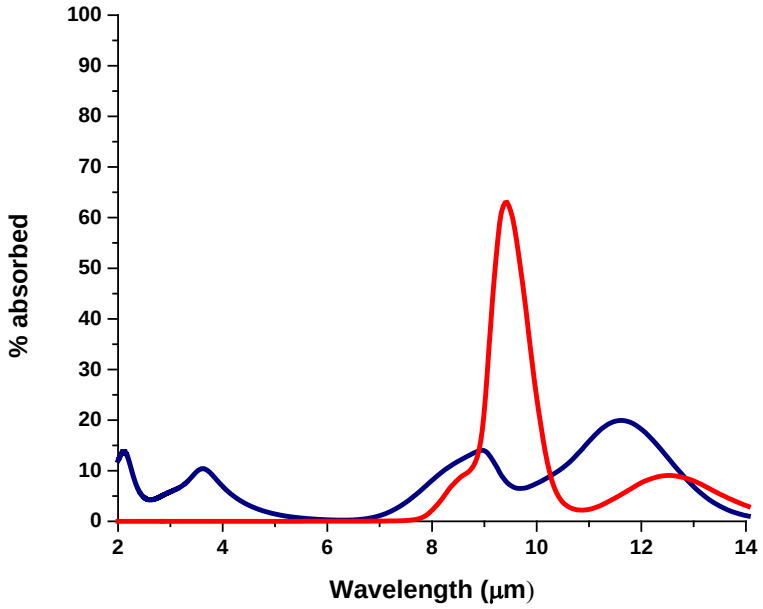

Fig. 4-11 a, Simulated Absorption Spectrum of 80 nm HgTe CQD film (Navy) and SiO2 film (Red) with SiO2 refractive index reported from ref. 47 and a perfect back reflector.

It can be seen that the dip around the 10 μm in film absorption is primarily due to the SiO_2 reststrahlen effect.

As a comparison, a simulation is also done assuming a constant real refractive index that is non-absorbing in the infrared for SiO_2 and Ti being a prefect back reflector. This confirms that the simulation gives a good estimate of the experimental spectrum.

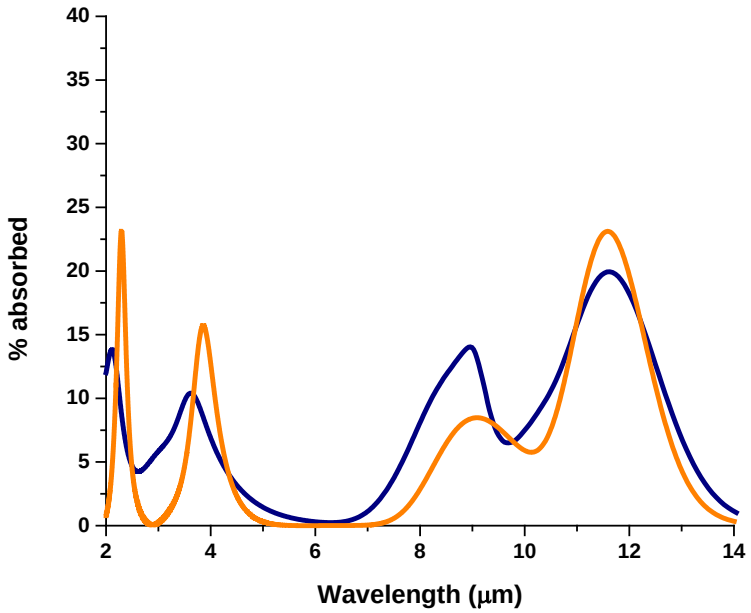

Fig. 4-11 b, Simulated Absorption Spectrum of 80 nm HgTe CQD film with experimental SiO2 and Ti refractive index (Orange) and spacer with no absorption and a back reflector (Navy).

References:

(1) Kagan, C. R.; Lifshitz, E.; Sargent, E. H.; Talapin, D. V. Building Devices from Colloidal Quantum Dots. *Science* **2016**, *353* (6302), aac5523. https://doi.org/10.1126/science.aac5523.

(2) García de Arquer, F. P.; Talapin, D. V.; Klimov, V. I.; Arakawa, Y.; Bayer, M.; Sargent, E. H. Semiconductor Quantum Dots: Technological Progress and Future Challenges. *Science* **2021**, *373* (6555), eaaz8541. https://doi.org/10.1126/science.aaz8541.

(3) Norris, D. J.; Efros, Al. L.; Rosen, M.; Bawendi, M. G. Size Dependence of Exciton Fine Structure in CdSe Quantum Dots. *Phys. Rev. B* **1996**, *53* (24), 16347–16354. https://doi.org/10.1103/PhysRevB.53.16347.

(4) Efros, A. L.; Brus, L. E. Nanocrystal Quantum Dots: From Discovery to Modern Development. *ACS Nano* **2021**, *15* (4), 6192–6210. https://doi.org/10.1021/acsnano.1c01399.

(5) Deng, Z.; Jeong, K. S.; Guyot-Sionnest, P. Colloidal Quantum Dots Intraband Photodetectors. *ACS Nano* **2014**, *8* (11), 11707–11714. https://doi.org/10.1021/nn505092a.

(6) Piels, M.; Bowers, J. E. 1 - Photodetectors for Silicon Photonic Integrated Circuits. In *Photodetectors*; Nabet, B., Ed.; Woodhead Publishing, 2016; pp 3–20. https://doi.org/10.1016/B978-1-78242-445-1.00001-4.

(7) Moazzami, K.; Phillips, J.; Lee, D.; Krishnamurthy, S.; Benoit, G.; Fink, Y.; Tiwald, T. Detailed Study of above Bandgap Optical Absorption in HgCdTe. *J. Electron. Mater.* **2005**, *34* (6), 773–778. https://doi.org/10.1007/s11664-005-0019-3.

(8) Scimeca, M. R.; Mattu, N.; Paredes, I. J.; Tran, M. N.; Paul, S. J.; Aydil, E. S.; Sahu, A. Origin of Intraband Optical Transitions in Ag2Se Colloidal Quantum Dots. *J. Phys. Chem. C* **2021**, *125* (31), 17556–17564. https://doi.org/10.1021/acs.jpcc.1c05371.

(9) Hafiz, S. B.; Scimeca, M. R.; Zhao, P.; Paredes, I. J.; Sahu, A.; Ko, D.-K. Silver Selenide Colloidal Quantum Dots for Mid-Wavelength Infrared Photodetection. *ACS Appl. Nano Mater.* **2019**, *2* (3), 1631–1636. https://doi.org/10.1021/acsanm.9b00069.

(10) Chen, M.; Hao, Q.; Luo, Y.; Tang, X. Mid-Infrared Intraband Photodetector via High Carrier Mobility HgSe Colloidal Quantum Dots. *ACS Nano* **2022**, *16* (7), 11027–11035. https://doi.org/10.1021/acsnano.2c03631.

(11) Hafiz, S. B.; Al Mahfuz, M. M.; Ko, D.-K. Vertically Stacked Intraband Quantum Dot Devices for Mid-Wavelength Infrared Photodetection. *ACS Appl. Mater. Interfaces* **2021**, *13* (1), 937–943. https://doi.org/10.1021/acsami.0c19450.

(12) Livache, C.; Martinez, B.; Goubet, N.; Gréboval, C.; Qu, J.; Chu, A.; Royer, S.; Ithurria, S.; Silly, M. G.; Dubertret, B.; Lhuillier, E. A Colloidal Quantum Dot Infrared Photodetector

and Its Use for Intraband Detection. *Nat. Commun.* **2019**, *10* (1), 2125. https://doi.org/10.1038/s41467-019-10170-8.

(13) Bera, R.; Choi, D.; Jung, Y. S.; Song, H.; Jeong, K. S. Intraband Transitions of Nanocrystals Transforming from Lead Selenide to Self-Doped Silver Selenide Quantum Dots by Cation Exchange. *J. Phys. Chem. Lett.* **2022**, *13* (26), 6138–6146. https://doi.org/10.1021/acs.jpclett.2c01179.

(14) Zarghami, M. H.; Liu, Y.; Gibbs, M.; Gebremichael, E.; Webster, C.; Law, M. P-Type PbSe and PbS Quantum Dot Solids Prepared with Short-Chain Acids and Diacids. *ACS Nano* **2010**, *4* (4), 2475–2485. https://doi.org/10.1021/nn100339b.

(15) Ramiro, I.; Kundu, B.; Dalmases, M.; Özdemir, O.; Pedrosa, M.; Konstantatos, G. Size- and Temperature-Dependent Intraband Optical Properties of Heavily n-Doped PbS Colloidal Quantum Dot Solid-State Films. *ACS Nano* **2020**, *14* (6), 7161–7169. https://doi.org/10.1021/acsnano.0c02033.

(16) Hu, Z.; Kim, Y.; Krishnamurthy, S.; Avdeev, I. D.; Nestoklon, M. O.; Singh, A.; Malko, A. V.; Goupalov, S. V.; Hollingsworth, J. A.; Htoon, H. Intrinsic Exciton Photophysics of PbS Quantum Dots Revealed by Low-Temperature Single Nanocrystal Spectroscopy. *Nano Lett.* **2019**, *19* (12), 8519–8525. https://doi.org/10.1021/acs.nanolett.9b02937.

(17) Zhang, H.; Guyot-Sionnest, P. Shape-Controlled HgTe Colloidal Quantum Dots and Reduced Spin–Orbit Splitting in the Tetrahedral Shape. *J. Phys. Chem. Lett.* **2020**, *11* (16), 6860–6866. https://doi.org/10.1021/acs.jpclett.0c01550.

(18) Keuleyan, S. E.; Guyot-Sionnest, P.; Delerue, C.; Allan, G. Mercury Telluride Colloidal Quantum Dots: Electronic Structure, Size-Dependent Spectra, and Photocurrent Detection up to 12 Mm. *ACS Nano* **2014**, *8* (8), 8676–8682. https://doi.org/10.1021/nn503805h.

(19) Shen, G.; Chen, M.; Guyot-Sionnest, P. Synthesis of Nonaggregating HgTe Colloidal Quantum Dots and the Emergence of Air-Stable n-Doping. *J. Phys. Chem. Lett.* **2017**, *8* (10), 2224–2228. https://doi.org/10.1021/acs.jpclett.7b00775.

(20) Chen, M.; Guyot-Sionnest, P. Reversible Electrochemistry of Mercury Chalcogenide Colloidal Quantum Dot Films. *ACS Nano* **2017**, *11* (4), 4165–4173. https://doi.org/10.1021/acsnano.7b01014.

(21) Chen, M.; Lan, X.; Tang, X.; Wang, Y.; Hudson, M. H.; Talapin, D. V.; Guyot-Sionnest, P. High Carrier Mobility in HgTe Quantum Dot Solids Improves Mid-IR Photodetectors. *ACS Photonics* **2019**, *6* (9), 2358–2365. https://doi.org/10.1021/acsphotonics.9b01050.

(22) Chen, M.; Shen, G.; Guyot-Sionnest, P. State-Resolved Mobility of 1 Cm2/(Vs) with HgSe Quantum Dot Films. *J. Phys. Chem. Lett.* **2020**, *11* (6), 2303–2307. https://doi.org/10.1021/acs.jpclett.0c00587.

(23) Yang, J.; Hu, H.; Lv, Y.; Yuan, M.; Wang, B.; He, Z.; Chen, S.; Wang, Y.; Hu, Z.; Yu, M.; Zhang, X.; He, J.; Zhang, J.; Liu, H.; Hsu, H.-Y.; Tang, J.; Song, H.; Lan, X. Ligand-Engineered HgTe Colloidal Quantum Dot Solids for Infrared Photodetectors. *Nano Lett.* **2022**, *22* (8), 3465–3472. https://doi.org/10.1021/acs.nanolett.2c00950.

(24) Ackerman, M. M.; Tang, X.; Guyot-Sionnest, P. Fast and Sensitive Colloidal Quantum Dot Mid-Wave Infrared Photodetectors. *ACS Nano* **2018**, *12* (7), 7264–7271. https://doi.org/10.1021/acsnano.8b03425.

(25) Lhuillier, E.; Keuleyan, S.; Guyot-Sionnest, P. Optical Properties of HgTe Colloidal Quantum Dots. *Nanotechnology* **2012**, *23* (17), 175705. https://doi.org/10.1088/0957-4484/23/17/175705.

(26) O'Donnell, K. P.; Chen, X. Temperature Dependence of Semiconductor Band Gaps. *Appl. Phys. Lett.* **1991**, *58* (25), 2924–2926. https://doi.org/10.1063/1.104723.

(27) Fan, H. Y. Temperature Dependence of the Energy Gap in Monatomic Semiconductors. *Phys. Rev.* **1950**, *78* (6), 808–809. https://doi.org/10.1103/PhysRev.78.808.2.

(28) Keffer, C.; Hayes, T. M.; Bienenstock, A. Debye-Waller Factors and the PbTe Band-Gap Temperature Dependence. *Phys. Rev. B* **1970**, *2* (6), 1966–1976. https://doi.org/10.1103/PhysRevB.2.1966.

(29) Olkhovets, A.; Hsu, R.-C.; Lipovskii, A.; Wise, F. W. Size-Dependent Temperature Variation of the Energy Gap in Lead-Salt Quantum Dots. *Phys. Rev. Lett.* **1998**, *81* (16), 3539–3542. https://doi.org/10.1103/PhysRevLett.81.3539.

(30) Deng, Z.; Guyot-Sionnest, P. Intraband Luminescence from HgSe/CdS Core/Shell Quantum Dots. *ACS Nano* **2016**, *10* (2), 2121–2127. https://doi.org/10.1021/acsnano.5b06527.

(31) Dey, P.; Paul, J.; Bylsma, J.; Karaiskaj, D.; Luther, J. M.; Beard, M. C.; Romero, A. H. Origin of the Temperature Dependence of the Band Gap of PbS and PbSe Quantum Dots. *Solid State Commun.* **2013**, *165*, 49–54. https://doi.org/10.1016/j.ssc.2013.04.022.

(32) Dai, Q.; Zhang, Y.; Wang, Y.; Hu, M. Z.; Zou, B.; Wang, Y.; Yu, W. W. Size-Dependent Temperature Effects on PbSe Nanocrystals. *Langmuir* **2010**, *26* (13), 11435–11440. https://doi.org/10.1021/la101545w.

(33) Allan, G.; Delerue, C. Tight-Binding Calculations of the Optical Properties of HgTe Nanocrystals. *Phys. Rev. B* **2012**, *86* (16), 165437. https://doi.org/10.1103/PhysRevB.86.165437.

(34) Moghaddam, N.; Gréboval, C.; Qu, J.; Chu, A.; Rastogi, P.; Livache, C.; Khalili, A.; Xu, X. Z.; Baptiste, B.; Klotz, S.; Fishman, G.; Capitani, F.; Ithurria, S.; Sauvage, S.; Lhuillier, E.

The Strong Confinement Regime in HgTe Two-Dimensional Nanoplatelets. *J. Phys. Chem. C* **2020**, *124* (42), 23460–23468. https://doi.org/10.1021/acs.jpcc.0c07533.

(35) Hudson, M. H.; Chen, M.; Kamysbayev, V.; Janke, E. M.; Lan, X.; Allan, G.; Delerue, C.; Lee, B.; Guyot-Sionnest, P.; Talapin, D. V. Conduction Band Fine Structure in Colloidal HgTe Quantum Dots. *ACS Nano* **2018**, *12* (9), 9397–9404. https://doi.org/10.1021/acsnano.8b04539.

(36) Prado, Y.; Qu, J.; Gréboval, C.; Dabard, C.; Rastogi, P.; Chu, A.; Khalili, A.; Xu, X. Z.; Delerue, C.; Ithurria, S.; Lhuillier, E. Seeded Growth of HgTe Nanocrystals for Shape Control and Their Use in Narrow Infrared Electroluminescence. *Chem. Mater.* **2021**, *33* (6), 2054–2061. https://doi.org/10.1021/acs.chemmater.0c04526.

(37) Muljarov, E. A.; Zimmermann, R. Dephasing in Quantum Dots: Quadratic Coupling to Acoustic Phonons. *Phys. Rev. Lett.* **2004**, *93* (23), 237401. https://doi.org/10.1103/PhysRevLett.93.237401.

(38) Krauss, T. D.; Wise, F. W. Coherent Acoustic Phonons in a Semiconductor Quantum Dot. *Phys. Rev. Lett.* **1997**, *79* (25), 5102–5105. https://doi.org/10.1103/PhysRevLett.79.5102.

(39) Besombes, L.; Kheng, K.; Marsal, L.; Mariette, H. Acoustic Phonon Broadening Mechanism in Single Quantum Dot Emission. *Phys. Rev. B* **2001**, *63* (15), 155307. https://doi.org/10.1103/PhysRevB.63.155307.

(40) Whiting, E. E. An Empirical Approximation to the Voigt Profile. *J. Quant. Spectrosc. Radiat. Transf.* **1968**, *8* (6), 1379–1384. https://doi.org/10.1016/0022-4073(68)90081-2.

(41) Ramiro, I.; Özdemir, O.; Christodoulou, S.; Gupta, S.; Dalmases, M.; Torre, I.; Konstantatos, G. Mid- and Long-Wave Infrared Optoelectronics via Intraband Transitions in PbS Colloidal

Quantum Dots. *Nano Lett.* **2020**, *20* (2), 1003–1008. https://doi.org/10.1021/acs.nanolett.9b04130.

(42) Guyot-Sionnest, P.; Peterson, J. C.; Melnychuk, C. Extracting Bulk-like Semiconductor Parameters from the Characterization of Colloidal Quantum Dot Film Photoconductors. *J. Phys. Chem. C* **2022**, *126* (40), 17196–17203. https://doi.org/10.1021/acs.jpcc.2c05391.

(43) Melnychuk, C.; Guyot-Sionnest, P. Slow Auger Relaxation in HgTe Colloidal Quantum Dots. *J. Phys. Chem. Lett.* **2018**, *9* (9), 2208–2211. https://doi.org/10.1021/acs.jpclett.8b00750.

(44) Melnychuk, C.; Guyot-Sionnest, P. Auger Suppression in N-Type HgSe Colloidal Quantum Dots. *ACS Nano* **2019**, *13* (9), 10512–10519. https://doi.org/10.1021/acsnano.9b04608.

(45) Bernevig, B. A.; Hughes, T. L.; Zhang, S.-C. Quantum Spin Hall Effect and Topological Phase Transition in HgTe Quantum Wells. *Science* **2006**, *314* (5806), 1757–1761. https://doi.org/10.1126/science.1133734.

(46) El kurdi, M.; Fishman, G.; Sauvage, S.; Boucaud, P. Comparison between 6-Band and 14-Band $\mathbf{k}\ensuremath{\cdot}\mathbf{p}$ Formalisms in SiGe/Si Heterostructures. *Phys. Rev. B* **2003**, *68* (16), 165333. https://doi.org/10.1103/PhysRevB.68.165333.

(47) Kischkat, J.; Peters, S.; Gruska, B.; Semtsiv, M.; Chashnikova, M.; Klinkmüller, M.; Fedosenko, O.; Machulik, S.; Aleksandrova, A.; Monastyrskyi, G.; Flores, Y.; Masselink, W. T. Mid-Infrared Optical Properties of Thin Films of Aluminum Oxide, Titanium Dioxide, Silicon Dioxide, Aluminum Nitride, and Silicon Nitride. *Appl. Opt.* **2012**, *51* (28), 6789–6798. https://doi.org/10.1364/AO.51.006789.

(48) Rakić, A. D.; Djurišić, A. B.; Elazar, J. M.; Majewski, M. L. Optical Properties of Metallic Films for Vertical-Cavity Optoelectronic Devices. *Appl. Opt.* **1998**, *37* (22), 5271–5283. https://doi.org/10.1364/AO.37.005271.

Chapter 5: Future Perspective

In the preceding chapters, I have demonstrated improvement in the synthesis of HgTe CQDs. I have shown improvement in transport properties, reduced 1/f noise, and demonstrated the use HgTe CQD in infrared detection. In Chapter 5, I will discuss the potential research directions with some opinions on practicality.

HgTe CQD is not only a good infrared material, but also a good candidate for the study of transport in CQDs. Improvement in the synthesis technique, doping control and ligand exchange all contribute to the high mobility measured in CQD systems today. Nevertheless, it remains in question whether true 'delocalization' can be reached in CQD systems since they are naturally disordered. As discussed in Chapter 1, it is difficult reach metallicity in quantum dots due to the high limit of critical carrier density. Therefore, to reduce the critical carrier density to be on the order of 1 e^-/dot, one would need to increase the coupling between dots by both reducing the interdot separation and increase the coupling area.

Increasing the dot-to-dot coupling area may be achieve by using faceted dots. Experimentally the mobility of the faceted dots is typically higher than spherical ones which could be attributed to the increase in the coupling area. However, reducing the interdot distance would be more difficult but not impossible by using shorter inorganic ligands instead of organic ones. Increasing coupling is only one piece of this puzzle, where disorder will also need to be reduced for any metallicity to be possible.

To test the true limit of metallicity in CQD systems, improvement in synthesis using better control techniques can be explored to make uniform dots. Also, one may be tempted to use size selective precipitation to improve the size uniformity to further enhance the mobility in CQD systems.

Fig. 5-1 shows a preliminary study of improvement in the intraband and interband spectrum with

size selective precipitation. With well controlled size selection, one can improve $\Delta E/E$ of the intraband transition by 10% with each precipitation. However, I have also encountered aggregation during repetitive precipitation as each cycle strips the excess Hg on the surface of these CQDs, thus leading to more instability. This also leads to difficulty in the hybrid ligand exchange when transferring these dots into polar solvents. With improved ligand stability by perhaps exchanging the surface oleylamine ligands with thiol ligands and replenishing the Hg content in the dot ink with each cycle, one may be able to reach a size uniformity not reachable by other means. This is a potent path that can be explored to improve the size distribution.

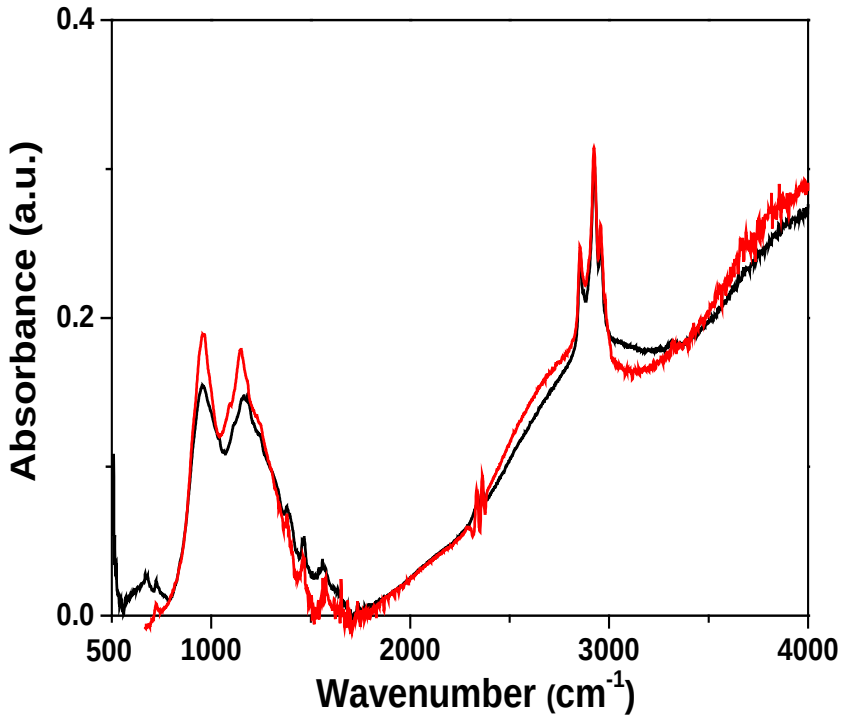

Fig. 5-1 Absorption spectrum of HgTe CQDs before (black) and after (red) size selective precipitation. It can be observed that the linewidth for transitions of the energy levels is reduced by carefully controlling the size.

Since the mobility scales inversely with the gap size on the FET device, one natural way to verify the conductance is to use nanofabrication to make devices on much smaller scale. In Chapter 3, I have demonstrated that the transport behavior of these CQDs follows the ES-VRH theory well at low temperatures, and this transport and the gap length dependence could be explained only if electrons are localized larger than a single dot diameter, which indicate delocalization. This would naturally point in the direction of fabricating devices on the scale of a few quantum dots. If the hypothesis is true that delocalization can be reach on the scale on 4-5 dots, we would be able to measure a finite conductance at 0 K, thus demonstrating the possiblity of disordered system such as CQDs reaching the metallic limit.

Since coupling of the states between two dots are related to the overlap of wavefunctions, it may be advantageous to dope the dots greater than 2 electrons, so the transport can be measured in the $1P_e$ State instead of the $1S_e$ States. As the p-orbital states are more spatially extended, this would increase the coupling between dots, making the limit of metallicity potentially lower. The FET measurement of doped HgTe have already shown the increase mobility of electrons in the $1P_e$ State when compared to the $1S_e$ State. The FET measurement of the high mobility sample is shown in Fig. 5-2.

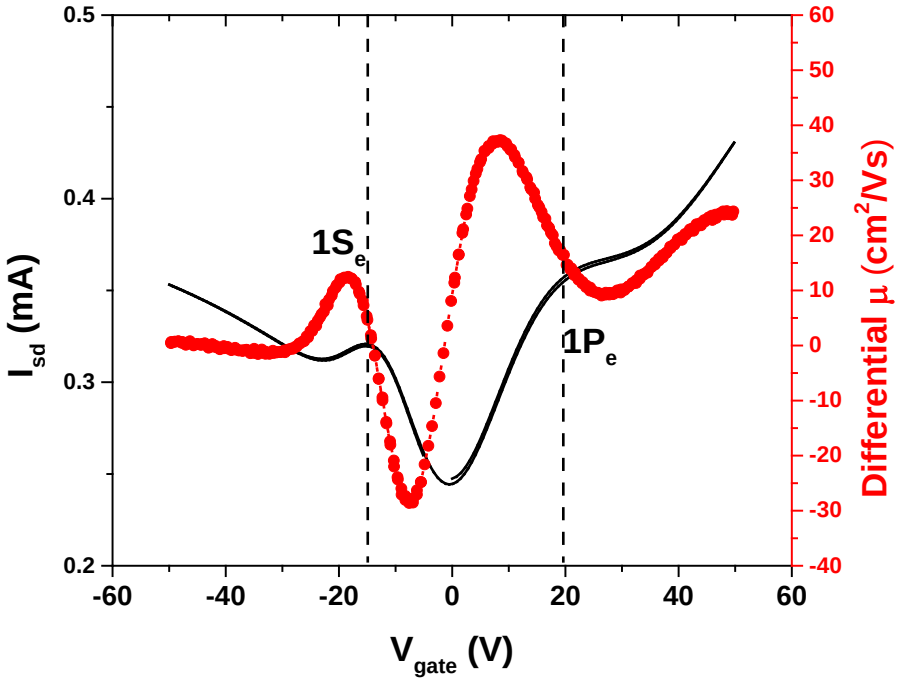

Fig. 5-2. FET measurement and the differential mobility of the high conductance film doped to 2 electrons per dot at 80 K. The 1Se electron mobility is negative as it behaves like a 'hole' due to the state being totally filled.

Another potential research direction is to explore the state-resolved transport of HgTe core/shell structures. Using similar synthetic techniques as discuss in the core/shell synthesis of HgSe/CdS, I have found that 2 layers of CdTe Shell can be growth on HgTe CQDs with significantly improved thermal stability. The absorption spectrum and photoluminescence are also well preserved, with the HgTe/CdTe dots also able to be transferred into polar ink with improved mobility.

In addition to the interest in transport properties, the viability of using HgTe CQDs to further improve the detectivity of long-wave infrared light is also an idea to be explored. As discussed in Chapter 4, I have demonstrated using the intraband transition to make long-wave devices with

detectivity over to 10^7 Jones. However, the detectivity drops rapidly at higher temperatures due to germinate recombination and possibly Auger recombination. Using dots with core/shell structure may be a natural way to resolve this problem. An alternative way to enhance the responsivity of these devices could use cavity or plasmonic. This may be a necessary path to take to make the long-wave infrared CQD photodetectors competitive to the commercial ones.